OUKA
The University of Osaka
Institutional Knowledge Archive

Title	Development of A Novel Wide Dynamic Range Epi-Thermal Neutron Spectrometer for Boron Neutron Capture Therapy
Author(s)	藤原, 悠
Citation	大阪大学, 2026, 博士論文
Version Type	VoR
URL	https://doi.org/10.18910/105464
rights	
Note	

The University of Osaka Institutional Knowledge Archive : OUKA

https://ir.library.osaka-u.ac.jp/

The University of Osaka

Doctoral Dissertation

Development of A Novel Wide Dynamic Range Epi-Thermal Neutron Spectrometer for Boron Neutron Capture Therapy

(BNCT のための広ダイナミックレンジ
熱外中性子スペクトル測定手法の開発)

Yu Fujiwara

January 2026

Graduate School of Engineering,
The University of Osaka

Contents

Abstract **3**

List of Symbols **5**

1 Introduction **9**
1.1 Recent Progress in Radiotherapy 9
1.2 Boron Neutron Capture Therapy (BNCT): Principle and Uses. 11
1.3 Development of Accelerator-Based BNCT and Its Issues 13
1.4 Evaluation of Neutron Energy Spectrum in the Epi-Thermal Range . 16
1.5 Research Objectives 18

2 Theory: Neutron Detectors and Spectrum Unfolding Methods **19**
2.1 Introduction 19
2.2 Conventional Neutron Detectors 19
2.2.1 Scintillators 19
2.2.2 Activation Detectors 20
2.2.3 Gas Detectors 22
2.2.4 Imaging Plate 24
2.3 Spectrum Unfolding Process 27
2.3.1 General Concepts 27
2.3.2 Unfolding Algorithms 28
2.3.3 Stopping Criteria 36
2.4 Conventional Approaches for Epi-thermal Neutron Spectrometry . . . 38
2.5 Application of ^{3}He Position Sensitive Proportional Counter 41
2.6 Monte Carlo Simulation 44
2.7 Summary 46

3 Application of a Pencil Beam Neutron Source **47**
3.1 Introduction 47
3.2 Epi-thermal Neutron Source Based on OKTAVIAN 49
3.2.1 Epi-thermal neutron source 49
3.2.2 Detector assignment 52
3.3 Collimator Design and Its Performance 52
3.3.1 Design goals and Parameters 52
3.3.2 Collimator Material Selection 53
3.3.3 Preliminary Calculations and the Trend Analysis 55
3.3.4 Parameter Determination 56
3.3.5 Beam Characteristics 58
3.4 Numerical Analysis 61
3.4.1 Simulation condition 61
3.4.2 Limitation of This Approach and its Correction 64
3.5 Summary 67

4 Design of Response Function in Monte Carlo Simulation 69
4.1 Introduction . . . 69
4.2 Design of the Response Function . . . 69
4.3 Numerical Analysis . . . 72
4.4 Further Improvements of This Spectrometer . . . 76
4.4.1 Influence of Spectrometer Position on Estimation Performance 76
4.4.2 Influence of Material Composition on Estimation Performance 78
4.4.3 Potential for the Expansion of the Measurable Range . . . 80
4.5 Summary . . . 81

5 Simultaneous Utilization of PSPC and Activation Foils 83
5.1 Introduction . . . 83
5.2 Material Selection . . . 84
5.3 Feasibility Analysis for the Simultaneous Use . . . 85
5.3.1 Evaluations of Response Function . . . 85
5.3.2 Numerical Analysis . . . 87
5.4 Potential Application of This Approach . . . 90
5.5 Summary . . . 90

6 Instrumentation of Imaging Plate for Neutron Spectrometry 93
6.1 Introduction . . . 93
6.2 Detector Configuration . . . 93
6.3 Data Acquisition Approach . . . 96
6.3.1 Experimental Data Processing . . . 96
6.3.2 Simulation strategy . . . 99
6.4 Benchmark Experiment . . . 102
6.4.1 Experimental Set Up and Its Result . . . 102
6.4.2 Calibration from PSL Value to Neutron Intensity . . . 105
6.5 Feasibility of IP-Based Neutron Spectrometer . . . 108
6.6 Summary . . . 110

7 Conclusion 113

Acknowledgements 117

References 119

List of Publications 123

Appendix 127
A Experimental Data Processing in PSPC . . . 127
B Comparison to Unfolding Algortihms . . . 132
C Unique Subsequent MCNP Calculation . . . 134
D Source Code for the Simulation and Data Processing . . . 137

Abstract

Boron Neutron Capture Therapy (BNCT) is a promising radiotherapy that selectively kills tumor cells while causing minimal damage to surrounding normal tissues. With the advancement of accelerator-based BNCT (AB-BNCT), accurate evaluation of the neutron field produced by the accelerator has become essential. In the context of the neutron energy spectrum in the epi-thermal range, conventional approaches have limitations in measurement accuracy, arising from their dependence on the number of materials as detectors. Furthermore, since multiple experiments are required to derive the spectrum, additional uncertainty is added due to varying experimental conditions.

This study proposes two novel spectrometers: a ^{3}He position-sensitive proportional counter (PSPC) and an imaging plate neutron detector (IP-ND), both of which detect neutrons by exploiting their high cross-sections for thermal neutrons. Furthermore, the characteristic features of the cross-sections—namely the 1:1 correspondence between neutron energy and the reaction probability for the PSPC, and the use of boron blocks as a moderator on the IP-ND—can be utilized to reconstruct the neutron energy information from the measurement results.

This thesis reports on the methodology of these approaches and the analytical and experimental results of the estimation. **Chapter 1** begins by outlining recent advances in radiotherapy, clarifying the role and advantages of BNCT. It then discusses the current challenges of BNCT from an engineering perspective. The feasibility of the PSPC for the epi-thermal neutron spectrometry up to 1 keV, as well as the issues to improve its measurable range across the epi-thermal region was also introduced [*Y. Fujiwara et al., Journal of Instrumentation.* **20**, P08018 (2025)]. Finally, the chapter describes the motivation of this study, the accurate evaluation of the energy spectrum in the epi-thermal neutron region.

Chapter 2 outlines detectors to measure neutrons and methodologies to evaluate the neutron energy spectrum. For the neutron spectroscopy, a novel unfolding algorithm based on Bayes' Theorem was especially discussed in detail. In **Chapters 3 - 5**, we present a series of investigations related to the PSPC, while **Chapter 6** reports on the feasibility of measurements using the IP-ND.

First of all, in **Chapter 3**, a beam-type neutron source has been implemented to reduce the neutrons entering from the side surface of the detector, which is consider to be a trigger for discrepancies of estimated energy spectrum. We employed a Monte Carlo (MC) simulation code to design the collimator in order to develop a beam-neutron source based on our research accelerator. Setting parameters to (1) material, (2) Width, (3) Hole diameter, and (4) Distance from the neutron source, they were investigated to achieve the established design goals. We show that our designed collimator possesses high-beam characteristics, which can improve the estimation accuracy in lower-energy range [*Y. Fujiwara et al., KEK Proceedings.* 158-168 (2024)]. This beam neutron source can be applied not only for this purpose but also for other fundamental experiment in BNCT. when it comes to the application of the epi-thermal neutron spectrometry, numerical analysis found that further im-

provements were still necessary to cover whole range of epi-thermal neutrons. In addition, we discussed that more practical measuremntal system is required considering the reduction of detected neutrons due to the collimator.

In light of this, **Chapter 4** investigates the effectiveness of the development of the response function in MC Simulations, that is utilized to evaluate the contribution of neutrons entering from the side surface of the detector. Modeling the experimental system, the response function was calculated across the epi-thermal region. Numerical analysis using this designed response function revealed that the estimation accuracy was significantly enhanced [*Y. Fujiwara et al., Journal of Radiation Protection and Research.* **S1**, S43-S48 (2025)]. Furthermore, the presence of sodium, which has a high-resonance cross-section at 2.5 keV was found to be a crucial factor to determine the estimation performance in higher-energy range (over 1 keV neutrons). We therefore concluded that the design of response function in MC simulations, considering the actual experimental situation, was effective and also change its performance by the mixture of other nuclear interaction.

In **Chapter 5**, the feasibility of the combination of the PSPC and Activation foils to enhance the measurement accuracy and its measurable range (up to 100 keV scale) has been described. 10 materials were selected as activation foils, and then these activation rates were calculated in MC simulations. The response function was prepared by merging responses from PSPC and activation foils, and numerical analysis was performed based on this system. As a result, estimated spectrum can reproduce the reference spectrum, in spite of the wide energy range [*Y. Fujiwara et al., Applied Radiation and Isotopes.* **219**, 111719 (2025)]. Even when different physical mechanisms are involved, the findings demonstrate that they can coexist and be simultaneously employed in a mutually complementary way. By optimizing materials and their configurations, this specrometer system can be effective further.

Chapter 6 presents the concept of an approach implementing an IP-ND for the epi-thermal neutron spectroscopy, and experimental demonstration has been carried out in Kyoto University Research Reactor. The concrete idea is that the several moderators for neutrons are installed onto the IP (e.g. Boron) as a filter, and the energy spectrum is derived from the difference of the IP's response due to their thicknesses. As a result, both the pixel and Photostimulated luminescence values made a significant difference due to the boron filters. Also, the energy deposit was decreased at this region; thus, the effectiveness of boron filters was sucessfully confirmed in both computationally and experimentally. In this way, the feasibility of this spectrometer system using IP-ND was proposed [*Submission*].

Finally, **Chapter 7** summarizes the works introduced in this Thesis and provides an perspective. In summary, the effectiveness of approaches and their mechanisms to enhance the estimation accuracy and to expand wide dynamic energy range have been demonstrated. We therefore concluded that the specrometer systems that are capable of covering wide dynamic energy range have been established. Also, this study lays the groundwork for evaluating the neutron field produced by the accelerator and the treatment effects in BNCT treatments.

List of Symbols

General Symbols

Φ	Neutron flux (m groups) ($cm^{-2}s^{-1}$)
n	groups of measured data ($1 \leq i \leq n$)
E	Neutron energy (eV, keV, MeV)
m	Energy bins ($1 \leq j \leq m$)
M	mass (g)
t	time (s)
T	Temperature (K)
P	Pressure (atm)
k	Boltzmann's constant
S	Source Area (cm^2) (Entropy used in MAXED code)
V	Volume (cm^3)
Vol	Voltage (V)
d	radius (cm)
θ	angle
Σ, σ	Macro/microscopic cross section (barn), variance for (σ)
λ	Decay constant (s^{-1})
l	mean free length (cm)
I	Neutron Intensity (1/s)
ε	detection efficiency
ϵ	counting error
N	Atomic density (m^{-3})
H, h_i	Pulse Height
χ	Chi-square value
μ	Average of the measurement data

PSPC-related Symbols

$\boldsymbol{Y}, [y_1 \cdots y_n]^T$	Counting value (Depth distribution)
x	Detector depths
$\boldsymbol{R_{pspc}}, r_{i,j}^{(PSPC)}$	PSPC response rate in i-th depth, j-th energy bins
R_A, R_B	Ratio of component A neutrons detected in PSPC
N_A, N_B, N_C	Number of Counts of each component in t sec irradiation
eff_i	correction factor for PSPC positional sensitivity
$\overline{C}$	Average counts measured in ^{3}He PSPC
$C_i(Pre1, Pre2)$	Raw data of the signal count in the preliminary experiments
$C_i(Ex), C_i(True)$	Raw data and subtracting backgrounds in validation experiment
c_i	Calculated ^{3}He(n,p)^{3}H response rate in MCNP
η	Statistical ratio of epi-thermal to fast neutrons
$\epsilon_{total}, \epsilon_{sys}, \epsilon_Y$	uncertainties in PSPC measurements

Activation Foils-related Symbols

$A, [a_1 \cdots a_k]^T$	Activation rate
$\boldsymbol{Z}, [z_1 \cdots z_{n+k}]^T$	Merged value of both depth distribution
$\boldsymbol{R^*}, r^*_{i,j}$	Merged Response matrix
$\boldsymbol{R_{foils}}, r^{(foils)}_{i,j}$	Response matrix of Activation foils
L_w	Foil length (cm)
L_t	Foil thickness (cm)
N_a	The number of activation
N_γ	The number of activation nuclides
I_γ	the emission ratio of γ rays
f_s	coefficient of the self-shielding effect
f_g	absorption probability of γ-rays inside the foil
ε_{ff}	detection efficiency in HP-Ge detector

Imaging Plate-related Symbols

$\boldsymbol{N}, [N_1 \cdots N_n]^T$	Spatial distribution of neutrons
$x,\ y$	Locations in IP-ND
PSL (x,y)	PSL values at position (x,y)
$PSL\ Corr$ (x,y)	Modified PSL values in each experiment
PSL(neutrons)	PSL values which came from the neutrons' contribution
N_{Gd}, N_{ND}, N_{MS}	Spatial distribution of gadolinium converter, ND in total, and MS
ε_n	The neutron absorption efficiency
ε_{cc}	color-center creation efficiency per captured neutron
ε_{PSL}	overall transmission efficiency through the data aquisition process
ω_0	Color center in IP
E_{sp}	secondary particles with total energy
σ_c	neutron capture cross section of the converter element
N_{PSL}	the number of PSL centers therein
ϕ_{PSL}	the molar fraction of PSL atoms
σ_{th}	Thermal cross section for compositions of IP (barn)
$\epsilon_{ROI}, \epsilon_{PSL}$	the standard error in the Pixel value
A_{Au}, A_{Au+Cd}	Activation rate for both Au foils and Au foils covered by Cadmium
M_{Au}, M_{Au+Cd}	Mass of both foils
E_{dep}	Energy deposition to IP
$R_{ND/MS}$	the ratio of the detection rate in both IPs
a, b	coefficient factor of the PSL value for E_{dep}
c	coefficient factor of the PSL value for neutron intensity

Other Unique Symbols

Φ_{ref}, Φ_{est}	Reference/Estimated neutron flux ($cm^{-2}s^{-1}$)
Φ_{true}	Obtained energy spectra divided by the diagonal matrix
Φ_{th}, Φ_{epi}	Neutron flux in thermal/epi-thermal neutrons ($cm^{-2}s^{-1}$)
$D_{fast}, D_{photons}$	Absorbed Dose by fast neutrons/photons
J_{total}	Neutron current in total
Ω	Sample space in probability
$P(A), P(B)$	Example events of probability
$W_{i,j}$	Weight factor in GRAVEL
Q_i	Reconstructed measured value (depth distribution in this study)
F, f_j	Diagonal matrix
it	Iteration times of unfolding algorithms
$G^{(it)}$	Denominator of RMSE value definition in the it-th iteration
u	the number of distributions to determine it
w	Weight for source definition in Appendix
$\overline{\Phi_{log}}$	Log-mean value of the reference spectrum
$f(x)$	Angular distribution calculated in MCNP

1 Introduction

1.1 Recent Progress in Radiotherapy

Cancer is one of the most common lifestyle diseases in the world, and the threat is increasing every year. The World Health Organization has forecasted that the number of cancer patients will reach 27 million per year in 2040 [1]. As cancer continues to be a major global health burden, the establishment of safe and precise treatment modalities is crucial not only for improving survival outcomes but also for maintaining patients' quality of life.

Nowadays, cancer therapies can be broadly categorized into three main types: surgical treatment, Chemotherapy, and radiation therapy. Surgical treatment is still the main approach for the cure and control of most solid cancers; however, removing cancers and surrounding normal regions not only loses their functions, but also accelerates the risk of recurrence [2]. Chemotherapy primarily works by preventing cancer cells from further growth and division. However, doctors should be careful about the dosage and timespan of this treatment because it has been observed that the medications given at very high doses caused numerous side effects and harm to other healthy cells [3]. Despite enormous applications, most chemotherapies are given to prolong and ease the patient's survival, hence called "palliative chemotherapy" [4].

Radiotherapy aims to use ionizing radiation to destroy malignant cells. It deposits energy in cancer cells or tissues, which can kill them or cause genetic changes. One of the advantages is that radiotherapy allows the selective damage of tumor cells with little impact on normal cells. Normal cells can repair themselves and retain their normal function faster than tumor cells after irradiation. Therefore, radiotherapy is used for palliative therapy as well as curative therapy [5].

Radiotherapy is separated into 3 clinical modalities of radiation therapy: external beam radiation therapy (EBRT), brachytherapy, and systemic radio nuclide therapy. The common approach is EBRT, where radiation such as X-rays, photons, protons, and neutrons is delivered from outside the body. Recent technological advances, for example, 3D Conformal Radiotherapy (3D-CRT), intensity-modulated radiation therapy (IMRT), volumetric-modulated arc therapy (VMAT), and stereotactic body radiotherapy (SBRT), allow radiotherapy to deliver as much dose to the tumor cells whilst sparing normal cells. In brachytherapy, radiation is delivered from inside the body by radioactive sources, sealed in catheters or seeds, directly into the tumor site. In our university, Astatine-based targeted alpha radiotherapy has been developed for the treatment of thyroid cancer [6]. Both EBRT and brachytherapy target cancer at the macroscopic level, based on radiographic imaging such as computed tomography (CT) or magnetic resonance imaging (MR), called as image-guided radiation therapy, while systemic radionuclide therapies carry radioactive isotopes to the cell via a patient's blood supply.

Furthermore, recent technical innovations in computing, robotics, imaging allow EBRT to integrate medical images into treatment machines directly, as illustrated in Figure 1.1. Such CT and MR imaging system are included in treatment machines,

which have a competitive quality of diagnostics system, and radiation oncologists can design the treatment planning system in each day based on the machine performance. These systems have been designed to achieve strong, uniform magnetic fields for imaging without hindering with the acceleration and transport of electrons which are necessary for radiation beam production [7].

With these advances, radiotherapy has become a major option for cancer treatment. However, the risk of radiation exposure is unavoidable, even though it can be minimized. Figure 1.2 the depth – dose distribution in photon- and hadron-based radiotherapy. In photon therapy, the dose peaks at a shallow depth and remains relatively high at deeper locations. In contrast, particle therapy can concentrate the dose at a specific depth due to the characteristics of the Bragg peak. To match the treatment volume with the tumor size, the Bragg peak is broadened to form a spread-out Bragg peak (SOBP). Nevertheless, caution is required regarding the potential damage to surrounding normal tissues. These treatments are particularly limited in treating brain cancers such as glioblastoma, which tend to infiltrate surrounding tissues shortly after onset. Furthermore, as noted in [8], the official dose limits make it nearly impossible to treat recurrent cancers. To address these challenges, there is increasing demand for targeted therapies.

Boron neutron capture therapy (BNCT) provides an alternative and unique approach by delivering charged particles at the intracellular level, directly inside the tumor. This study focuses on BNCT, which is safe, highly effective, and clinically superior.

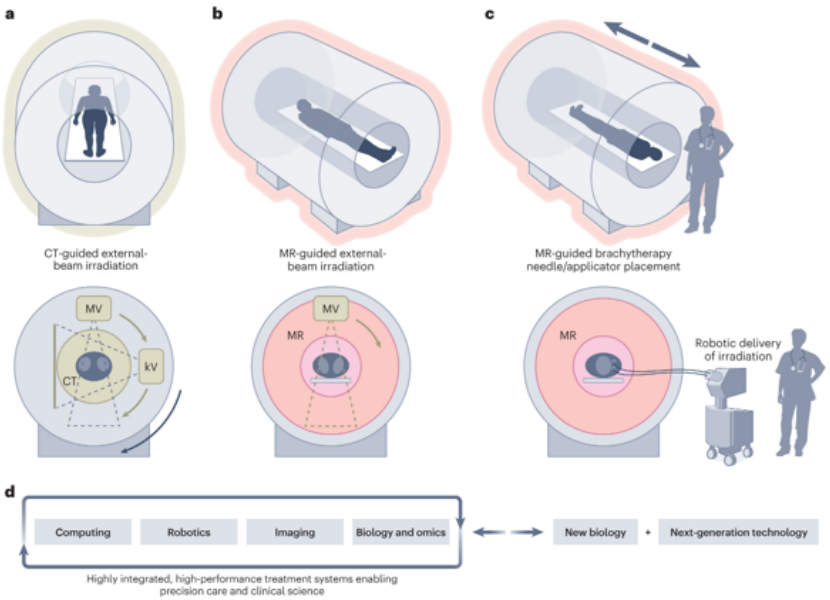


Figure 1.1: Technological convergence of image-guided IMRT. This figure was extracted from Ref. [7].

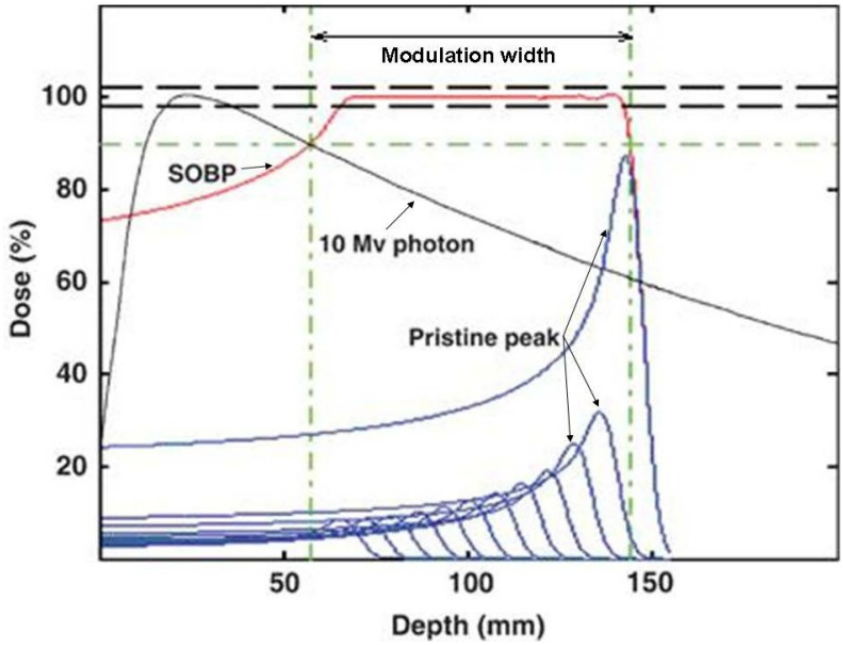


Figure 1.2: An example of the depth-dose in each radiotherapy. In particle therapy, the tumor is aligned with the region of high dose within the SOBP, thereby enabling the dose to be concentrated on tumor cells while minimizing damage to surrounding normal tissues. This figure was extracted from Ref. [9].

1.2 Boron Neutron Capture Therapy (BNCT): Principle and Uses.

Figure 1.3 shows the principle of BNCT treatments. BNCT is based on the capture and fission reactions that occur when nonradioactive ^{10}B is irradiated with thermal neutrons, eventually producing a high-energy alpha ray and ^{7}Li nuclei. The nuclear reaction is as follows:

$$^{10}\mathrm{B} + n \rightarrow {}^{7}\mathrm{Li} + \alpha + 2.79MeV \tag{1.1}$$

$$^{10}\mathrm{B} + n \rightarrow {}^{7}\mathrm{Li}^{*} + \alpha \rightarrow {}^{7}\mathrm{Li} + \gamma(478\,\mathrm{keV}) \tag{1.2}$$

Alpha particles and lithium nuclei are charged particles with high linear energy transfer (LET) and relative biological effectiveness (RBE) that produce closely spaced ionizations near the reaction, within the range of 5 μm and 9 μm, respectively. The range of tumoricidal radiation is limited within boron-containing cells. Moreover, human tissues contain plenty of ^{1}H (0.33 barns) and ^{14}N (1.7 barns), and their neutron capture cross sections are small enough that reactions with these elements don't occur commonly to produce lethal radiation damage to normal tissues. In contrast, ^{10}B has an exponentially high cross section (3880 barns) and is preferentially retained in tumor cells. Therefore, in principle, the nuclear reaction between ^{10}B drugs and neutrons occurs only in tumor cells with little damage to the normal cells.

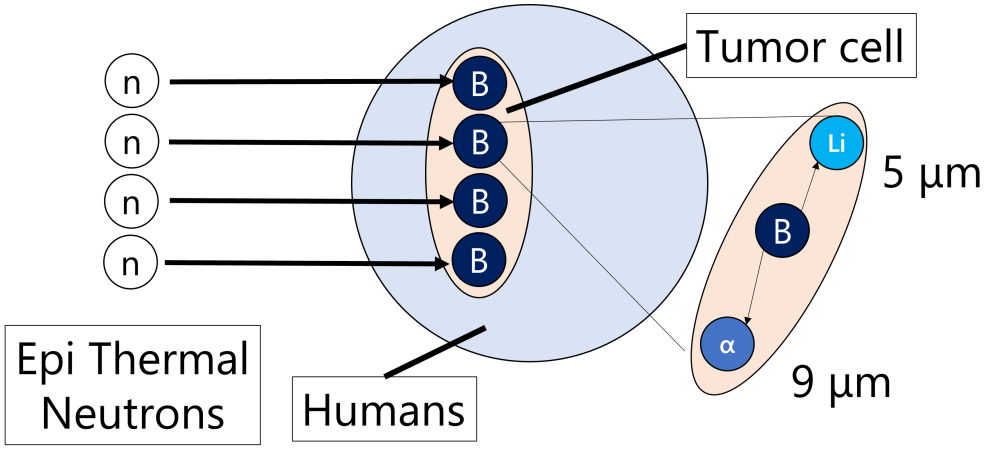


Figure 1.3: BNCT principle illustration.

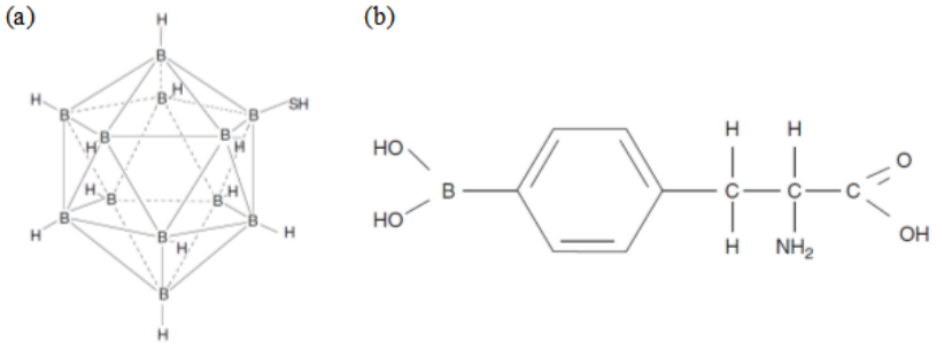


Figure 1.4: Structural formula of two BNCT drugs. (a) BSH and (b) BPA. These figures were extracted from [10].

The safety and effectiveness of BNCT are ensured based on this principle, which was proposed in the mid-1930s by Gordon Locher, four years after the discovery of the neutron by James Chadwick [11, 12]. Neurosurgeon William Herbert Sweet and physicist Gordon Lee Brownell, of Massachusetts General Hospital and Massachusetts Institute of Technology (MIT), respectively, conducted the first clinical trials involving BNCT, using the Brookhaven Graphite Research Reactor in 1951 [13, 14] After performing the primary debulking craniotomy on patients with high-grade glioma in Cambridge, Massachusetts, Sweet transported them to Upton, New York, for the intravenous infusion of ^{10}B-enriched borax (sodium tetraborate). Then, he exposed his patients to a single fraction of thermal neutrons from the experimental research reactor. None of the patients treated in these first clinical trials survived beyond 1 year, and all experienced severe toxicities. It was considered that the reason for these poor outcomes came from subpar tumor-to-blood ratios (TBRs), with surgical debulking compromising the compartmentalization of boron [15]. In addition, it is important to note that thermal neutrons do not penetrate deeply; to deliver an adequate dose, open craniotomies with exposed surgical cavities were required.

Sweer's initial work and awareness of his limitations led to a focus on improving the selectivity of boronated components, as well as the drug delivery system.

Although the research interest declined in the US, international collaborations were carried out. Decades later, Hatanaka presented some remarkable clinical results that had never been reported in high-grade gliomas; while most of the patients treated had astrocytoma with a few glioblastomas, they reported a median survival of 21.3 months [16]. These outstanding results had been achieved by the enhanced pharmacokinetics of sodium borocaptate (BSH, $Na_2B_{12}H_{11}SH$) [17]. A biodistribution study of BSH in patients with glioblastoma revealed that the tumor to normal brain ratio was as high as 40 to 1 ([18, 19]). Soon after, a second drug was introduced by Japanese dermatologist Yutaka Mishima. He experimented with perilesional injections of 4-borono-d, l-phenylalanine (BPA) in malignant melanomas, one of the first extracranial uses [20]. It became the most widely used boron compound after it was found to be taken up by other historical tumor histological patterns [21]. Structural formulas of two fundamental BNCT drugs, BSH and BSA were depicted in Figure 1.4.

Nowadays, l-BPA conjugating fructose to improve its hydrophilicity (l-BPA-F) is the most prominent boronated compound utilized in clinical trials [22, 23]. Additionally, some companies are developing such boron drugs, including AstraZeneca and Stella Pharma. Clinical trials have been carried out with these two boron drugs, mainly based on the research reactors; however, reactor-based BNCT reflects the political situation. Indeed, most of the research reactors for BNCT clinical trials were shut down, leaving the Tsing Hua Open-pool Reactor in China or RA-6 in Argentina [24, 25]. To address this problem, Accelerator-Based BNCT (AB-BNCT) is being developed worldwide [10].

1.3 Development of Accelerator-Based BNCT and Its Issues

In AB-BNCT, neutrons are produced through nuclear reactions between accelerated particles and target materials such as lithium or beryllium. These neutrons are then moderated to the appropriate energy levels for treatment within the Beam-Shaping Assembly (BSA).

Japan plays a pivotal role in developing AB-BNCT systems [26, 27, 28, 29, 30]. Kyoto University developed the first recognized accelerator-based epi-thermal neutron source with Sumitomo Heavy Industries, Inc. in the world, which is named Cyclotron-based neutron source (C-BENS) [26]. C-BENS utilized Beryllium as a target where neutrons are produced in the ^{9}Be (p, n) ^{9}B nuclear reaction. Kumada et al. applied a linac-based accelerator for the AB-BNCT system [27]. Recent AB-BNCT systems installed a Lithium target to produce neutrons emitted from the ^{7}Li (p, n) ^{7}Be nuclear reaction [28, 29, 30]. Herein, the accelerator for AB-BNCT developed in Therapeutics Inc. was shown in Figure 1.5. Lithium targets can produce a higher yield of neutrons compared to beryllium. Additionally, the maximum energy of the emitted neutrons is relatively low, around 1 MeV, which is advantageous over Be-based AB-BNCT systems. As a result, the requirements for

the Beam-Shaping Assembly (BSA) can be relaxed. Globally, commercial companies developing Li-based AB-BNCT systems, such as Neutron Therapeutics Inc. and TAE Life Sciences, are emerging, and their systems are currently being installed in medical facilities [30, 31, 32].

Clinical trials have also been carried out using these kinds of AB-BNCT systems [34, 35, 36]. The JHN002 trial was the first trial to explore an epithermal accelerator-based neutron source [34]. Treatments were carried out for patients with recurrent squamous cell carcinoma (R-SCC) or with recurrent/locally advanced non-squamous cell carcinoma (R/LA-nSCC) of the head and neck. As a result, the objective response rate (ORR) was 71%, and complete response/partial response were 50%/25% in R-SCC and 8%/62% in R/LA-nSCC. The 2-year overall survival for R-SCC and R/LA-nSCC was 58% and 100%, respectively. Kawabata et al. operated clinical trials for 27 patients with recurrent malignant glioma (MG) (primarily glioblastoma (GB), JG002). The result showed that the 1-year survival rate and median overall survival (OS) of the recurrent GB cases in this trial were 79.2% (95% CI: 57.0 – 90.8) and 18.9 months (95% CI: 12.9 – not estimable), respectively, whereas those of JO22506 were 34.5% (90% CI: 20.0 – 49.0) and 10.5 months (95% CI: 8.2 – 12.4), respectively [35]. Kashihara et al. applied AB-BNCT for the cutaneous angiosarcoma and malignant melanoma. 10 patients (scalp angiosarcomanine, forefinger malignant melanoma: one) were included in this trial, and the ORR within 180 days was 70 % [36]. As described, AB-BNCT also has high effectiveness for a variety of cancer treatments. Thanks to this remarkable progress, the Japanese government decided that AB-BNCT treatments were covered by insurance in 2020.

With the big wave of accelerators designed for BNCT in a clinical setting, centers are implementing patient positional systems, computerized dose calculation, image-based patient-specific treatment planning systems (TPS), and neutron beam spectrum. It is important to note that these systems depend on each center because of unique neutron sources, types of boron carriers, and cancer sites. A key difference from TPS in photon therapy is the presence of both neutrons and photons with wide energy ranges. Conventionally, these mixed beam properties were evaluated in nonhuman experimental RBE and then turned into humans by appropriate weighting [37]. Since BNCT delivers highly localized doses to tumor cells, the neutron distribution becomes macroscopically inhomogeneous. As a result, the conventional concept of absorbed dose, such as that used by Rogus et al., is not directly applicable. Therefore, it has been suggested that the biological effectiveness of BNCT should be evaluated using a microdosimetric approach, as is done in hadron therapy [38].

This study focuses on the neutron beam spectrum. The subsequent section provides an overview of prior methodologies and emphasizes the originality of the proposed approach.

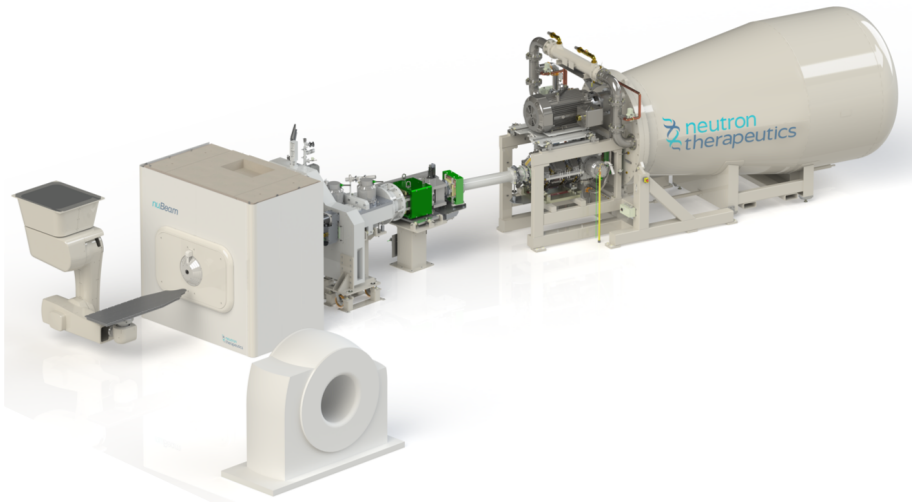


Figure 1.5: An accelerator for AB-BNCT treatments developed in Neutron Therapeutics Inc. This picture was extracted from [33].

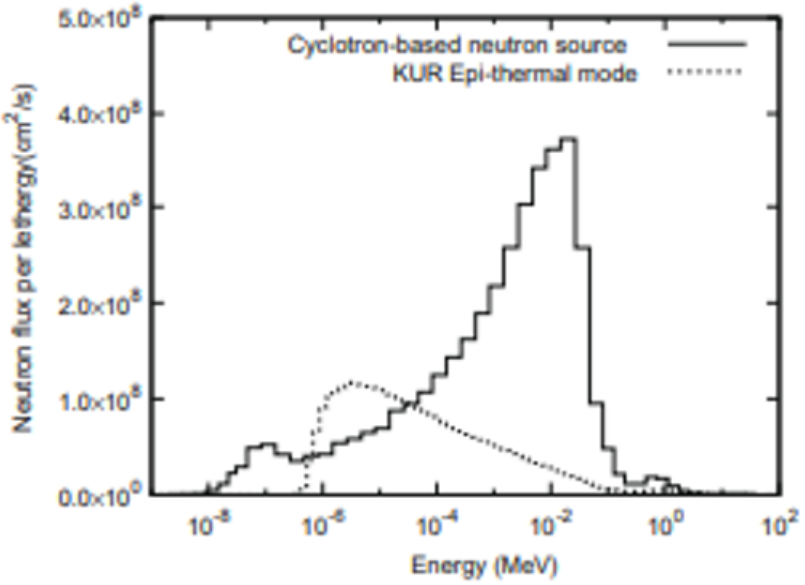


Figure 1.6: Comparison with neutron spectrum for KUR and CBENS. This picture was extracted from [39].

Table 1.1: IAEA recommendations for the neutron beam properties [40].

Characteristics	Recommended Values
Φ_{epi}	$\geq 5 \times 10^8$ $(n \cdot \mathrm{cm}^{-2} \cdot \mathrm{s}^{-1})$
D_{fast}/Φ_{epi}	$\leq 7 \times 10^{-13}$ $(\mathrm{Gy} \cdot \mathrm{cm}^2)$
D_{photon}/Φ_{epi}	$\leq 2 \times 10^{-13}$ $(\mathrm{Gy} \cdot \mathrm{cm}^2)$
Φ_{th}/Φ_{epi}	≤ 0.05
J_{total}/Φ_{epi}	≥ 0.7

1.4 Evaluation of Neutron Energy Spectrum in the Epi-Thermal Range

It has been reported that neutron energy has a crucial impact on RBE values [41], so this characteristic is important for the assessment. In addition, transition to accelerators makes this even more significant. Since epi-thermal neutrons cannot be obtained directly, moderators should be installed; however, they should be more compact than those of accelerators because of the capacity of hospitals. Therefore, as illustrated in Figure 1.6, the the energy peak of neutron flux in the accelerators for AB-BNCT is likely to shift to higher energy than those of reactors. In light of this, the International Atomic Energy Agency has determined requirements for the criteria of AB-BNCT [40], as shown in Table 1.1.

Previous studies assessed the neutron energy spectrum using the multifoil activation method, a Bonner sphere spectrometer (BSS), or the adjustment method [42, 43, 44, 45, 46, 47]. Principles of these approaches are discussed in Section 2.4, but in general, it is controversial in the measurement performance, and also these Spectrometer required several times of experiment. That is not convenient, and experimental situation is different in each time. Therefore, a new-type of neutron spectrometer in epi-thermal energy range is one of the crucial issues for the safe treatment in BNCT.

In light of this, this study suggests the application of the position-sensitive proportional counter (PSPC). This device detects the location of interactions within the ^{3}He gas. Given that ^{3}He has a high nuclear reaction cross-section and 1:1 correspondence with the neutron energy based on the 1/v rule [48], the depth-dependent signal distribution (referred to as "depth distribution" hereinafter) provides neutron energy information when neutrons enter the ^{3}He PSPC parallel to its axis. The neutron energy spectrum is reconstructed from the signal distribution using a spectrum unfolding technique based on the response function of the spectrometer [49]. ^{3}He PSPCs have been employed for various purposes, such as the characterization of neutron scattering [50]. In the context of neutron spectrometry, a ^{3}He PSPC was utilized as the BSS detector owing to its high nuclear reaction cross-section for thermal neutrons [46, 51]. However, the novel spectrometer using a ^{3}He PSPC does not require any moderators, unlike BSS, and enables the determination of the neutron energy spectrum through a single experiment. Therefore, this spectrometer has the potential to overcome the difficulties of previous methods, with high measurement accuracy and the ability to cover wide energy ranges. Detailed theory and Methodologies are presented in **Chapter 2**, and the experimental data processing in PSPC was discussed in **Appendix A**.

To demonstrate this spectrometer, A validation experiment have been performed [52]. This study implemented this PSPC and the depth distribution was measured, as illustrated in Figure 1.7. Then, the energy spectrum was estimated, and compared with the reference spectrum (See Figure 1.8). While the experimental depth distribution could be reproduced by the simulation results, the estimation performance was insufficient to conclude the feasibility of the spectrometer over a wide

energy range (up to 10 keV). Although the estimated energy spectrum can reproduce the reference spectrum up to 1 keV, there are large discrepancies in the higher energy region (over 1 keV). Still, further development and modification were found to be necessary to fully cover the epi-thermal range.

Additionally, since conventional spectrometers require complex data-processing procedures, there has been a strong demand for the development of spectrometers that enable simpler and more straightforward data analysis. This demand motivates the investigation of the feasibility of neutron-detection imaging plates (IP-NDs), which allow neutron information to be obtained simply by reading the PSL distribution using a dedicated readout system.

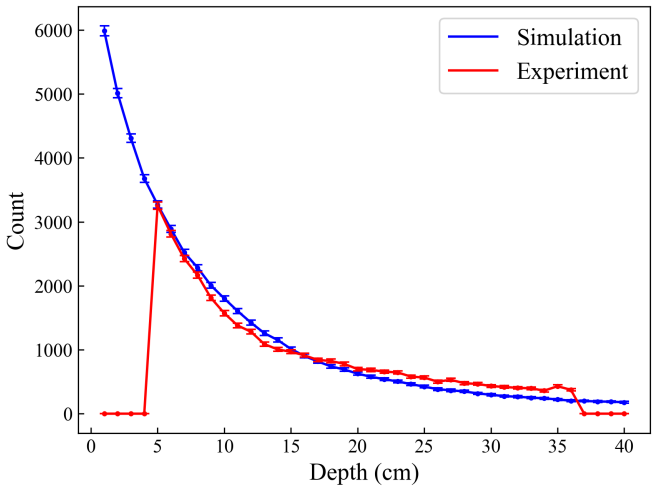


Figure 1.7: Comparison of the Depth distribution between experimental and simulation results.

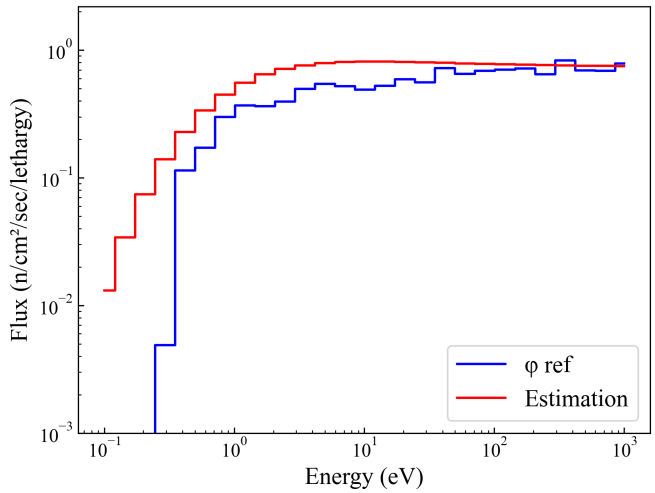


Figure 1.8: Comparison of Energy spectrum between $\boldsymbol{\Phi_{est}}$ and $\boldsymbol{\Phi_{Ref}}$.

1.5 Research Objectives

This research aims to develop and enhance a measurement method for the neutron energy spectrum in the epi-thermal range based on the ^{3}He PSPC. Previous studies have shown the feasibility of this approach both numerically and experimentally [49, 53]. Murata and Miyamaru proposed this concept with a numerical experiment, indicating that this spectrometer could evaluate the energy spectrum by at least 100 eV [49]. In order to verify this approach, Osawa fabricated an epi-thermal neutron field in our laboratory [53], and the first validation experiment has been performed [52]. As a result, it was revealed that this spectrometer demonstrated the agreement at least up to 1 keV; however, discrepancies between the reference spectrum and experimental result are at most 40%. Therefore, it is mandatory to enhance the accuracy of this approach.

This thesis suggested three approaches to coping with this issue. The first approach is the development of a sharp beam-type neutron source [53]. This spectrometer assesses neutrons incident from the entrance to represent the energy-dependent depth distribution. It requires a high-rate beam property to obtain such distributions in experiments. However, it's not practical to install this kind of collimator in the real facilities. Therefore, I proposed to evaluate the response function of this spectrometer in the Monte Carlo simulations (MC simulations) as a second approach [54]. In MC simulations, it enables us to assess the probabilistic behavior of each particle. Therefore, the information of neutron incidents from the side, which are regarded as the error in approach 1, can be included in the designed response function. Furthermore, it is well known that actual accelerators for BNCT cannot completely reduce their neutrons' energies, and neutrons over 10 keV remain. Therefore, my approach is to combine multiple activation methods with my PSPC-based spectrometer to expand the measurement energy range [55]. It is important to mention that these two approaches come from different physical rules, activation and absorption.

Moreover, this study also considered IP-ND as a spectromter for the low-energy range. Using IP's high spacial resolution, **Chapter 2** explains the way to obtain the energy spectrum in PSPC and IP-ND. **Chapters 3, 4, and 5** elaborate on the details of each approach in PSPC, and **Chapter 6** described an novel approach of IP-ND. Then, **Chapter 7** concludes this study and mentions further developments.

2 Theory: Neutron Detectors and Spectrum Unfolding Methods

2.1 Introduction

This section describes detectors and analytical approaches to obtaining the neutron energy spectrum. In principle, the neutrons energy cannot be identified directly; indeed, neutrons themselves cannot even be detected due to their lack of electric charge. Instead, charged particles produced through nuclear reactions are being measured, for example, the ^{3}He(n, p)^{3}H reaction in this study [48]. The neutron energy spectrum is then derived from these signal distributions through a process known as "spectrum unfolding." Various detectors and unfolding techniques have been developed to estimate the neutron energy spectrum based on such nuclear reactions. This chapter summarizes the general concepts and associated challenges of these methods and presents the novelty of the approach adopted in this study.

2.2 Conventional Neutron Detectors

2.2.1 Scintillators

A scintillator is composed of a detection element, a scintillator, and a photosensitive device, a photoelectronic amplifier. Scintillators include a tiny amount of impurities called activator that generated the energy level between the valence and conduction band. When ionizing radiations irradiate to a scintillator, it gives electron-hole pairs, making the electrons being push up into the conductor, and the holes ionize the impurity. The electrons pushed up into the conductor recombine with the ionized impurity to form its excited state. The light emitted when the impurity in the excited state transitions to the ground state is named the "scintillation ray". Signals are detected by connecting them to an electrical circuit. The meschanism of scintillation rays generation was illustrated in Figure 2.1.

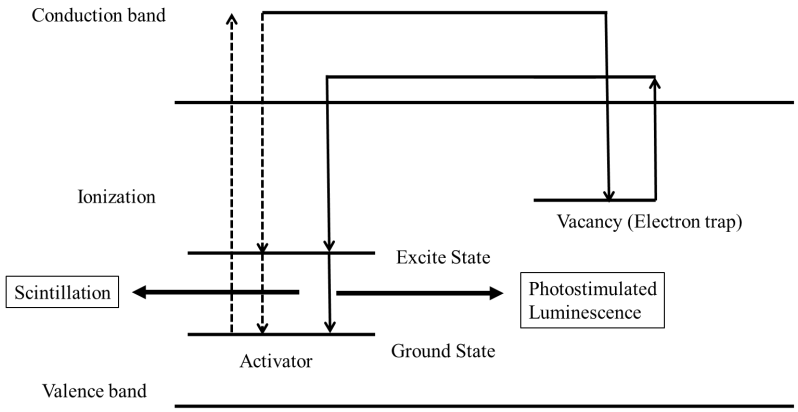


Figure 2.1: Processes on the scintillation rays and photostimulated luminescence. (details in **Section 2.2.4**).

Scintillators are classified into inorganic/organic types, while CsI or NaI, exemplify inorganic scintillators, and organic ones are compounds of hydrogen and carbon. In the context of neutron spectroscopy, organic scattering was selected as a high-energy neutron spectrometer because neutron elastic scattering on the hydrogen nucleus produces scattered neutrons and recoil protons. According to [56], organic scintillators enable the evaluation of several kinds of neutron energy spectra with high accuracy. Besides, for the BNCT safe analysis, a LiCaF scintillator was applied to evaluate the neutron ambient dose in the epi-thermal neutron field [57]. Now that its characteristics have also been elucidated, like in [58], the use of LiCaF scintillator is widespread. Moreover, a Single Photon Electronic Compton Tomography (SPECT) system for BNCT (BNCT-SPECT) is being developed by deploying a lot of scintillators, for instance, $Gd_3Al_2Ga_3O_{12}$: Ce (GAGG (Ce)) scintillator [59, 60] to evaluate local boron dose distribution in real-time. However, moderators are necessary to evaluate the neutron flux in a specific energy range, such as the Bonner Sphere Spectrometer (BSS), as introduced in **Section 2.4**.

2.2.2 Activation Detectors

Activation detectors detect neutrons via the neutron activation reaction for materials like Gold, Indium, etc. The induced γ-rays are detected in the Germanium detector or some scintillators. These materials have a high cross-section in a specific energy range for neutrons, so the signal counts represent the intensity of neutrons in this region. The use of only scintillators needs to be taken into account in the presence of a mixed radiation field of neutrons and γ-rays, generated in the detection process. However, activation detectors avoid discriminating against each signal. In general, they are used in the shape of thin foils to maintain the neutron field, and this approach of the activation foils is also applied for the neutron spectroscopy in BNCT, which is shown in **Section 2.4**.

The principle of the activation detector is described below. At a given time t, the number of reactions occurring within an infinitesimal time interval can be expressed by Equation (2.1), where R denotes the reaction rate per unit time.

$$R(t)dt = N \cdot V \int \varphi(E,t)\sigma(E)dEdt \tag{2.1}$$

Where N is the atomic density of the target nuclei, $\varphi(E,t)$ is the neutron flux at energy = E, and $\sigma(E)$ is the activation cross-section, V is the volume of a sample foil. Assuming the irradiation time as t_m, the number of activation nuclides (N_a) is the integral value of Equation (2.1), considering the decay during the activation, as follows

$$N_a = \int R(t) \cdot exp(-\lambda(t_m - t))dt \tag{2.2}$$

$$= N \cdot V \int \int \varphi(E,t) \cdot \sigma(E) \cdot exp[-\lambda(t_m - t)]dEdt \tag{2.3}$$

Where λ is the decay constant. There are two solutions of Equation (2.3) for neutron's intensity.

- Constant neutron intensity
  In this case, R also becomes constant according to Equation (2.1). Therefore, Equation (2.3) can be written in

$$N_a = N \cdot V \int \varphi(E) \cdot \sigma(E) dE \int_0^{t_m} exp[-\lambda(t_m - t)] dt \tag{2.4}$$

$$= \frac{N \cdot V[1 - exp(\lambda t_m)]}{\lambda} \int \varphi(E) \cdot \sigma(E) dE \tag{2.5}$$

$$= \frac{N \cdot V \cdot \varphi[1 - exp(\lambda t_m)]}{\lambda} \int P(E) \cdot \sigma(E) dE \tag{2.6}$$

  Where φ is the neutron intensity, and P(E) is the probability that neutrons are irradiated to the activation foil at energy E. Therefore, R can be derived from the following Equation (2.8).

$$R = \int P(E)\sigma(E) dE \tag{2.7}$$

$$= \frac{N_a \lambda}{N \cdot V \varphi[1 - exp(\lambda t_m)]} \tag{2.8}$$

- Time-dependent neutron intensity
  Since the energy spectrum at time = t is constant, the neutron flux ($\varphi(E, t)$) can be described as

$$\varphi(E, t) = \varphi(t) P(E) \tag{2.9}$$

  Equation (2.3) is rewritten by Equation (2.9) as follows:

$$N_a = N \cdot V \int \varphi(t) \cdot P(E) \cdot \sigma(E) dE \int_0^{t_m} exp[-\lambda(t_m - t)] dt \tag{2.10}$$

$$= N \cdot V \int P(E) \cdot \sigma(E) dE \int_0^{t_m} \varphi(t) \cdot exp[-\lambda(t_m - t)] dt \tag{2.11}$$

  Therefore, R is obtained from

$$R = \int P(E)\sigma(E) dE \tag{2.12}$$

$$= \frac{N_a \lambda}{N \cdot V \int_0^{t_m} \varphi(t) exp[-\lambda(t_m - t])} \tag{2.13}$$

Provided that the measurement of radioactivity is performed in a HP-Ge detector, it measures the count rate of γ-rays based on the decay system of activation nuclide. When this measurement is conducted in t_m seconds after the cooling time in t_c seconds, The number of γ-rays are obtained from the following Equation.

$$N_\gamma = N_a \cdot I_\gamma \cdot exp(-\lambda t_c)[1 - \exp(-\lambda t_m)] \tag{2.14}$$

The counting rate in HP-Ge detector (C) is given in

$$C = \varepsilon_{ff} \cdot N_\gamma + \text{Background} \tag{2.15}$$

Where ε_{ff} is the detection efficiency of γ-rays, derived from

$$\varepsilon_{ff} = f_s \cdot f_g \tag{2.16}$$

Where f_s is coefficient of the self-shielding effects of γ-rays, f_g is the probability of the shielding of γ-rays by itself.

Therefore, N_a can be obtained from Equations (2.14 - 2.16),

$$N_a = \frac{\lambda(C - \text{Background})}{\varepsilon_{ff} \cdot I_\gamma \cdot exp(-\lambda t_c)[1 - \exp(-\lambda t_m)]} \tag{2.17}$$

N_a can be obtained from Equations (2.8, 2.13), and this relationship allows us to measure neutrons. However, as shown in Equation (2.17), it requires complex data processing and needs to consider several factors of the uncertainties.

2.2.3 Gas Detectors

Gas detectors acquire electrical signals by applying a high voltage to free electrons generated in the ionization from the interactions between neutrons and the inside gases. Typical examples include ionization chambers, proportional counters, and Geiger-Müller detectors. This section outlines the principle of a general proportional counter, which is often used as a neutron detector. Other detectors' principles are well described in [48].

Proportional counters may be filled with a mixture of noble gases, like Argon, or quench gases, for instance, carbon dioxide and methane, for ionization radiation detection. Interactions between incident radiation and the gas inside the detector produce ionization in the noble gas, resulting in a quantity of electron – ion pairs proportional to the total energy deposited in the gas. A positive voltage applied to the anode attracts the electrons, whereas the positive ions are drawn to the cathode. As electrons draw nearer to the anode, they gain enough kinetic energy, which is accelerated by the field, to ionize successive gas atoms. Thus, it causes an avalanche of charge near the anode. The resulting electrons are collected on the anode while

positive ions drift toward the cathode. The total charge can then be read by suitable electronics connected to the anode.

For neutron detection, it is filled with gases that have a high nuclear cross-section for neutrons, Boron (BF_3) or ^{3}He, etc. The ^{3}He proportional counter is a proportional gas that readily absorbs thermal neutrons. In the detection process, a proton and triton are emitted in diametrically opposite directions, with a combined kinetic energy of 764 keV, as shown in equation (2.18).

$$^3He + n =^3 He + p + 764\ keV \tag{2.18}$$

A phenomenon called the 'wall effect' occurs when one or both ions collide with the detector cathode before depositing their full energy in the gas volume. As a result, the total energy deposited in the gas may vary between the initial kinetic energy of the triton (191 keV) and the full energy of the reaction (764 keV). A detailed study of the wall effect is available in the work done by Shalev et al [61]. An example ^{3}He proportional counter, and its spectrum measured in this device is illustrated in Figures 2.2, 2.3.



Figure 2.2: PSPC used in this study, the length is 40 cm, and the pressure is 5 atm.

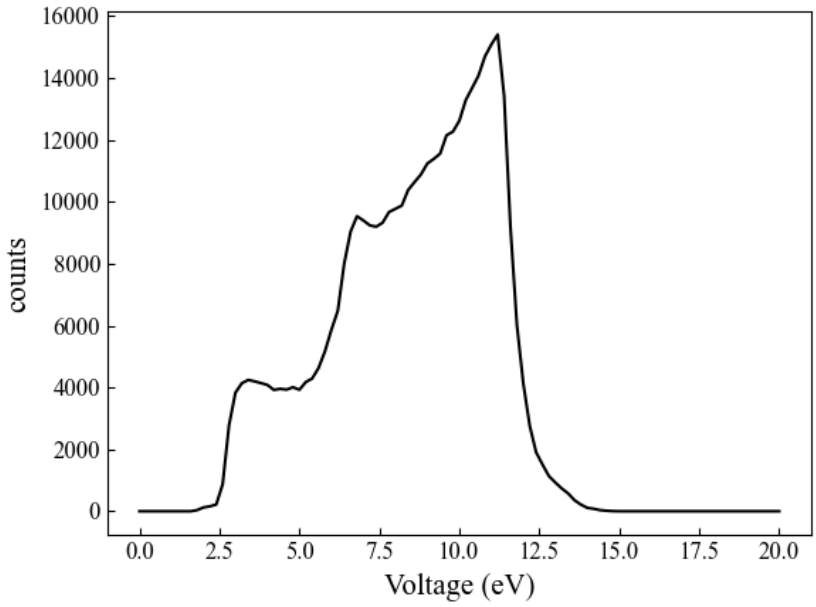


Figure 2.3: An example spectrum by PSPC. Wall effect represents the other two peaks in this Figure.

2.2.4 Imaging Plate

An Imaging Plate (IP) operates on a principle similar to that of scintillation detectors. When ionizing radiation is incident on the phosphor, electron – hole pairs are generated, impurities are ionized, and electrons are promoted to the conduction band, as described in **Section 2.2.1**. The main difference is that an IP detects photostimulated luminescence (PSL) from a photostimulable phosphor, such as BaFBr:Eu^{2+}. When the material is irradiated with a laser, it emits light (photostimulated luminescence) at a different wavelength. Since the photostimulable phosphor contains traps that capture electrons excited by ionizing radiation, no prompt scintillation light is produced. Instead, these trapped electrons are released upon laser stimulation, resulting in the emission of photostimulated luminescence.

The Imaging Plate is a film-like radiation image sensor composed of specifically designed phosphors that trap and store the radiation energy. The stored energy is stable until it is scanned with a laser beam, which releases the energy as luminescence. This phosphor technology was first applied in the medical X-ray diagnostic field, which can be applied for several technologies [62]. In the case of the X-ray imaging plate, called as BAS-MS, it has a high spatial resolution (0.2 mm, FWHM), a dynamic measurable range (1: 10^5), and no counting rate limitation. An X-ray imaging plate could be turned into a neutron detector when compounds include elements that can emit ionizing radiations such as ^{157}Gd (n, γ) ^{158}Gd or ^{6}Li (n, α) ^{3}H. The imaging plate neutron detector (IP-ND) has been developed in Fujifilm. Co. Ltd., and the characteristics have been examined [62, 63]. Advantages that are possessed in the X-ray imaging plate are also valid for IP-ND, so the IP-ND has been applied for the neutron radiography.

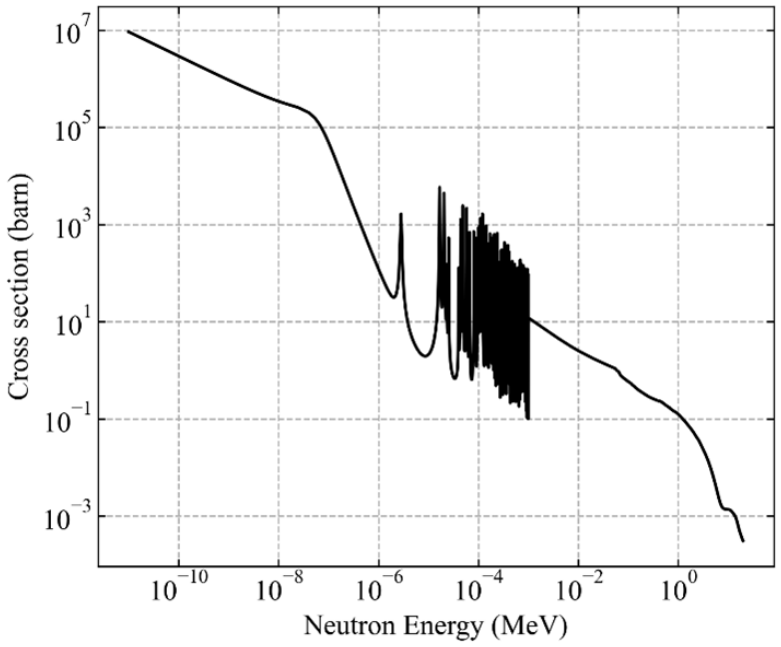


Figure 2.4: Cross-Section of ^{157}Gd, extracted from [64].

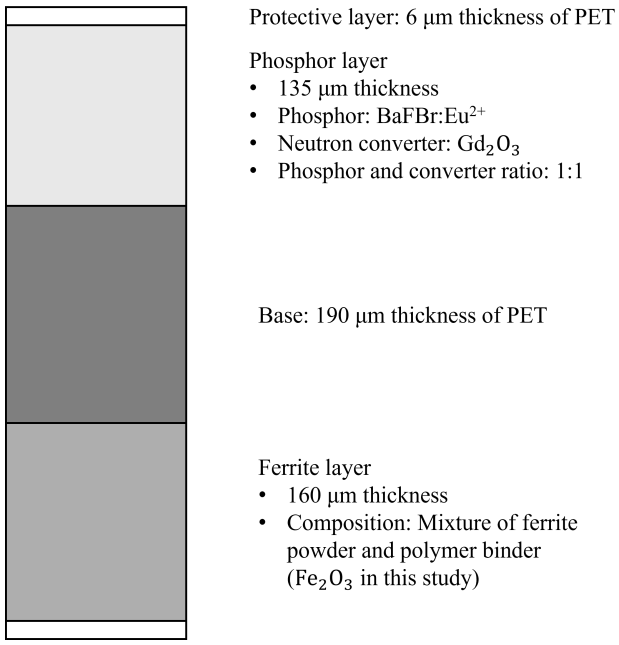


Figure 2.5: A sketch of the structure of IP-ND, based on Ref. [63].

Herein, the detection system of the IP-ND was introduced. Imaging plates with a Gd or Li converter (IP-ND) record the spatial distribution of γ-rays from nuclear reactions between neutrons and converter materials. ^{157}Gd has a high capture cross section for thermal neutrons (see Figure 2.4); thus, low-energy neutrons induce the above reactions and deposit energy to the IP. This study used BAS-ND (Fujifilm Co., Ltd.). BAS-ND consists of Gd_2O_3 as the neutron converter and BaFBr:Eu^{2+} as the phosphor layer with a thickness of 135 μm with 1:1 ratio of the converter and the phosphor [63]. The phosphor layer is covered by a 6-μm-thick polyethylene terephthalate (PET) protective layer. The support consists of a 190-μm-thick PET film. A ferrite sheet is attached to the back side of the IP to facilitate handling in the reader system. This structure was shown in Figure 2.5.

It is well known that the following fundamental processes occur in IP-ND [63]:

- **Neutron absorption by the converter and emission of secondary charged particles.**
  The neutron absorption efficiency ε_n is

$$\varepsilon_n = 1 - \exp(-N\,\sigma_c\,t), \tag{2.19}$$

  where N is the number density of converter atoms, σ_c is the neutron capture cross section of the converter element, and t is the phosphor-layer thickness. For simplicity, neutron absorption in non-converter constituents and neutron scattering are neglected. Let the sum of the number densities of the converter atoms and the PSL atoms (Ba) be n. Writing $N = (1 - \phi_{\mathrm{PSL}})\,n$ with ϕ_{PSL} being the molar fraction of PSL atoms, Equation (2.19) becomes

$$\epsilon_n = 1 - \exp\big[-(1 - \phi_{\mathrm{PSL}})\,n\,\sigma_c\,t\big]. \tag{2.20}$$

- **Creation of color centers in PSL by secondary particles.**
  Let ε_{cc} denote the color-center creation efficiency per captured neutron. If the energy required to create one color center is ω_0, secondary particles with total energy E_{sp} can at most form E_{sp}/ω_0 centers. Let V_{sp} be the volume traversed by the activated electrons and N_{PSL} the number of PSL centers therein. Then,

$$\varepsilon_{cc} \propto \begin{cases} \dfrac{E_{sp}}{\omega_0}, & N_{\mathrm{PSL}} > \dfrac{E_{sp}}{\omega_0}, \\ \dfrac{E_{sp}}{\omega_0}\,\phi_{\mathrm{PSL}}, & N_{\mathrm{PSL}} \leq \dfrac{E_{sp}}{\omega_0}. \end{cases}$$

- **Stimulated emission in read-out by incident laser light.**
  Multiple processes (scattering/absorption of the incident light, secondary excitation of color centers, Eu^{2+} emission, etc.) are lumped into an overall transmission efficiency $\varepsilon_{\mathrm{PSL}}$. The PSL intensity is then

$$\mathrm{PSL} = \varepsilon_n\, \varepsilon_{cc}\, \varepsilon_{\mathrm{PSL}}. \tag{2.21}$$

In making signals, IP-ND uses electrons from the ionization Eu^{2+} to Eu^{3+}. Neutron irradiation induces the ^{151}Eu (n,γ) ^{152}Eu and ^{153}Eu (n, γ) ^{154}Eu reactions [63], which may cause ionization and produce the signal for the BAS-ND. he contribution of these reactions to the IP signal is estimated assuming that one reaction produces one signal, although this assumption may lead to overestimation. Fujibuchi et al., compared the atomic density N and the cross-section for thermal neutron of these nuclei to estimate the signals produced by this reaction, indicating that the Nsigma value of ^{157}Gd (n, γ) ^{158}Gd is much higher than that for ^{151}Eu (n,γ) ^{152}Eu and ^{153}Eu (n, γ) ^{154}Eu reactions (See Table 2.1) [65]. Therefore, contribution of neutrons to Eu was regarded as extremely small enough to be ignored.

When the neutron capture reactions occur in ^{157}Gd, about 20 % of the generated ^{158}Gd nucleus were left in excite state. It releases several types of radiation as follows:

$$^{157}Gd + n \rightarrow ^{158}\,Gd + \gamma + X - rays + ICe^{-} + ACKe^{-} \tag{2.22}$$

Where "IC" means internal, "ACK" is Auger Coster – Kronig (ACK) conversion electrons [66, 67]. These electrons ionize Eu^{2+} to Eu^{2+}, which produces the IP-ND signals. Thus, the neutron-induced spatial distribution on the IP is assumed to reflect the number of neutrons traversing the phosphor layer.

Table 2.1: Gd and Eu cross sections for thermal neutrons (σ_{th}).

Reactions	Planar density of target atom in the IP (atom cm^{-2})	σ_{th} (barn, $10^{-24} cm^2$)	Nσ_{th} (atom)
^{157}Gd (n,γ) ^{158}Gd	1.0×10^{19}	2.5×10^{5}	2.6
^{151}Eu (n,γ) ^{152}Eu	1.5×10^{17}	9.3×10^{3}	1.4×10^{-3}
^{153}Eu (n,γ) ^{154}Eu	1.6×10^{17}	3.9×10^{2}	6.3×10^{-5}

When it comes to the application of IP for neutron detection/spectrometry, Fujibuchi et al., proposed a low-energy detector employing the BAS-ND, which also discriminates the gamma rays supplementary generated via the nuclear interactions between neutrons and moderators [65]. Ogino et al., performed the measurement of epi-thermal neutrons using IP-ND, which is for evaluating tritium breeding performance in the context of fusion engineering [68].

For BNCT applications, a multi-imaging plate system for BNCT irradiation field has been developed [69, 70, 71, 72]. This project aims to evaluate the quality assurance for BNCT, and IP was used instead of Au foils. Using BAS-TR, which is not equipped with the protection layer to detect the secondary particles such as α-rays generated by ^{10}B (n, α) ^{7}Li reactions. In this project, such secondary particles were measured in the BAS-TR by incorporating several neutron converters such as Boron and Lithium to get the sensitivity for wide-range energy of neutrons. These studies revealed that the evaluation of neutron dose in the epi-thermal neutron field was possible, and the discrimination of γ-rays and neutrons can be sucessfully performed by employing several-types of IP.

BAS-TR was also utilized as the spectrometer in higher-energy region, by measuring recoil protons. Nohtomi et al., have developed a unique approach to evaluate high-energy neutrons. The spectrometer consists of the BAS-TR and Acril crystal as the moderator [73]. The response function was built by the Monte Carlo Simulations by using the difference in the reaction characteristics for the neutron energy. This study shows the feasibility of the IP-based spectrometer for neutron spectroscopy.

As discussed, previous studies have almost utilized the BAS-TR for the evaluation of neutron's properties by measuring secondary charged particles generated in nuclear interactions of converter materials with neutrons. However, there is no spectrometer using IP for the low-energy neutrons, and this fact is our motivation to develop such system. In this study, we aim to apply IP-ND for the low-energy neutron spectrometry by using a novel technique focusing on the boron's characteristics. The details about the concept, detector set ups, and the feasibility analysis will be described in **Chapter 6**.

2.3 Spectrum Unfolding Process

2.3.1 General Concepts

The pulse height spectra measured in any radiation detectors are described as the convolution integral of the response function and the energy spectrum of the radiation. This relationship is given by the following Equation, letting the pulse height spectrum be denoted as $\frac{dN}{dH}$, the response function as R (H, E), and the energy spectrum as Φ (E).

$$\frac{dN}{dH} = \int R(H,E)\Phi(E)dE \tag{2.23}$$

The unfolding process means solving this Equation. If the energy traversing the detector (E_p) corresponds 1:1 to the pulse height spectra, the Equation (2.23) is

rewritten in

$$\frac{dY(E_d)}{dE_d} = \int_{E_p=E_{min}}^{E_p=E_{max}} R(E_p \rightarrow E_d) \frac{dY(E_p)}{dE_p} dE_p \tag{2.24}$$

Equation (2.24) is also called the first Fredholm integral Equation. This Equation is successive for E_p; however, experimental results are measured in the discrete spectrum, such as the histogram. Hence, energies are divided into several groups $(E_1, E_2, \cdots, E_j, \cdots, E_m)$, and the discrete spectrum (p_j) is created by integrating the energy spectrum in the following Equation (2.25),

$$p_j = \int_{\Delta E} \frac{dY(E_p)}{dE_p} dE_p \tag{2.25}$$

Identically, the pulse height spectra are made in the following Equation (2.26),

$$d_i = \int_{\Delta E} \frac{dY(E_d)}{dE_d} dE_d, \tag{2.26}$$

Where d_i is the *i-th* value of the pulse height ($1 \leq$ i $\leq$ n), and the division is generally carried out with the same lethargy, through this process, the Equation (2.24) is also described in the shape of the matrix:

$$Y(x) = \int R(x, E)\Phi(E)dE \tag{2.27}$$

$$\boldsymbol{Y} = \boldsymbol{R\Phi} \tag{2.28}$$

$$\begin{bmatrix} y_1 \\ \vdots \\ y_n \end{bmatrix} = \begin{bmatrix} r_{11} & \cdots & r_{1m} \\ \vdots & \ddots & \vdots \\ y_{n1} & \cdots & r_{nm} \end{bmatrix} \begin{bmatrix} \phi_1 \\ \vdots \\ \phi_m \end{bmatrix} \tag{2.29}$$

From Equation (2.29), the response function (R(d,E)) is also found to be discretized. The substance section introduces the way to solve this Equation (2.29).

2.3.2 Unfolding Algorithms

Since experimental results include several uncertainties, such as counting errors or those in the nuclear data, the neutron energy spectrum, Φ (E), cannot be obtained directly by deterministic operations. To address this ill-posed problem, several algorithms have been developed from a statistical perspective [74, 75, 76, 77, 78]. This section introduces these algorithms, including the Bayesian approach, which is applied in this study to solve the problem.

(A) MAXED

This concept was developed to apply the maximum entropy principle to the unfolding of neutron spectrometric measurements. In principle, the maximum

entropy seeks the solution to maximize the entropy (S), as given in

$$S = -\Sigma_j[\varphi_j^{est} \cdot \ln(\frac{\varphi_j^{est}}{\varphi_j^{ref}}) + \varphi_j^{ref} - \varphi_j^{est}], \tag{2.30}$$

Where φ_j^{ref} is the default spectrum, and φ_j^{est} is the solution spectrum. The characteristic of MAXED is to incorporate a priori information into φ_j^{ref} to ensure φ_j^{est} is non-negative and obtain the appropriate solution [77]. However, this approach has been recommended for a few-channel detector spectroscopy because this approach requires a lot of user-defined parameters and forces us to optimize them for each channel. Since the energy spectrum in the epi-thermal neutron range became successive, this concept might not be able to handle its sensitivity. Therefore, this study excluded this unfolding method.

(B) GRAVEL

This concept applied the least squares for the unfolding. In general, this approach attempted to solve this ill-posed problem by minimizing χ^2 given in

$$\chi^2 = (\boldsymbol{Y} - \boldsymbol{R\Phi})^{\boldsymbol{T}} \boldsymbol{C}(\boldsymbol{Y} - \boldsymbol{R\Phi}), \tag{2.31}$$

Where C is the covariance matrix of the measured data. As a representative, the GRAVEL code was developed for the HEPRO package made at CERN [78]. This study considered this algorithm because the least squares is a classical method for solving over-determined systems of linear equations. A uniformly distributed initial solution is appropriate for the iterations, and its amplitude can be of any value within computer precision. The algorithm adopts $\ln\varphi_j^{ref}$ instead of φ_j^{ref} in the iterations, ensuring the solution is non-negative. The solution is updated at each iteration according to

$$\varphi_j^{est(it+1)} = \varphi_j^{est(it)} \exp(\frac{\Sigma_{i=1}^N W_{ij}^{(it)} \ln(\frac{Y_i}{Q_i^{(it)}})}{\Sigma_{i=1}^N W_{ij}^{(it)}}), \tag{2.32}$$

Where *it* denotes the number of iterations. $W_{ij}^{(it)}$ is a weight factor defined by

$$W_{ij}^{(it)} = Y_i \frac{R_{ij}\varphi_j^{est(it)}}{Q_i^{(it)}}, \tag{2.33}$$

Where $Q_i^{(it)}$is the reconstructed position distribution obtained by multiplying the spectrometer response R_{ij} and the iterative solution $\varphi_j^{est(it)}$, expressed as

$$Q_j^{(it)} = \Sigma_{j=1}^M R_{ij}\varphi_j^{est(it)} \tag{2.34}$$

ALGORITHM 1: GRAVEL unfolding algorithm

Input: $\boldsymbol{y} \in \mathbb{R}^{n}_{\geq 0}$, $R \in \mathbb{R}^{n \times m}_{\geq 0}$, $\boldsymbol{\Phi}^{(0)}_{\text{est}}$, $\boldsymbol{\Phi}^{\text{ref}}$, N_{iter}
Output: $\boldsymbol{\Phi}_{\text{est}}$
Initialize $\boldsymbol{\Phi}^{(0)}_{\text{est}}$ as an uninformed distribution (e.g. $\Phi^{(0)}_{\text{est},j} = 1/m$)
$\text{RMSE}_{\text{prev}} \leftarrow \infty$ `// RMSE at iteration` $it - 1$
for $it = 0, 1, \ldots, N_{\text{iter}} - 1$ **do**
  $\boldsymbol{Q}^{(it)} \leftarrow R\,\boldsymbol{\Phi}^{(it)}_{\text{est}}$ `// predicted counts`
  for $j = 1, \ldots, m$ **do**
    $T_j \leftarrow \sum_{i=1}^{n} y_i \frac{R_{ij}\,\Phi^{(it)}_{\text{est},j}}{Q^{(it)}_i} \ln\left(\frac{y_i}{Q^{(it)}_i}\right)$
    $S_j \leftarrow \sum_{i=1}^{n} y_i \frac{R_{ij}\,\Phi^{(it)}_{\text{est},j}}{Q^{(it)}_i}$
    $\Phi^{(it+1)}_{\text{est},j} \leftarrow \Phi^{(it)}_{\text{est},j} \exp\left(\frac{T_j}{S_j}\right)$
  $\text{RMSE}^{(it+1)} \leftarrow \sqrt{\frac{1}{m}\sum_{l=1}^{m}\left(\Phi^{(it+1)}_{\text{est},l} - \Phi^{\text{ref}}_{l}\right)^2}$
  if $\text{RMSE}^{(it+1)} > \text{RMSE}_{\text{prev}}$ **then**
    break
  $\text{RMSE}_{\text{prev}} \leftarrow \text{RMSE}^{(it+1)}$
return $\boldsymbol{\Phi}_{\text{est}} \leftarrow \boldsymbol{\Phi}^{(it+1)}_{\text{est}}$

Since GRAVEL was adopted to solve the ill-posed problem in wide-range neutron spectrometry, it is also applied to this problem. The processing performed in this algorithm was summarized in Algo 1.

(C) MLEM

This concept applied the maximum likelihood estimation, a standard statistical tool for point estimation. For maximizing the likelihood function, we use a general iterative algorithm called Expectation Maximization (EM in further text), originally developed for image reconstruction in astronomy, medicine, etc. Therefore, this algorithm is called "MLEM." The algorithm is based on statistical principles and considers the Poisson nature of measurements, which is applicable in radiation measurements because almost all measurement results adhere to the Poisson distribution. The iterative process is described in the following Equation (2.35).

$$\varphi_j^{est(it+1)} = \frac{\varphi_j^{est(it)}}{\Sigma_{i=1}^{N} R_{ij}} \Sigma_{i=1}^{N} R_{ij} \frac{Y_i}{Q_i^{(it)}} \tag{2.35}$$

This process was written in Algo 2.

ALGORITHM 2: MLEM unfolding algorithm

Input: $\boldsymbol{y} \in \mathbb{R}^{n}_{\geq 0}$, $R \in \mathbb{R}^{n \times m}_{\geq 0}$, $\boldsymbol{\Phi}^{(0)} = \frac{1}{m}$, it
Output: $\boldsymbol{\Phi_{est}}$
for $it = 0, 1, \ldots N_{\text{iter}}$ **do**
  $\boldsymbol{q}^{(it)} \leftarrow R\,\boldsymbol{\Phi}^{(it)}_{\boldsymbol{est}}$ // m
  for $j = 1, \ldots, n$ **do**
    $\phi_j^{(it+1)} \leftarrow \phi_j^{(it)} \cdot \sum_{i=1}^{m} \frac{R_{ij}\, y_i}{q_i^{(it)}}$
  $\mathrm{RMSE}^{(it+1)} \leftarrow \sqrt{\frac{1}{m}\sum_{l=1}^{m}\left(\Phi_{\text{est},l}^{(it+1)} - \Phi_l^{\text{ref}}\right)^2}$
  // If $\mathtt{RMSE}_{it} > \mathtt{RMSE}_{it-1}$, break
  if $\mathrm{RMSE}^{(it+1)} > \mathrm{RMSE}_{\text{it}}$ **then**
    break
  $\mathrm{RMSE}_{\text{it}} \leftarrow \mathrm{RMSE}^{(it+1)}$
return $\boldsymbol{\Phi}_{\text{est}} \leftarrow \boldsymbol{\Phi}^{(it+1)}_{\text{est}}$

Algorithms (A) - (C) have been investigated a lot, and their details and uncertainty propagation are summarized in Ref. [79].

(D) Bayesian Approach

This concept regards the inverse problem as one of probability; Bayes' Theorem is applied to find the solution, proposed by D'Agostini [80]. Firstly, the probability (P) is defined as follows.

- P(E) ≥ 0, where E is an event
- P(Ω)=1, where Ω is a sample space
- P($U^{\infty}_{(i=1)}E_i$) = $\Sigma^{\infty}_{(i=1)}\ P(E_i)$, if the event E is an exclusion

Then, the conditional probability of event A for event B is given by

$$P(A \mid B) = \frac{P(A \cap B)}{P(B)} \tag{2.36}$$

The numerator is replaced using the multiplication theorem in probability in the following Equation (2.37).

$$P(A \cap B) = P(A) \cdot P(B \mid A) \tag{2.37}$$

Using the Equation (2.37), the Equation (2.36) is expressed as

$$P(A \mid B) = \frac{P(B|A) \cdot P(A)}{P(B)} \tag{2.38}$$

If events A and B are divided into multiple groups and they are independent, probabilities are written in the following Equation (2.39) with the number of groups (i and j).

$$P(B_i) = \Sigma_{(it=1)}^{n} P(A_k) \cdot P(B_i \mid A_k) \tag{2.39}$$

By replacing the denominator with Equation (2.37), the general Equation of Bayes' theorem is obtained.

$$P(A_j \mid B_i) = \frac{P(B_i|A_j) \cdot P(A_j)}{\Sigma_{(it=1)}^{n} P(A_k) \cdot P(B_i \mid A_k)} \tag{2.40}$$

The integration of this concept into neutron spectroscopy is summarized below. First of all, the sample place is defined as the event where neutrons irradiate the detector. Then, P(A) refers to the initial neutron energy spectrum as the prior probability; P(B) refers to the probability of a signal distribution, which is normalized in Bayes' theorem; P(A | B) refers to the posterior probability of the neutron energy spectrum when a prior probability is given; and $P(B \mid A)$ refers to likelihood as the response function, the signal distribution for a certain neutron energy. $P(A \mid B)$ corresponds to the unfolded energy spectrum, which is derived from already known parameters, the measured depth distribution (P(B)), the theoretically evaluated response function, $P(B \mid A)$, and any initial guess, P(A).

Strictly, the pulse height spectra and energy spectrum don't satisfy the three axioms of probability, so normalization is required for mathematical use.

$$f_j = \Sigma_{i=1}^{m} r_{ij} \tag{2.41}$$

Then, the normalized response function, r'_{ij}, was described as

$$r'_{ij} = \frac{r_{ij}}{f_j}, \tag{2.42}$$

Where r'_{ij} fulfilled the following Equation (2.43).

$$\Sigma_{i=1}^{m} r'_{ij} = 1 \tag{2.43}$$

In the matrix shape, Equation (2.28) was replaced by,

$$
\begin{aligned}
\boldsymbol{Y} &= \boldsymbol{R'F\Phi} \\
R' &= \begin{pmatrix} r'_{11} & \cdots & r'_{1m} \\ \vdots & \ddots & \vdots \\ r'_{n1} & \cdots & r'_{nm} \end{pmatrix} \\
F &= \begin{pmatrix} f_1 & 0 & \cdots & 0 \\ 0 & f_2 & \cdots & \vdots \\ \vdots & \vdots & \ddots & 0 \\ 0 & \cdots & 0 & f_n \end{pmatrix}
\end{aligned}
\tag{2.44}
$$

In accordance with the normalization of R, Y and $\boldsymbol{\Phi}$ should also be normalized properly. Thus, the ideal goal of these processes is to determine $\boldsymbol{Y}$' and $\boldsymbol{\Phi'}$, as shown in

$$
\begin{aligned}
\boldsymbol{Y'} &= \boldsymbol{R'\Phi'} \\
\Sigma_{i=1}^{n} y_i &= \Sigma_{j=1}^{m} \varphi_j = 1
\end{aligned}
\tag{2.45}
$$

For Φ', the normalization was performed using the magnitude of X, $\mid \Phi_F \mid$:

$$
X' = \frac{\mathbf{1}}{\boldsymbol{\Phi_F}} \cdot \boldsymbol{F} \cdot \boldsymbol{X} = \frac{1}{\mid \Phi_F \mid} \cdot \begin{pmatrix} f_1 \cdot \varphi_1 \\ \vdots \\ f_j \cdot \varphi_j \\ \vdots \\ f_n \cdot \varphi_n \end{pmatrix} = \begin{pmatrix} \varphi'_1 \\ \vdots \\ \varphi'_j \\ \vdots \\ x'_n \end{pmatrix} \tag{2.46}
$$

From Equation (2.46), the following Equation is valid:

$$
X = \mid \Phi_F \mid \cdot F^{-1} \cdot X' \tag{2.47}
$$

Therefore, Equation (2.44) is rewritten in

$$
\boldsymbol{Y} = \mid \boldsymbol{\Phi_F} \mid \cdot \boldsymbol{R'} \cdot \boldsymbol{X'} \tag{2.48}
$$

Let it break down the matrix into these elements and calculate the sum of Y.

$$
\begin{aligned}
\mid y \mid &= \Sigma_{i=1}^{m} y_i \\
&= \Sigma_{i=1}^{m} \mid \Phi_F \mid \cdot \Sigma_{i=1}^{n} r'_{ij} \varphi'_j \\
&= \mid \Phi_F \mid \Sigma_{i=1}^{m} \Sigma_{i=1}^{n} r'_{ij} \cdot \varphi'_j \\
&= \mid \Phi_F \mid \Sigma_{i=1}^{m} r'_{ij} \Sigma_{i=1}^{n} \varphi'_j \\
&= \mid \Phi_F \mid
\end{aligned}
\tag{2.49}
$$

In the end, normalization was achieved as in Equation (2.45). It is important to mention that the establishment of Equation (2.49) ensures the validity of the iterative algorithm to be presented. Since epi-thermal neutrons have a lot of groups, this concept is valid for the unfolding. In principle, Bayes' Theorem can estimate the energy spectra with any initial values, corresponding to P(A). This concept was produced by Iwasaki et al., which was applied it to reconstruct CT images [76]. According to his work, other advantages of our approach were listed as follows:

(1) Quite a simple method, easy to calculate without numerical ill-conditioning

(2) Event-based method, which could realize the real-time imaging

(3) Necessary quantities, the likelihood values which can be estimated before the data taking by the simulation calculation

Thanks to these advantages, the Bayesian approach becomes one of the effective approaches for ill-posed problems in the field of radiation measurements [81, 82].

From a theoretical standpoint, the energy spectrum can be obtained in the following Equation.

$$\varphi_j^{est(it+1)} = \Sigma_i \frac{r'_{ij} \cdot \varphi_j^{est(it)}}{\Sigma_j \varphi_j^{est(it)} \cdot r'_{ij}} \tag{2.50}$$

However, in general, matrix elements of the response function in the lower-left become zero; thus, this equation cannot find any solutions. Therefore, Nauchi updated this algorithm as shown in the following Equation [83]:

$$\varphi_j^{est(it+1)} = \Sigma_i y_i \frac{r'_{ij} \cdot \varphi_j^{est(it)}}{\Sigma_j \varphi_j^{est(it)} \cdot r'_{ij}} \tag{2.51}$$

where $\varphi_j^{(est)}$ refers to the jth value of the estimated energy spectrum at it iterations, y_i refers to the i th value of depth distribution, and $r'_{i,j}$ refers to the normalized response function of the detector. Notably, this study introduced a white spectrum, wherein all values of the initial guess were 1/n of the initial energy spectrum ($\boldsymbol{\Phi}_{\boldsymbol{est}}^{\boldsymbol{(1)}} = 1$). Note that there have been several algorithms from Bayesian Estimation, such as MCMC, PyUnfold, etc [56, 84], which were compared to **Appendix B**.

An important differenct thing from MLEM algorithm is that this process obtained the real energy spectrum by multiplying reciprocal number of normalization factor, derived from when the normalized $\boldsymbol{R}^{'}$, described in

$$\boldsymbol{\Phi}_{\boldsymbol{true}} = \boldsymbol{R}_{\boldsymbol{j}}^{-\mathbf{1}} \cdot \boldsymbol{\Phi}_{\boldsymbol{est}} \tag{2.52}$$

Where R_j achieved $R_{i,j} = R'_{i,j} \cdot R_j$. This method has not been supported theoretically, but used as expanded interpretation. In fact, its convergence was proved without any statistical errors [83]; however, it was not in the case with error. The whole process of "Nauchi-Bayes" was shown in Algo 3.

This study adopted "Nauchi-Bayes" as the unfolding data processing, which was compared to other algorithms, GRAVEL, MLEM, and PyUnfold module for the unfolding process in the PSPC (See **Appendix B**).

ALGORITHM 3: Bayesian unfolding algorithm (proposed by [83]).

Input: $\boldsymbol{y} \in \mathbb{R}^{n}_{\geq 0}$, $R \in \mathbb{R}^{n \times m}_{\geq 0}$, $\boldsymbol{\Phi}^{(0)}_{\mathrm{est}}$, $\boldsymbol{\Phi}^{\mathrm{ref}}$, it
Output: $\boldsymbol{\Phi}_{\mathrm{est}}$
// Compute $f_j = \sum_{i=1}^{n} R_{ij}$ and normalized response $R'_{ij} = R_{ij}/f_j$
for $j = 1, \ldots, m$ **do**
  $f_j \leftarrow \sum_{i=1}^{n} R_{ij}$
  for $i = 1, \ldots, n$ **do**
    $R'_{ij} \leftarrow \dfrac{R_{ij}}{f_j}$
// Main loop, acquisition of $\boldsymbol{\Phi}^{(it+1)}_{\mathrm{est}}$
$\mathrm{RMSE}^{1} \leftarrow \infty$ // RMSE at iteration 1
for $it = 0, 1, \ldots, N_{\mathrm{iter}} - 1$ **do**
  $\boldsymbol{q}^{(it)} \leftarrow R' \, \boldsymbol{\Phi}^{(it)}_{\mathrm{est}}$ // n-dim predicted counts
  for $j = 1, \ldots, m$ **do**
    $\Phi^{(it+1)}_{\mathrm{est},j} \leftarrow \Phi^{(it)}_{\mathrm{est},j} \cdot \sum_{i=1}^{n} y_i \dfrac{R'_{ij}}{q^{(it)}_i}$
  $\mathrm{RMSE}^{(it+1)} \leftarrow \sqrt{\dfrac{1}{m} \sum_{l=1}^{m} \left(\Phi^{(it+1)}_{\mathrm{est},l} - \Phi^{\mathrm{ref}}_{l} \right)^2}$
  // If $\mathrm{RMSE}_{it} > \mathrm{RMSE}_{it-1}$, break
  if $\mathrm{RMSE}^{(it+1)} > \mathrm{RMSE}_{\mathrm{it}}$ **then**
    break
  $\mathrm{RMSE}^{\mathrm{it}} \leftarrow \mathrm{RMSE}^{(it+1)}$
return $\boldsymbol{\Phi}_{\mathrm{est}} \leftarrow \boldsymbol{\Phi}^{(it+1)}_{\mathrm{est}}$

2.3.3 Stopping Criteria

The spectrum unfolding method predominantly involves setting an initial spectrum and iteratively applying specific algorithms such as GRAVEL, MLEM, and our approach. The number of iterations is a critical factor in these approaches. Figure 2.6 illustrates a reference spectrum and estimated spectra using our approach [83] with several iteration times. With fewer iterations, the estimation results tend to depend on the initial spectra, while the influence of noise becomes increasingly significant with more iterations. This section introduces previous approaches to determining this parameter [85, 86, 87], and the way in this study. Ideally, the number of iterations can be determined by minimizing the rootmean-square-error (RMSE) between the unfolded estimate and the ground-truth spectrum, as shown in the following Equation (2.53)

$$RMSE = \sqrt{\frac{\sum_{j=0}^{J}(\overline{\varphi_j} - est_j^{(it)})^2}{J}} \tag{2.53}$$

We named this approach as "ideal iteration number." Bouallgue et al developed MLEM-STOP method for this problem, which used an indicator function denoted as $\mathbf{J}^{(it)}$ [85]. it is constructed by computing the mean squared error of the measured input spectrum φ_j and forward-projected estimate spectrum $q_i^{(it)}$ normalized to the forward-projected mean as follows:

$$q_i^{(it)} = \sum_{j=0}^{J} R_{ij}\varphi_j^{(it)} \tag{2.54}$$

$$G_i^{(it)} = \frac{\sum_{i=0}^{I}(R_{ij} \cdot \varphi_j^{est(it)} - q_i^{(it)})^2}{\sum_{i=0}^{I} q_i^{(it)}} \tag{2.55}$$

As the number of iterations are increased, the unfolded spectrum may arrive at a noise-free condition when the expectation value of the mean-squared deviation between φ_j and $Q_i^{(it)}$ equals the mean $Q_i^{(it)}$. At this point, $G^{(it)} = 1$ and the stopping criteria has been met. In practice, it has been found the algorithm should be terminated just before $G^{(it)} = 1$.

Tamaki applied a Monte Carlo method to determine the stopping number [87]. In this process, a certain amount of sample array ($\boldsymbol{q}$) is generated based on the measurement data, as follows in a normal distribution, N (μ, ϵ), where μ is the average of the measurement data, and ϵ is its variance. Q (u) is composed of a random number, where u represents the number of distributions, which is 1000 in this study. The estimated energy spectrum using Equation (2.51) in *it* times ($\varphi_j^{(it)(u)}$) is then obtained, and their average and variance $\overline{\varphi\ (\mathrm{est})^{(it)}}_j$, $\epsilon^{(it)}_{\mathbf{\Phi}\ (\mathrm{est}),j}$ are also calculated as follows:

$$\overline{\varphi\ (\mathrm{est})^{(it)}}_j = \frac{1}{u}\sum_u \varphi\ (\mathrm{est})_j^{(it)(u)} \tag{2.56}$$

$$(\epsilon^{(it)}_{\mathbf{\Phi}\ (\mathrm{est}),j})^2 = \frac{1}{u}\sum_u (\varphi\ (\mathrm{est})_j^{(it)(u)} - \overline{\varphi\ (\mathrm{est})^{(it)}}_j) \tag{2.57}$$

In principle, the measured data for and its variance are described in the following Equations,

$$\overline{q_i^{(it)}} = \sum_j r_{i,j} \cdot \overline{\varphi^{(it)}}_j \tag{2.58}$$

$$\epsilon^{(it)}_{\mathbf{q},i} = \sum_j (r_{i,j})^2 \cdot (\sigma^{(it)}_{\mathbf{\Phi}\ (\mathrm{est}),j})^2 \tag{2.59}$$

According to Kondo [88], this ϵ is monotonically increasing; therefore, this study applied the maximum *it* value fulfilled with the following situation.

$$\sum_i \epsilon_i^2 \geq_i (\epsilon^{(it)}_{\boldsymbol{Y},i})^2 \tag{2.60}$$

This Equation implies that the iteration is performed until the variance of the measured data corresponding to the estimated spectrum remains below the true variance observed in the experiment.

This study applied "ideal iteration nember" approach to determine the iteration number. Based on response function $\boldsymbol{R}$ and reference spectra ($\boldsymbol{\Phi_{ref}}$), a true measured data ($\boldsymbol{Y}$, derived from $\boldsymbol{R \cdot \Phi_{ref}}$) was obtained. $\boldsymbol{\epsilon}$ (5%), based on a normal distribution was added to $\boldsymbol{Y}$, $\boldsymbol{R \cdot \Phi_{ref} + \epsilon(5\%)}$, and defined this number by calculating RMSE values for each iteration. Results of iteration number determination and the comparison of "Nauchi-Bayes" method to other conventional unfolding approach in **Appendix B**.

In order to compare the estimation quality, a log-mean normalized RMSE was introduced as follows:

$$\overline{\Phi_{\log}} = \exp\left\{\frac{1}{N}\sum_{j=1}^{N} \ln \varphi_j^{\mathrm{ref}}\right\}, \tag{2.61}$$

$$\mathrm{nRMSE} = 100 \times \frac{\sqrt{\frac{1}{N}\sum_{j=1}^{N}\left(\varphi_j^{\mathrm{est}} - \varphi_j^{\mathrm{ref}}\right)^2}}{\overline{\Phi_{\log}}}. \tag{2.62}$$

Here, $\overline{\Phi_{\log}}$ denotes the log-mean value of the reference spectrum. The log-mean was employed because the neutron spectrum spans a wide dynamic range of approximately five orders of magnitude. The unit of nRMSE is percent (%). Therefore, this parameter evaluates the average deviation of the estimation results compared to the reference.

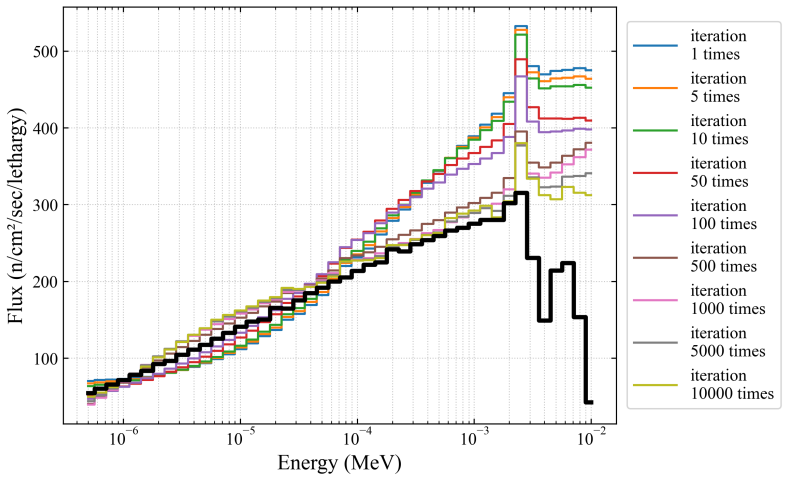


Figure 2.6: Neutron energy spectra estimated by Equation (2.51) in *it*.

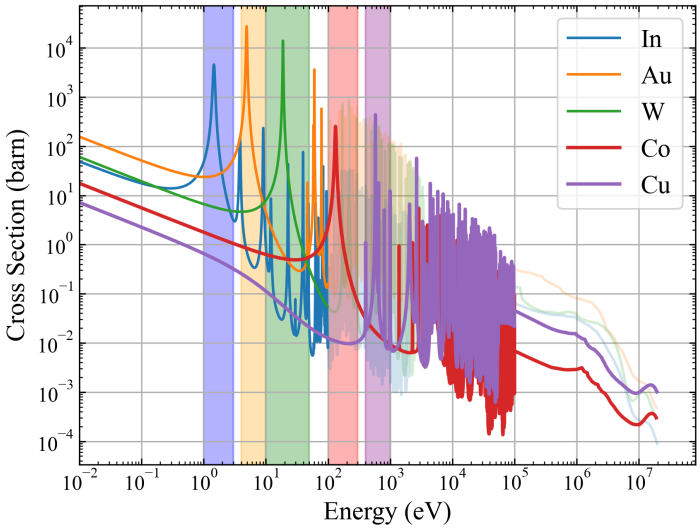


Figure 2.7: Examples of materials used for the multiple activation method. Each material has a large cross-section at a typical energy region in epi-thermal neutrons.

2.4 Conventional Approaches for Epi-thermal Neutron Spectrometry

Several detectors and unfolding algorithms were used, as discussed in **Sections 2.2, 2.3**. Methods such as the multiple activation foil method and the Bonner Sphere Spectrometer (BSS) have been developed to evaluate the neutron energy spectrum in the epi-thermal range [42, 43, 45, 47]. This section outlines these conventional approaches and discusses their limitations.

Based on the principle in **Section 2.2.2**, activation foils can detect the aver-

age neutron flux. The multiple activation foil method utilizes the differences in the activation (or inelastic) cross-section for materials to evaluate the wide range of the neutron's energy spectrum. Multiple foils have been used to cover the whole energy range of the spectrum, as shown in Figure 2.7. Auterinen et al performed measurements of the neutron spectrum across eight reactor-based BNCT facilities with 12 foil detectors [42]. In addition, Liu et al expanded the number of detectors by considering complexities in the self-shielding effect, which is resulting in the evaluation of the spectrum with 25 groups [43]. However, the magnitude of activation cross-section in materials is extremely varied, so that the correction of the detector's dimension is necessary. This caused the uncertainty in the estimated spectra. Besides, the previous studies have revealed that the number of materials is insufficient to convey the energy spectrum in epi-thermal neutrons. This limitation implies a low-energy resolution, and a prior distribution including a priori information is necessary to obtain an accurate spectrum in the unfolding process.

The BSS consists of multiple Bonner sphere detectors with different energy response functions. Each detector contains a neutron moderator to slow incident neutrons, with a low-energy neutron detector at its center, as Figure 2.8 depicts. The BSS accounts for diverse energy response functions by using several Bonner sphere detectors, as shown in Figure 2.9. This collection of response functions, referred to as the "response function matrix," is evaluated by Monte Carlo simulations and measurements in a reference neutron field. Sequential measurements of each BSS enable the unique yield count to each detector for the neutron beam, given in the convolution of neutron spectral fluence and the detector's energy response function as discussed in **Section 2.3.1**. However, BSS also has an issue with energy resolution due to the number of detectors. Ueda et al performed this methodology for epi-thermal neutron spectrometry with only three moderators [47]. Nowadays, measurements are carried out in only about ten Bonner sphere detectors to assess the broad neutron energy distribution, according to ref. [89]. The resulting energy distribution is then divided into dozens of energy bins in a process known as few-channel unfolding; thus, high energy resolution is not expected. Moreover, many time measurements are required, which causes several uncertainties in the experimental conditions.

In summary, the Utilization of BSS is challenging to determine the actual neutron spectral fluence without any prior information, as is the case with the multiple activation foil method. The unfolding method proposes to modify the initial spectrum to make it more consistent with that measured by the Bonner sphere.

In our research laboratory, another unique spectrometer using ^{3}He counter has been developed [46, 87, 90, 91]. This system employs a liquid-based moderator, whose thickness can be easily adjusted, thereby varying its neutron moderation capability. Similar to the Bonner sphere spectrometer (BSS), which uses moderators of different thicknesses, this method achieves sensitivity over a wide dynamic energy range by changing the volume of the liquid moderator surrounding the ^{3}He counter. A prototype of this spectrometer was designed and developed in our laboratory [46, 87], followed by an experimental campaign. Figure 2.10 shows the results of

the validation experiment, demonstrating that the unfolded spectrum successfully reproduced the reference spectrum. These results confirm the feasibility of this approach. For applications to epi-thermal neutron spectrometry, it is known that the angular distribution of incident neutrons can be a major source of discrepancy. To address this issue, an upgraded detector system is currently under development [91].

As described above, neutron spectrometry over a wide energy range has long been challenging, and experimental approaches have only recently begun to emerge. Therefore, the development of novel systems that can further improve estimation accuracy is strongly required.

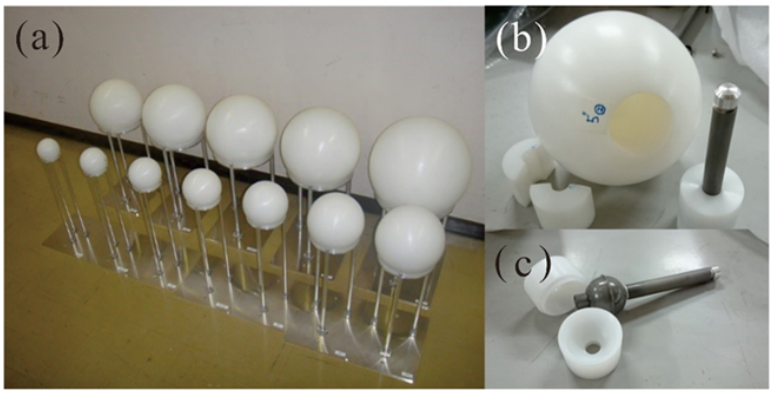


Figure 2.8: (a) A group of BSS, (b) A detailed structure, and (c) Spherical ^{3}He counter, commonly used as a low-energy neutron detector in BSS [89].

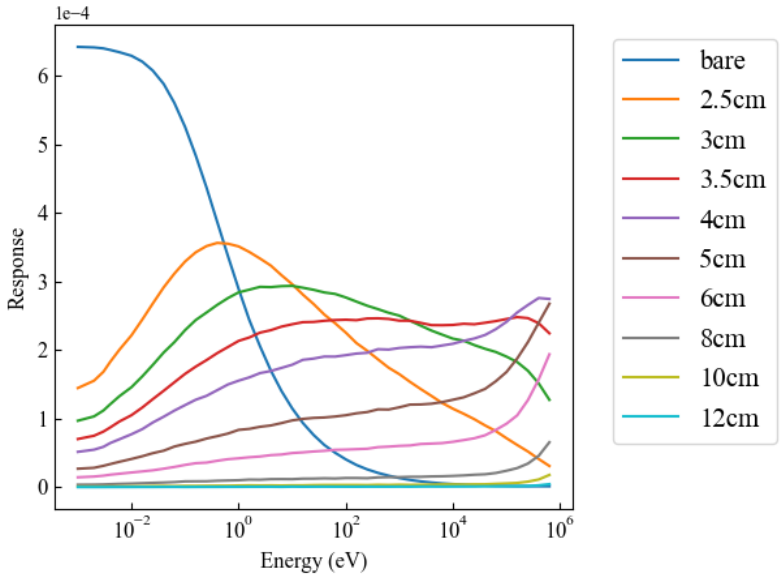
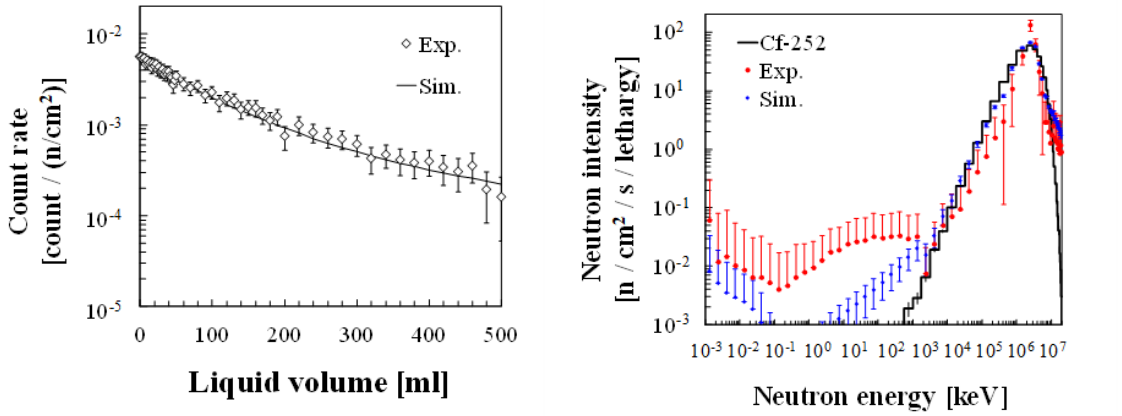


Figure 2.9: Responses of Bonner Sphere calculated in PHITS.



(a) Experimental Result

(b) Unfolded result

Figure 2.10: Experimental results of the (a)count rates (b) unfolding result using ^{252}Cf neutron source. Data was extracted from Ref [90].

2.5 Application of ^{3}He Position Sensitive Proportional Counter

The ^{3}He PSPC possesses signal units at both ends, and particles that reach the resistance wire are divided into two signals. The position of reaction detection (called "detection position" henceforth) was determined from the ratio of the signals generated by both signal units [92]. ^{3}He was introduced as an inside gas, and protons generated by the ^{3}He (n, p) ^{3}H reaction were detected. Due to the unique cross-section of its nuclear reaction, extensive high and 1:1 correspondence to the neutron energy based on 1/v law (see Figure 2.11), by irradiating neutrons parallel to the axis of the PSPC on its entrance, low-energy neutrons were detected at shallow positions while high-energy neutrons were detected at deep positions. This signal distribution along the axis direction, called depth distribution $\boldsymbol{Y}$, was reconstructed as the neutron energy spectrum [49], as described

$$\mathbf{Y} = \boldsymbol{R}\boldsymbol{\Phi} \tag{2.63}$$

Where $\mathbf{R}$ is the response function of PSPC. The principle of PSPC-based epi-thermal neutron spectrometer was shown in Figure 2.12. this study utilized a ^{3}He PSPC with a 40 cm length and 2.5 cm diameter, and the pressure of the ^{3}He gas was 5 atm. Given the high cross-section of ^{3}He and its linearity, the length of the PSPC reflects the possible energy range to measure. In addition, the wall effect can be reduced as the diameter of PSPC increases. The spatial resolution of the PSPC has been reported to be excellent, e.g., several millimeters of resolution can be achieved using pulse shape analysis [50, 93]. Thus, this study divided the PSPC into 1 cm and scored the signals in each location to make the depth distribution (see Figure 2.13). The energy resolution was evaluated in the previous study [49]; however, epi-thermal neutrons in the real BNCT field should be discrete, so spatial resolution was more important than the energy resolution in this study.

The response function (R) of the detector was considered to correspond to the response rate of the ^{3}He (n, p) ^{3}H reaction when neutrons reached h cm in the ^{3}He PSPC, which is theoretically described as follows:

$$R(x, E)\,dx = \Sigma(E) \cdot \exp(-\Sigma(E)x)\,dx \tag{2.64}$$

where $\Sigma(E)$ refers to the macroscopic nuclear reaction cross-section, which is defined as the product of the microscopic nuclear reaction cross-section ($\sigma(E)$) and atomic number density (N), as expressed in Equation (2.65):

$$\Sigma(E) = N \cdot \sigma(E). \tag{2.65}$$

The nuclear reaction cross-section data were extracted from JENDL-5.0 [64]. Thus, the response function of the detector was evaluated using Equation (2.64), as shown in Figure 2.14.

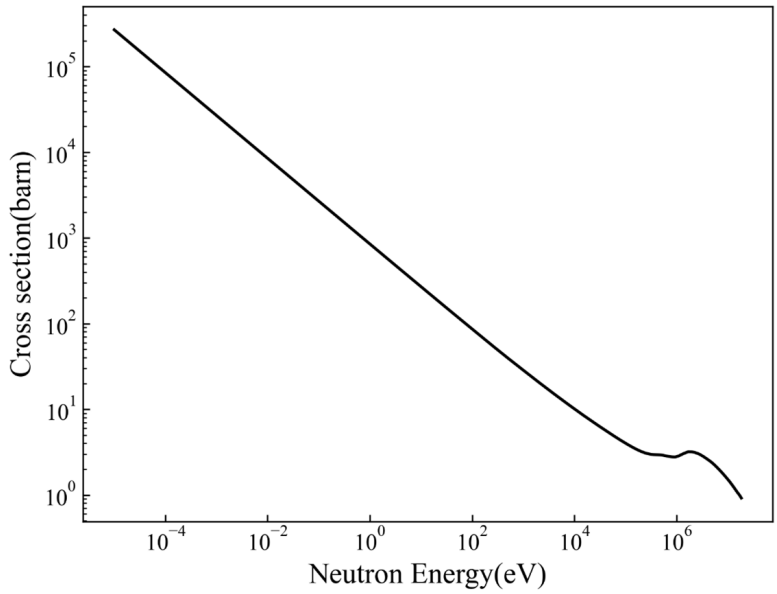


Figure 2.11: ^{3}He Cross-section [64].

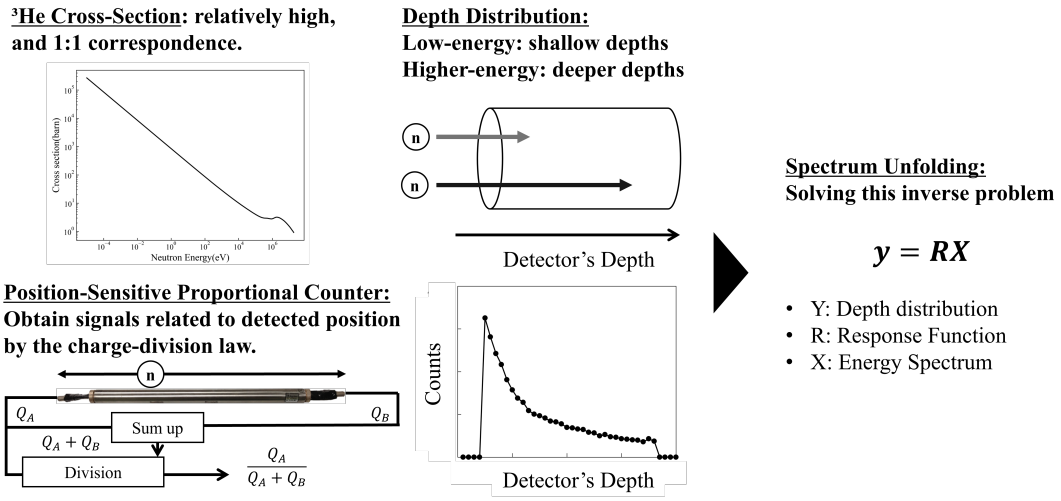


Figure 2.12: Measurement principle of ^{3}He PSPC spectrometer.

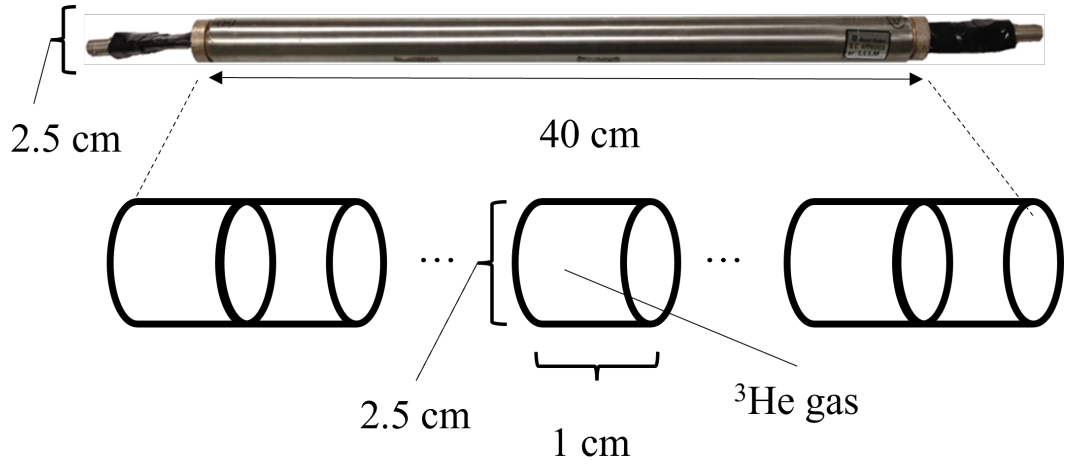


Figure 2.13: PSPC, and illustration of its separation to evaluate the depth distribution in simualtion work. In order to cosider the depth distribution, we separated PSPC in 1 cm intevals [49, 52]. In MCNP, depth distribution was calculated by ^{3}He (n, p) ^{3}H response rate in each group, and then compared to the experimental result as shown in Figure 1.7.

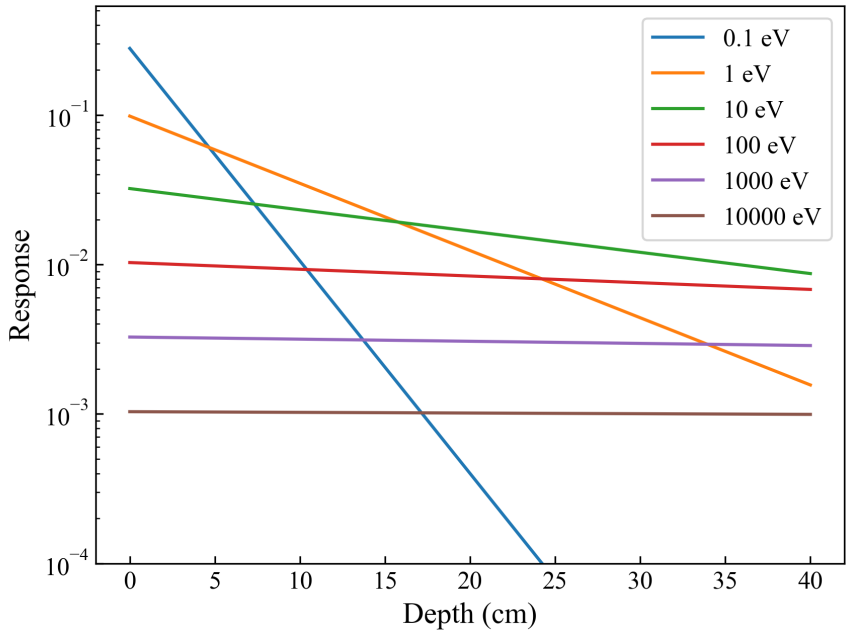


Figure 2.14: Theoretical response function in PSPC

2.6 Monte Carlo Simulation

Monte Carlo simulations were employed to theoretically derive physical evaluation properties by accurately modeling the behavior of radiation. This study applied the Monte Carlo N-particle code 5 (MCNP 5) and the Particle and Heavy Ion Transport code System (PHITS) for this objective [94, 95]. In this section, the proposed Monte Carlo simulation is compared with a deterministic method in order to clarify its advantages and limitations.

Monte Carlo methods are very different from deterministic methods. Deterministic methods solve the transport Equation for the average particle behavior, for example, the discrete ordinates method. On the other hand, Monte Carlo methods obtain answers by simulating individual particles and recording some aspects in tallies. The average behavior of particles in the physical system is then inferred from the average behavior of the simulated particles by the central limit theorem. Both methods are completely different in the way to solve a problem, even in the construction of the solution. While deterministic methods typically give complete information throughout the phase space of the problem, the Monte Carlo methods supply information only about specific tallies requested by the user.

Monte Carlo methods are suitable for solving complicated three-dimensional, time-dependent problems. Because the Monte Carlo method does not use phase space boxes, there are no averaging approximations required in space, energy, and time. This is especially important in allowing detailed representation of all aspects of physical data [94].

This study mainly employed the MCNP 5 to model the physical behaviors in the detectors (PSPC and activation foils) and to design the experimental system. MCNP is a general-purpose, continuous-energy, generalized-geometry, time-dependent, coupled neutron/photon/electron Monte Carlo transport code. It can be used in several transportation modes, source definitions, and tally settings to obtain physical solutions in many situations. This study generally evaluated the neutron absorption of ^{3}He inside the PSPC, so the "F4" tally in MCNP was used for this objective. Notably, the behavior in the activation foils can also be assessed in this tally. This tally calculates the response rate of the ^{3}He (n, p) ^{3}H reaction or activation reactions, for instance, the ^{197}Au (n, γ) ^{198}Au reaction, by scoring the track lengths at tallies and multiplying by values of the cross sections in the target reactions. These values are derived from the evaluated nuclear data libraries as discussed below. The effectiveness to represent the PSPC behavior in F4 tally of MCNP was examined in the previous study.

PHITS is also one of the most familiar Monte Carlo simulation codes, which enables simulations of charged particles like Protons and Carbon ions, whereas MCNP 5 doesn't support these kinds of simulations (MCNP 6.3 allows us to simulate in multi-type of charged particles). Recently, the varsatilities of PHITS have been expanded, such as Microdosimetry simulations, setting multi-source, such as neutron & γ mixed field or radioactivity, as the source in a simulation [95]. These functions were applied to the modeling of the IP's response, and the simulation results were compared to the experimental results for the benchmarking, understanding the physics during the IP's detection process (See **Chapter 6**).

The Monte Carlo simulation uses continuous-energy nuclear and atomic data libraries. The primary sources of nuclear data are evaluations from the Evaluated Nuclear Data File (ENDF) system [96], Japanese evaluated nuclear data library (JENDL) [64], and Fusion Evaluated Nuclear Data Library (FENDL) [97], etc. Considering the compatibility of the MCNP 5, the previous model of the latest MCNP code (MCNP 6.3), the JENDL-4.0 and 5.0 were used as the nuclear data in this study [64, 98]. These data libraries contain several lists of nuclear interactions, neutron interactions, neutron-induced photons, photon interactions, neutron dosimetry or activation, and thermal particle scattering S (α, β).

Using evaluated nuclear data libraries, particle transport can be modeled in radiation-transport simulations. However, recent advances in experimental techniques and computational environments have required calculations under increasingly complex conditions, for which existing physics models alone are often insufficient. To address this limitation, modern Monte Carlo transport codes now provide user-defined physics capabilities, or they originally include highly flexible physics modules, as in GEANT4 [99] and OpenMC [100].

Simulation geometries and the tally used in this study are introduced in each Chapter, and a part of the input file in the simulation is presented in **Appendix D**.

2.7 Summary

This section explores neutron detectors and the unfolding process to obtain the neutron energy spectrum. **Section 2.2** introduced a series of neutron detectors and their measurement principles. In this Section, an outline of the principle of IP-ND was also presented.

Then, **Section 2.3** outlines the unfolding process, the way to transfer the signal distribution into the neutron energy spectrum. This study proposed a novel approach for unfolding based on Bayes' theorem. Since there are strengths and weaknesses in unfolding approaches in the neutron's energy ranges, I compared several unfolding algorithms that are suitable for point estimation.

Section 2.4 showed two conventional measurement systems, the multiple activation foil method and the Bonner Sphere Spectrometer (BSS), and pointed out their limitations for neutron spectroscopy in epi-thermal energy ranges.

To cope with this issue, this study suggested the feasibility of the ^{3}He PSPC, and **Section 2.5** summarized the measurement principle. Also, this section demonstrated the feasibility of our proposed method using PSPC for the evaluation of the energy spectrum up to 1 keV.

Prior to the concrete approaches to improving measurement accuracy, this study used the Monte Carlo simulation; thus, **Section 2.6** described it and the computational simulation codes.

In the following Chapters, methods to improve the estimation quality in PSPC, and another novel spectrometer using IP-ND has been investigated.

3 Application of a Pencil Beam Neutron Source

3.1 Introduction

This chapter focuses on the application of a beam-type neutron source to enhance the estimation performance of PSPC. As discussed in **Chapter 2**, the primary independence of the response function is crucial for the unfolding process. ^{3}He PSPC has attempted to exhibit this characteristic in its depth distribution using a 1:1 correspondence to the epi-thermal neutrons in the ^{3}He cross section. However, this concept was assumed that the neutron incidents enter from the top surface of the detector. If neutrons enter from the side surface of the detector, thisrelationship is corrupted, resulting in the low estimation accuracy for the energy spectrum. In fact, we performed in MCNP 5 to investigate this phenomenon. Events of neutrons entering the ^{3}He PSPC were divided into three components, as shown in figure 3.1. Theoretically, only component-A neutrons could enter the ^{3}He PSPC. Figure 3.2 presents the contributions of each component calculated in MCNP 5, that calculated in the following Equation,

$$R_A = \frac{N_A}{N_A + N_B + N_C} \tag{3.1}$$

Where R_A is the ratio of ^{3}He (n, p)^{3}H reaction rate by "component A" neutrons, N_A, N_B, and N_C are the total count in PSPC for each component. This result revealed that the contribution of component A was below 90 % at each detector depth. Moreover, neutron distribution at the detector exhibited substantial uncertainty owing to the scattering effects arising from the proximity of the epi-thermal column and geometric shape of the detector's signal terminals. Therefore, it requires a beam-type neutron source, and this chapter outlines the design and the effectiveness of this approach.

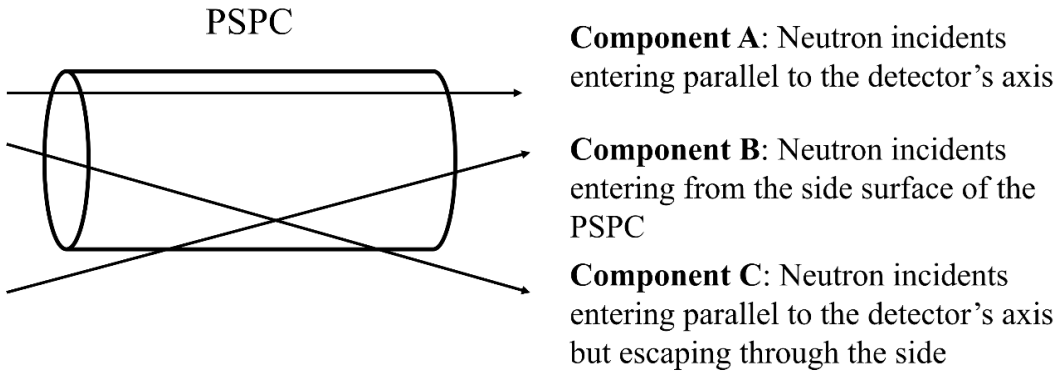


Figure 3.1: Three components of neutron incidents to PSPC. Component A is the proper signals for the Depth distribution which represents the correspondency between the incident energy and the detector's depth.

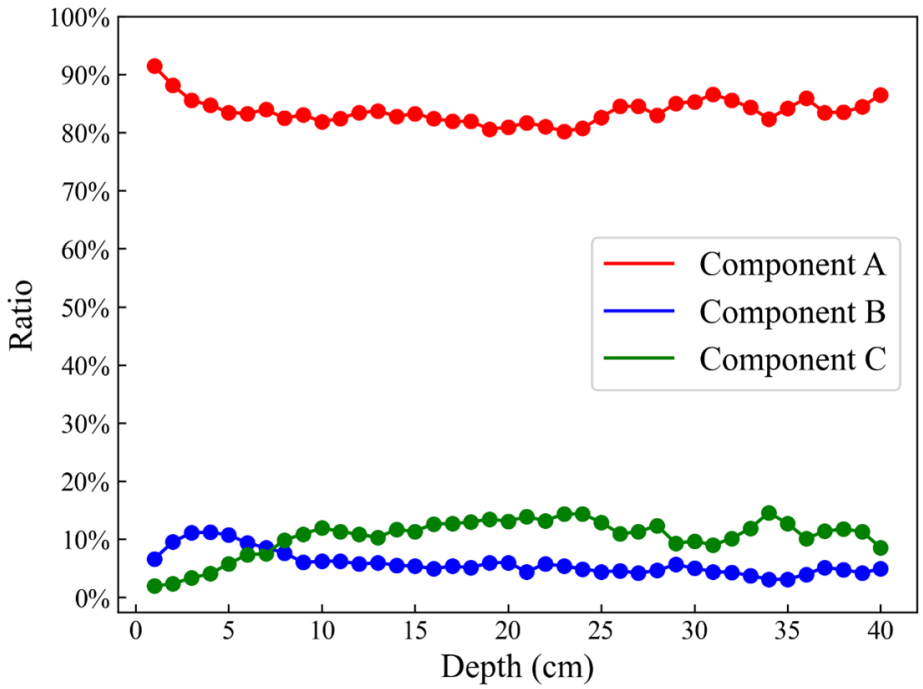


Figure 3.2: Ratio of each component calculated in MCNP 5. The error at each depth is sufficiently small to be considered negligible [52].

We first presented the introduction of the epi-thermal column designed for the validation of our spectrometer in **Section 3.2**, and then discussed the developmwnts of the beam-neutron source from **Section 3.3**. This chaoter includes the numerical analysis conducted to evaluate the estimation accuracy in this approach. Finally, the implications obtained in **Section 3.3.5** and potential future developments are elaborated in **Section 3.4**.

This study assumed the world's most intense 14 MeV neutron source acility of Osaka University, OKTAVIAN [101], as the neutron generator (see Figure 3.3). It is one of the Cockcroft – Walton type electrostatic accelerators, and D-T neutrons are generated in the following Equation (3.2).

$$D + T \rightarrow He + n + 14.1MeV \tag{3.2}$$

According to Tamaki et al, the maximum intensity of the continuous neutron source was approximately 3×10^{12} DT neutrons per second [102]. The neutron source is equipped with two beam ports: one leads to a large experimental hall for large-scale experiments, and the other connects to a separate room dedicated to high-intensity neutron irradiation, referred to as the heavy irradiation room. In this Chapter, assuming the large experimental hall, the beam-neutron source was designed.



Figure 3.3: Overviews of OKTAVIAN

3.2 Epi-thermal Neutron Source Based on OKTAVIAN

This section describes the structure of the beam-type neutron source designed in OKTAVIAN. The core concept involves the installation of a collimator to shape the neutron beam, based on the epi-thermal neutron source developed by Osawa et al. [53], as discussed in **Section 3.2.1**. The methodology and results related to the collimator design are presented in **Section 3.3**.

3.2.1 Epi-thermal neutron source

Epi-thermal neutron field for fundamental research regarding low-energy neutron application, including this study, was developed. It was designed to obtain sufficient neutron intensity in the epi-thermal range, as well as high-rated epi-thermal neutrons compared to high-energy neutrons (above 10 keV). The detailed structure of the epi-thermal column is shown in Figure 3.4.

It is composed of carbon, lead, iron, carbon-fluoride, aluminium-fluoride, and titanium. Carbon and lead were used as reflectors. Since neutrons generated in DT reactions are isotropic, reflectors play a role in enhancing the neutron yield for the destination of the detector. Iron has a high absolute cross-section for 14 MeV neutrons, and it is employed to reduce high-energy neutrons. Indeed, some of the neutrons emitted in DT reactions are directly irradiated into the epi-thermal column. Aluminium-Fluoride and Carbon-Fluoride were installed as moderators for neutrons passed through iron. Ideally, the most appropriate material is Aluminium-Fluoride; however, due to the technical issue, it is challenging to fabricate the moderator in this dimension ($50 \times 50 \times 40$ cm) only with this material.

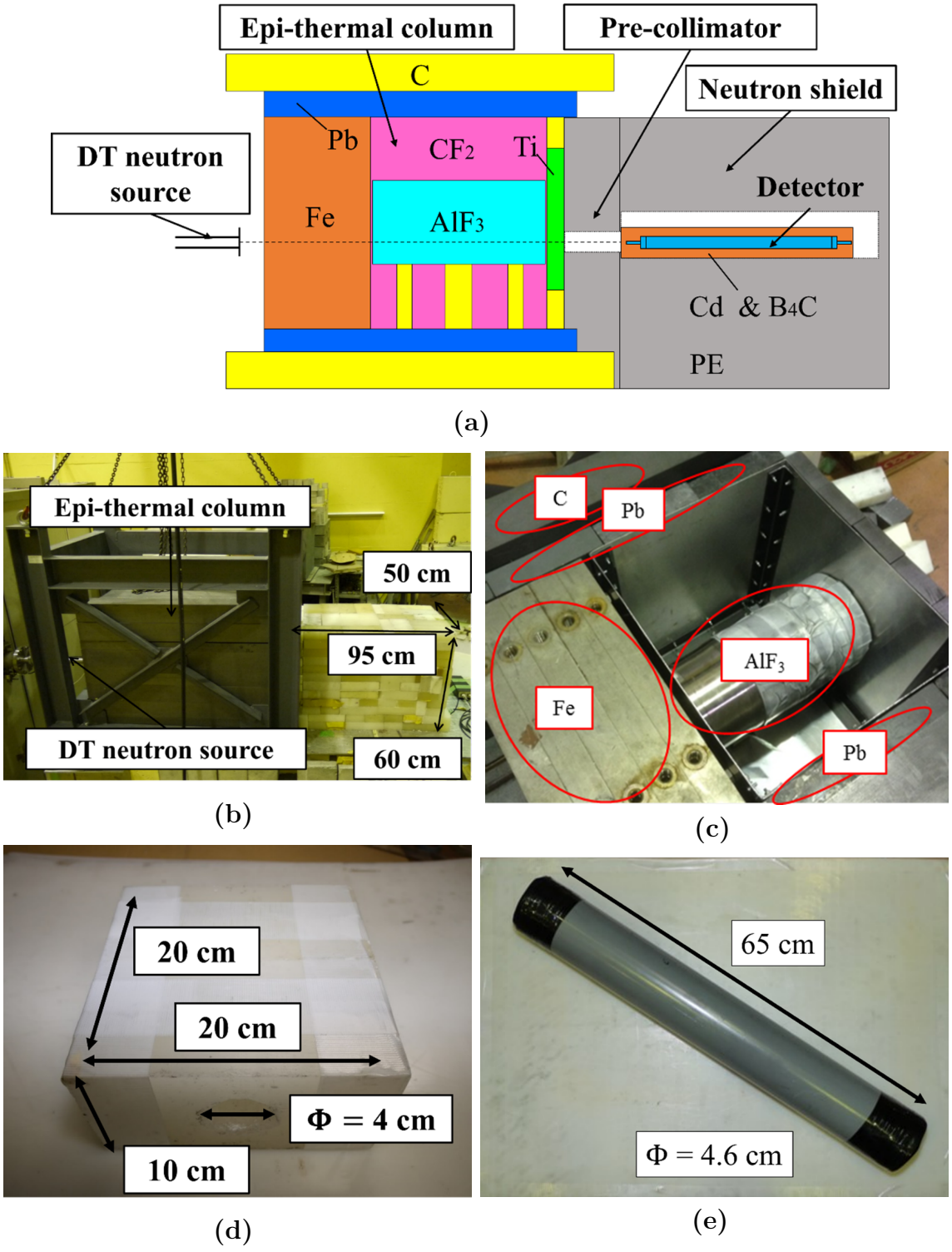


Figure 3.4: System overview in the validation experiment. a: Schematic Overview, b: Fabricated experimental system. A crane was used to adjust the position of the system to the DT neutron source, c: Inside design of the epi-thermal column, d: Pre-collimator design, and e: Detector and absorber.

Therefore, a part of the moderator is substituted with Carbon-Fluoride. It is important to mention that a container was installed for powdered Carbon-Fluoride, and this structure was incorporated in MC simulations. Titanium was adopted to reduce neutrons in the hundred keV range because it has a high resonance cross-section in this energy range.

More details were presented in ref [53], the energy spectrum was shown in Figure 3.5. As illustrated, the neutron field was predominantly composed of epi-thermal neutrons (orange region). The statistical ratio of epi-thermal to fast neutrons ($\frac{\Phi_{epi}}{\Phi_{fast}}$), defined as the η value in the referenced study, was calculated to be 21.2. The total flux of this soutce across the epi-thermal range (Φ_{epi}) was also 3.9×10^3 ($\mathrm{n\,cm^{-2}\,s^{-1}}$), all of which achieved the design goals.

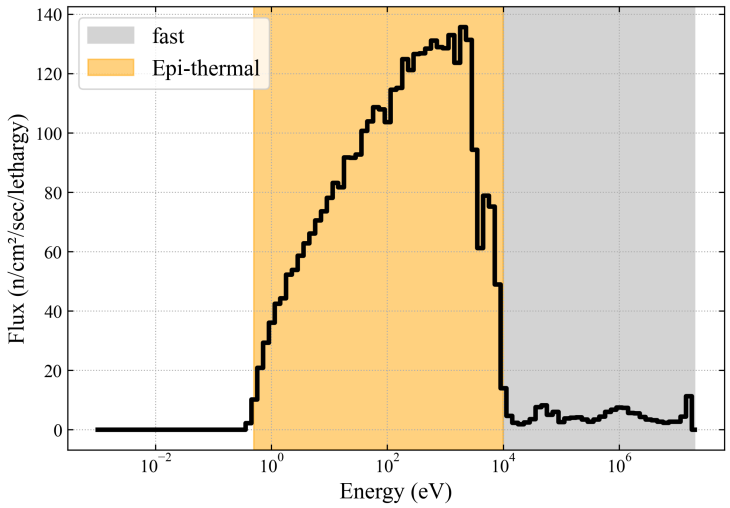


Figure 3.5: Energy spectrum of the designed epi-thermal column [53].

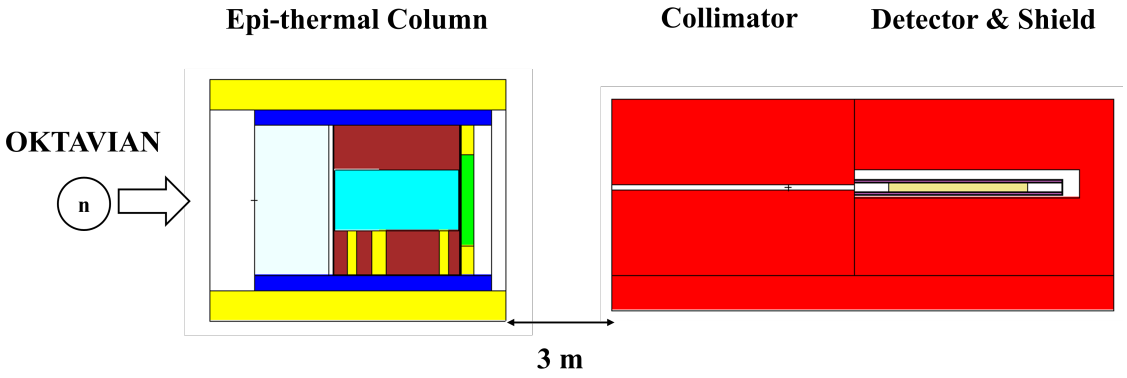


Figure 3.6: Schematic sketch of the entire design of the pencil-beam neutron source (included the collimator designed the following Section).

3.2.2 Detector assignment

Neutrons reached the detector after passing through the collimator. To shield the detector from wall-scattered neutrons, polyethylene blocks were installed around it. Also, Boron carbide and cadmium were covered around the detector to shield thermal neutrons. Figure 3.6 also shows the design of detector and surrounding shielding components.

3.3 Collimator Design and Its Performance

This section outlines the design work of the collimator to create the beam-neutron source. Nowadays, the application of the beam neutron source varies in the fundamental research about BNCT, material testing, and imaging technique [103, 104]. Since this designed beam neutron source is also applicable for these objectives, this section investigates the beam characteristics through the MCNP, as shown in **Section 3.3.5**.

3.3.1 Design goals and Parameters

The material, length, diameter, and distance to the epi-thermal column were determined with these criteria:

- The ratio of the ^{3}He (n, p)^{3}H reaction rate by "component A" neutrons (R_A) is over 99 %
- The total count of neutrons in one irradiation experiment (= 5 hours irradiation) is over 10^4

The neutron detection incident in PSPC was separated into three, as shown in Figure 3.1. "Component A" neutrons are appropriate for estimating the energy spectrum because they faithfully represent the decay system through the detector. On the other hand, "Component B and C" neutrons are the crucial factors for overestimating the depth distribution.

Based on these design goals, we designed the following 4 parameters:

(1) **Material**

(2) **Width**

(3) **Hole Diameter**

(4) **Distance between the epi-thermal column**

The design work was performed through the Monte Carlo simulations using MCNP 5 [94]. Based on the Figure 2.13, we modeled 40 cylinders to reproduce the position-sensitivity of PSPC, and the ^{3}He (n, p) ^{3}He response rate was calculated as the depth distribution in variety of parameters. Note, that the JENDL-4.0 [98] was used in this work.

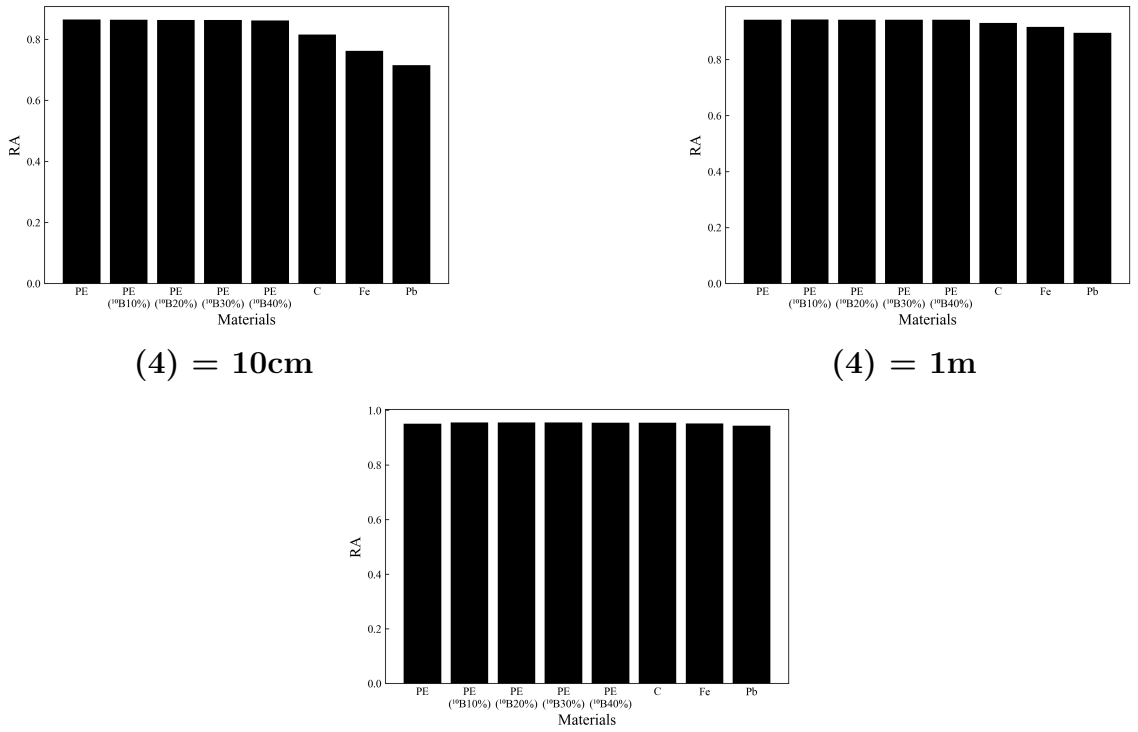


Figure 3.7: R_A values in materials. Other parameters are (2) = 20 cm, (3) = 4 cm, and (4) varies 10 cm, 1 m, and 5 m, respectively. These values are based on the previous study, and it revealed that R_A depends on the parameter (4). Therefore, we changed the value of parameter (4) and performed simulations.

3.3.2 Collimator Material Selection

We selected the material of the collimator first because it acts as a "moderator," and its performance does not depend on the configuration of other materials. Considering the cross-sections and nuclear interactions with epi-thermal/high energy neutrons, candidate materials are stainless, carbon, lead, polyethylene, and boron contained polyethylene, respectively. Stainless was included because of the high-cross section for the high-energy neutrons, and carbon and lead were expected as effective reflecter that contributes to the high production of neutrons. Polyethylene is well-known moderator that is used in various detector for low-energy neutron spectrometry [47, 90], and the boron was also taken into account to investigate the impact of its high neutron absorption [64].

Figure 3.7 presents the simulation results of R_A, indicating that values of with/without polyethylene are larger than others. Besides, remarkable discrepancies weren't observed among polyethylene-based collimator, because its cross-section decreased in the neutron energy and it doesn't strongly affect on the R_A. Therefore, we determined the polyethylene as the parameter (1).

Table 3.1: Parameter candidates prepared for the first preliminary calculation. In this part, we calculated N_B in $3 \times 3 = 27$ points to find the neutron's behavior.

Width of collimator (cm)	20	50	70
Hole diameter of collimator (cm)	2	5	8
Distance between collimator and the epi-thermal column (m)	1	3	5

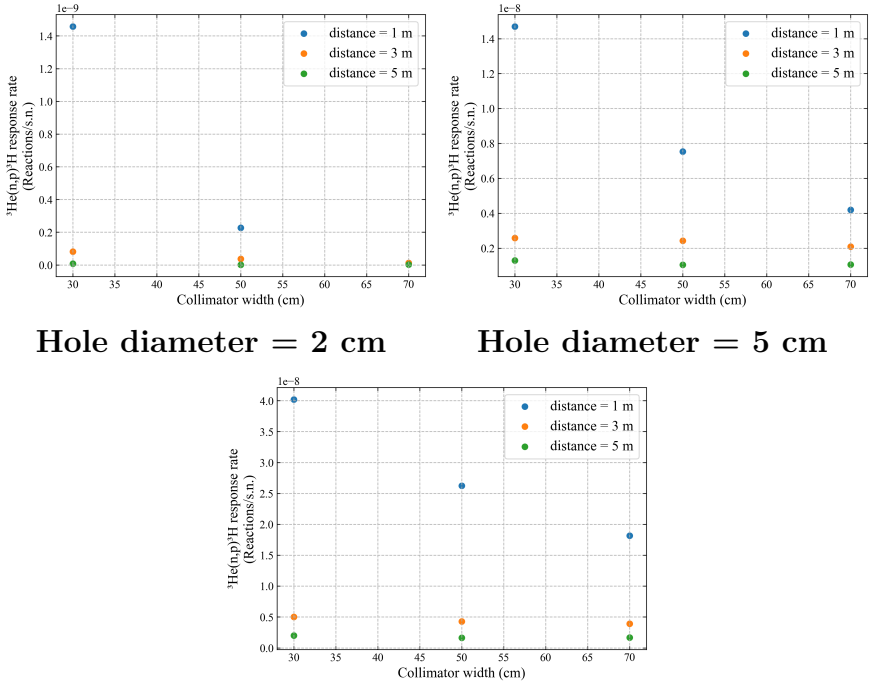


Figure 3.8: Preliminary calculations of ^{3}He (n,p) ^{3}H response rate by neutrons assigned to component B neutrons ($\boldsymbol{R_B}$). Error is small enough not to be stated.

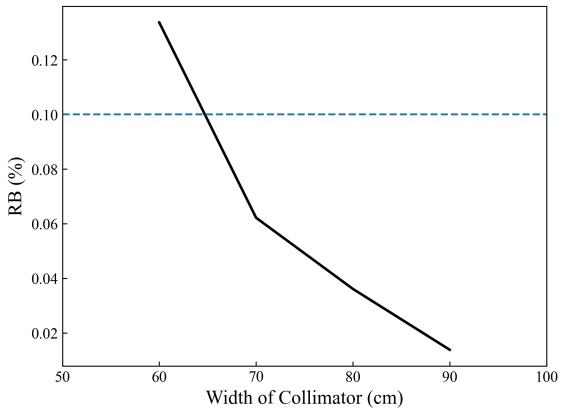


Figure 3.9: $\boldsymbol{R_B}$ values in the collimator width (2).

3.3.3 Preliminary Calculations and the Trend Analysis

We performed preliminary calculations with 27 candidates of all other parameters to find the behavior of the target values (R_A and N_A). We prepared 3 parameters for each parameter, and conducted $3 \times 3 = 27$ points simulations (See Table 3.1). Notably, polyethylene was selected as the material of the collimator. Then, we especially focused on the component B neutrons (See Figure 3.1), and Figure 3.8 depicts the relationship between the Flux B values (N_B) and the width of the collimator (parameter (2)). Regardless of the value of (4), at (2) = 70 cm and (3) = 2 cm, N_B becomes considerably small and can be understood to decrease significantly. It impried the following two points:

i N_B values sharply decreased when the hole diameter $\leq$ 2.5 cm (smaller than the diameter of PSPC)

ii N_B values became small when the width is equal to 70 cm

These findings mean the contribution of neutrons in component B can extremely decreased by getting the hole diameter of the collimator less than the diameter of the detector. Thus, the collimator needs **the hole diameter (parameter (3) should be $<$ 2.5 cm)**. For the finding ii, N_B became very small, but further evaluation is needed to decide whether the value (2) = 70 cm is acceptable. In light of this, we determined the width of the collimator (parameter (2)), with the additional design goal below:

The ratio of the ^{3}He (n, p) ^{3}H reaction rate by "component B" neutrons (R_B) is smaller than 0.1 %

Regarding the method for determining (3) and (4), we aimed at "improving the measurement accuracy in the verification experiment," which is the objective of this study. That is, for the values of (3) and (4), we evaluated the uncertainties introduced by R_A and N_A, respectively, and selected the values that minimize their sum, ϵ_{total}. Taking into account actual experiments, the error can be obtained analytically, and it is divided into two types of errors:

$$\epsilon_{total} = \epsilon_{sys} + \epsilon_Y \tag{3.3}$$

Where, ϵ_{sys} means the systematic error, and ϵ_Y is the counting error of PSPC. ϵ_{sys} means neutrons from the side surface of PSPC were regarded as the error factor. Considering that, the ϵ_{sys} is evaluated as shown in Equation (3.4),

$$\epsilon_{sys} = 1 - R_A \tag{3.4}$$

On the other hand, since the count in the detector adheres to the Poisson distribution [48], ϵ_Y was defined in the following Equation (3.5):

$$\epsilon_Y = \frac{y_i}{\sqrt{N_A}} \tag{3.5}$$

Where y_i is the PSPC's count in the experiment as follows,

$$y_i = c_i \times V \times I \times S \times t \tag{3.6}$$

Where $_i$ is the ^{3}He (n, p) ^{3}H response rate calculated in MCNP, I is the neutron intensity of the source, S is the space of the PSPC, and t is the irradiation time. In this Section, each parameter is 10^9 (n/s), 4.9 cm^2, and 8 hours, respectively.

3.3.4 Parameter Determination

According to the baseline developed in the previous Section, we next determined the (2) width of the collimator. The other parameters were set as follows: (1) polyethylene, (3) 2 cm, and (4) 100 cm. Figure 3.9 shows the simulation results in the collimator width. R_B reached under 0.1 % when the width was 70 cm, so we determined the collimator width as 70 cm. Finally, we optimized the parameter (3) and (4) simultaneoulsly, in order to minimize the "Total Error (ϵ_{total})" (See the Equation (3.3) in Section 3.4). To narrow down the group of the two parameters, another preliminary calculation was performed with the 30 candidates as displayed in Table 3.2. Then, errors were obtained based on Equations (3.4 and 3.5), illustrating as the heatmap (See Figure 3.10).

Table 3.2: Parameter candidates prepared for the first preliminary calculation. In this part, we calculated R_A and N_A in $6 \times 5 = 30$ points.

Hole diameter of collimator (cm)	1	1.5	2	2.5	3	4
Distance between the collimator and the column (m)	1	2	3	4	5	



Figure 3.10: ϵ_{total} colormap calculated in parameters that were listed in Table 3.2.

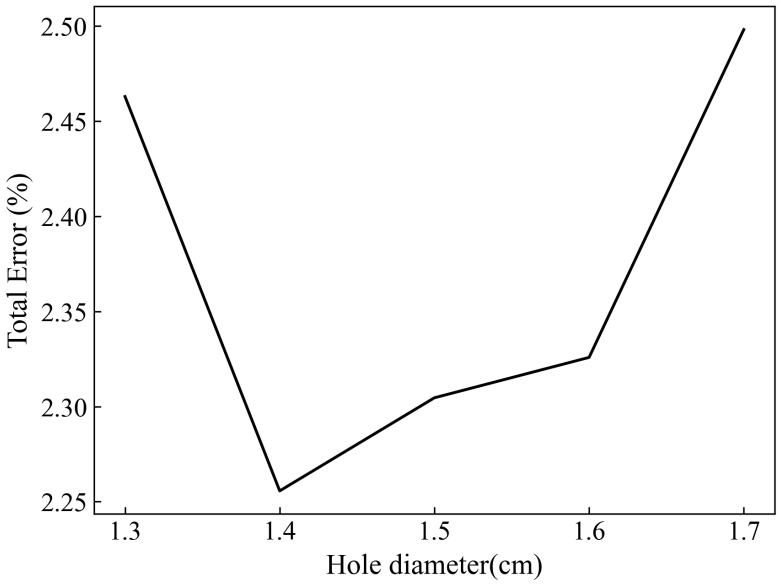


Figure 3.11: ϵ_{total} values in the hole diameter (3) of the collimator.

Table 3.3: Collimator parameters and its performance [105]

parameters	Values
Material	Polyethylene
Width	70 cm
Hole Diameter	1.4 cm
Distance between epi-thermal column and collimator	3 m
R_A	99.7 %
N_A	2.7×10^3
R_B	7.8×10^{-3} %

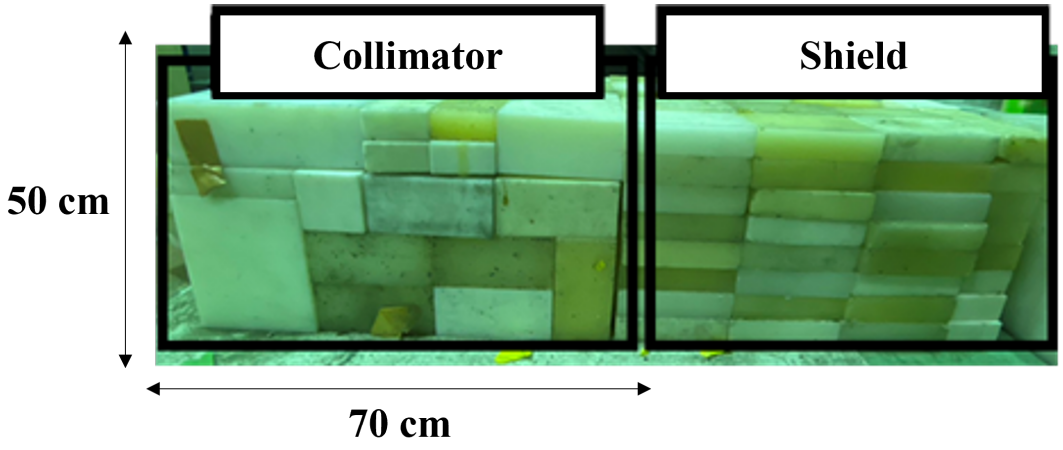


Figure 3.12: Developed collimator and shield covering PSPC [105].

According to this heatmap, ϵ_{total} was the smallest when (hole diameter (3), distance (4)) = (1.5 cm, 3 m). Since the ϵ_{total} depends on the hole diameter rather than on the distance, we analyzed the ϵ_{total} in the hole diameter, as shown in Figure 3.11. As a result, ϵ_{total} got the smallest value when the hole diameter was 1.4 cm. Therefore, we determined the parameter (3) and (4) were (1.4 cm, 3 m).

Results were shown in Table 3.3, and each collimator parameter is Polyethylene: 70 cm, 1.4 cm, and 300 cm, respectively. According to this table, almost neutrons can be collimated; however, it cannot be obtained enough counts to achieve the design goal. It will be addressed by extending the irradiation time, for instance, we can get more than 10^4 counts in 24 hours irradiations. In the following Sections, we performed the simulation works using this beam-type neutron source.

Figure 3.12 illustrates the schematic sketch of the designed collimator through these simulation work.

3.3.5 Beam Characteristics

In future, the beam characteristics will be investigated by the irradiation experiment. The neutron flux will be measured by activation foils (an Au foil e.g.), and the spatial distribution can be obtained by exposure to the IP-ND. Therefore, in this simulation work, the spectrometer was removed in order to investigate the beam properties.

Figure 3.13 depicts the simulation system to examine them. We calculated the horizontal flux distribution from the exit of the collimator in 5 cm steps by F2 tally of MCNP on behalf of the activation foils behavior, and the neutron flux in radial axis at each point was calculated as IP-ND's behavior.

First of all, design requirements were defined to evaluate the beam performance:

i. The reduction of neutron fluxes horizontally, Φ_h (x) is $\geq$ 90 %

ii. The ratio of neutron flux inside the diameter of the PSPC ($d \leq 2.5$ cm), R_{inside} at x cm $\geq$ 99%

The neutron flux at the collimator exit had already decreased, as shown in Figure 3.17 (b) and Figure 3.5. This indicates that a longer acquisition time would be required to obtain sufficient detector counts from a statistical perspective. We assumed that a 10% reduction in Φ_h was acceptable and therefore defined Design Goal iaccordingly. The neutron flux within the PSPC diameter (Φ_r) is also an essential parameter for estimating the energy spectrum from the depth distribution. We required $R_{\mathrm{inside}} \geq 99\%$, because the smaller the neutron leakage outside the detector becomes, the better the reconstruction performance is.

Figure 3.14 shows the lateral neutron-flux distribution obtained in this study. The red dotted line indicates the entrance position of the PSPC. We defined regions in which the neutron flux remains above 99% of the flux at the PSPC entrance as exhibiting high beam performance (highlighted in orange). Accordingly, this beam – neutron source can maintain a high flux level even 55 cm downstream of the collimator exit. In particular, Φ_h remains stable from x = 10 cm to 30 cm, which corresponds to the region spanning from the PSPC entrance to 20 cm downstream.

According to Ref. [52], discrepancies were observed between the experimental and calculated depth distributions. We considered that the presence of the neutrons from the side surface of PSPC attributed to this phenomenon, so such disagreements can be reduced using this neutron source.

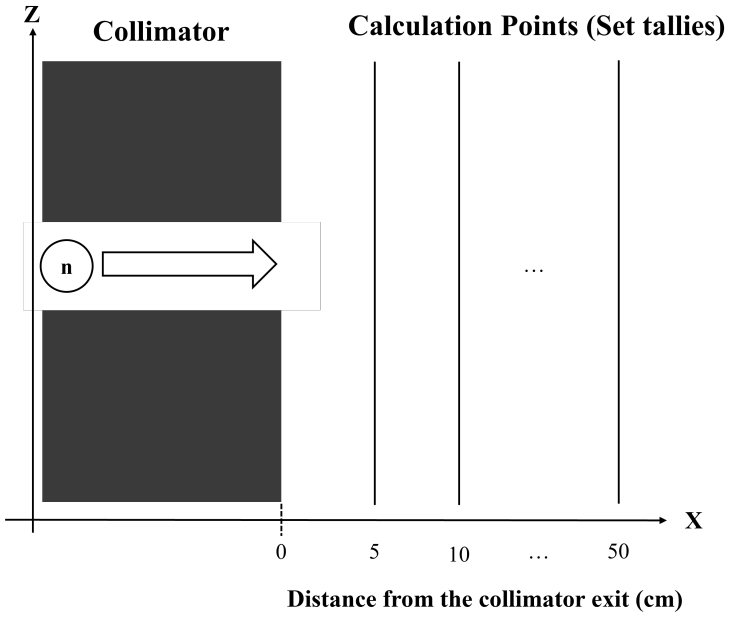


Figure 3.13: Simulation system for the beam characterization calculations.

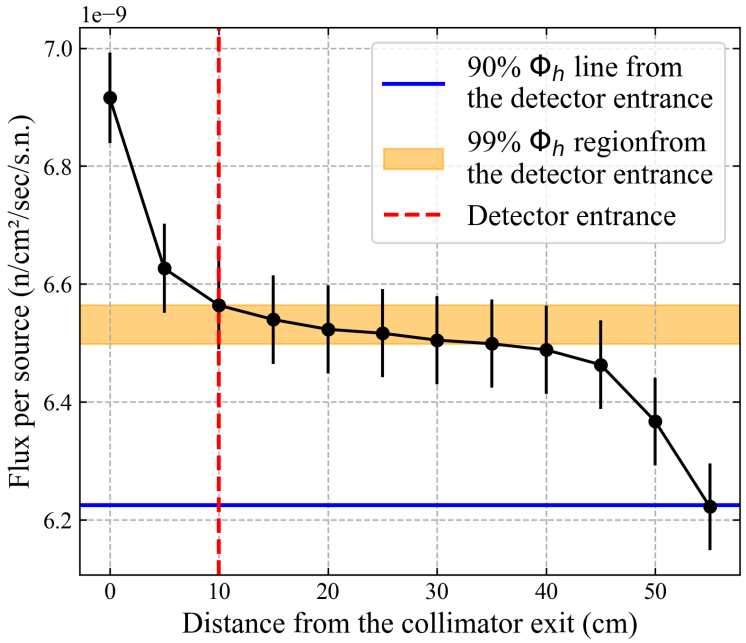


Figure 3.14: Simulation system for the beam characterization calculations.

Figure 3.15 shows the radial distribution calculated in MCNP. Two dotted lines with red color mean diameters of the collimator and the PSPC, respectively. Result shows the high concentration of this designed neutron source, the neutron flux decreased as the radius is larger. R_{inside} in each point was calculated, as shown in Figure 3.16. Compared to the design requirements, R_{inside} remained 99 % up to almost 30 cm behind the exit of the collimator. We therefore concluded that this designed collimator has a potential to create a sufficient effective neutron beam in that distance, which can be applied for various topics in fundamental engineering researches about low-energy neutrons. The detail angular beam spread will be examined by the irradiation experiment to IP.

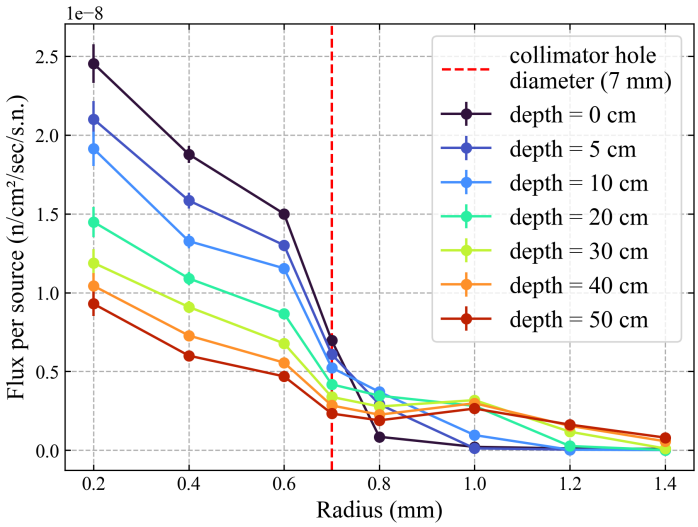


Figure 3.15: Radial distribution of neutrons from the exit of the collimator.

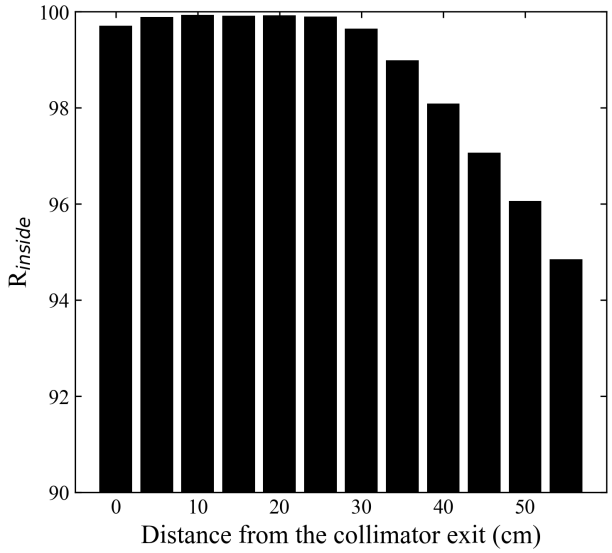


Figure 3.16: Radial distribution of neutrons from the exit of the collimator.

3.4 Numerical Analysis

3.4.1 Simulation condition

To validate the effectiveness of the designed beam neutron source, numerical experiments were conducted within this experimental system. Figure 3.17 presents the strategy for the numerical analysis. In this study, we employed MCNP 5 to obtain the reference spectrum ($\boldsymbol{\Phi_{ref}}$) and depth distribution y based on this experimental system. Then, $\boldsymbol{\Phi_{ref}}$ was compared to ref derived from y using Equation (2.51). As shown in Figure 3.17, $\boldsymbol{\Phi_{ref}}$ was the simulation value at the entrance of the detector. Higher-energy neutrons (over 10 keV) are present in the experimental environment; however, such effects are expected to be small due to the low response and small magnitudes of the spectrum. We divided the energy bin into 43 groups (j = 43) with the same lethargy ($10^{0.1}$) across the epi-thermal region and conducted the estimation.

We first examined the robustness of this approach by incorporating normal distributions that represent counting errors. As discussed in **Chapter 3.3.3**, the experimental results are assumed to contain uncertainties, ϵ_s and ϵ_y, which together constitute the total error, ϵ_{total}. Because the unfolding outcomes are influenced by these uncertainties, the procedure must maintain a sufficient level of robustness against them. In this study, we considered that the limited robustness observed in the unfolding process primarily originated from neutrons entering through the lateral surfaces of the detector. We hypothesized that using a beam-type neutron source would mitigate this issue. To validate this hypothesis, we first performed numerical experiments under ideal conditions and then introduced controlled errors, as summarized below:

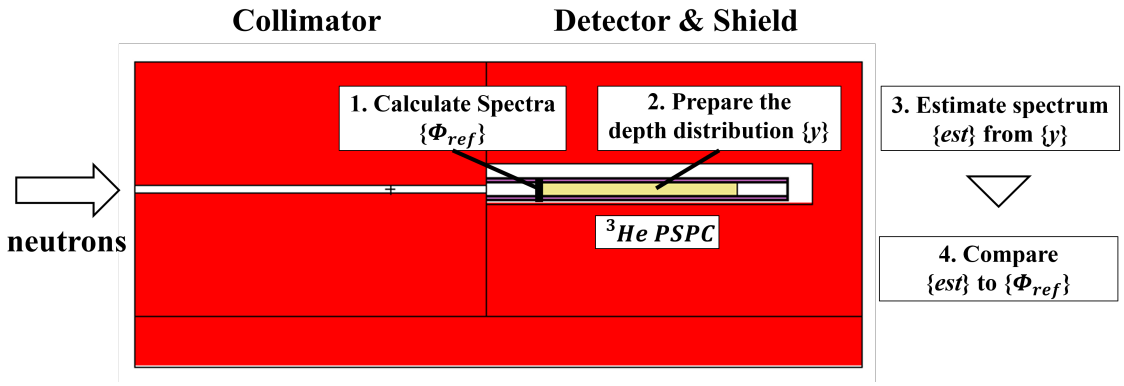
i. $\boldsymbol{R} \times \boldsymbol{\Phi_{ref}}$

ii. $\boldsymbol{R} \times \boldsymbol{\Phi_{ref}} + \boldsymbol{\epsilon}$ (e % Normal Distribution)

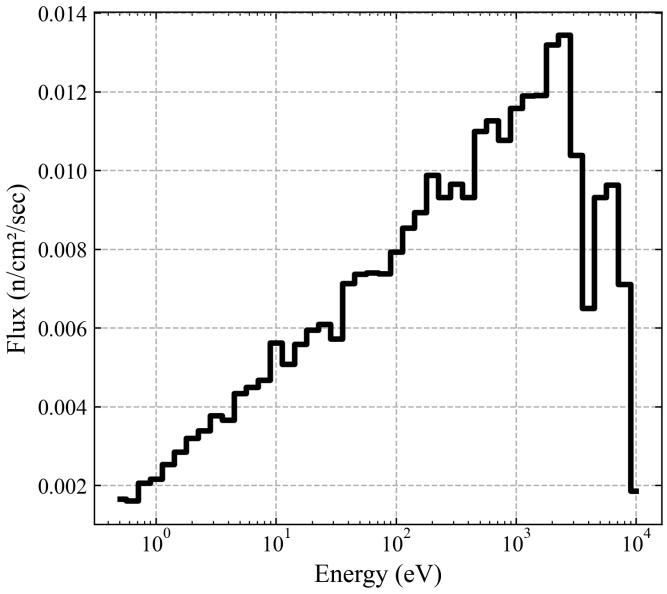
iii. Calculated $\boldsymbol{Y}$

Where e corresponds to ϵ_t, and this study assumed it varies from 1 % to 10 %.

Figure 3.18 shows the result of $\boldsymbol{\Phi_{ref}}$ and $\boldsymbol{\Phi_{est}}$ for the designed pencil-beam neutron source. Table 3.4 exhibits the statistical tests, RMSE and NRMSE values in each case. From the statistical point of view, the estmated spectrum has 30 % discrepancies in average, and it was increased as the error was added. Moreover, the estimated value from the calculated $\boldsymbol{Y}$, assuming the experimental result may cause huge discrepancies (67 %) compared to the reference.



(a)



(b)

Figure 3.17: (a) strategy of the numerical analysis in this Section. We aimed to compare the energy spectrum at the entrance of the PSPC. The $\boldsymbol{\Phi_{ref}}$ value was calculated at this point, and the $\boldsymbol{\Phi_{est}}$ values were derived from several candidates of depth distribution. (b) A $\boldsymbol{\Phi_{ref}}$ distribution in this Section calculated in MCNP.

Table 3.4: Results of numerical analysis for each situation.

Cases	RMSE Values	NRMSE Values (%)
$\boldsymbol{R} \cdot \boldsymbol{\Phi_{ref}}$	1.81×10^{-3}	30.2
$\boldsymbol{R} \cdot \boldsymbol{\Phi_{ref}} + \epsilon(1\%)$	1.82×10^{-3}	30.3
$\boldsymbol{R} \cdot \boldsymbol{\Phi_{ref}} + \epsilon(3\%)$	1.85×10^{-3}	30.9
$\boldsymbol{R} \cdot \boldsymbol{\Phi_{ref}} + \epsilon(5\%)$	1.92×10^{-3}	32.0
$\boldsymbol{R} \cdot \boldsymbol{\Phi_{ref}} + \epsilon(10\%)$	2.19×10^{-3}	36.6
Calculated $\boldsymbol{Y}$	4.31×10^{-3}	67.0

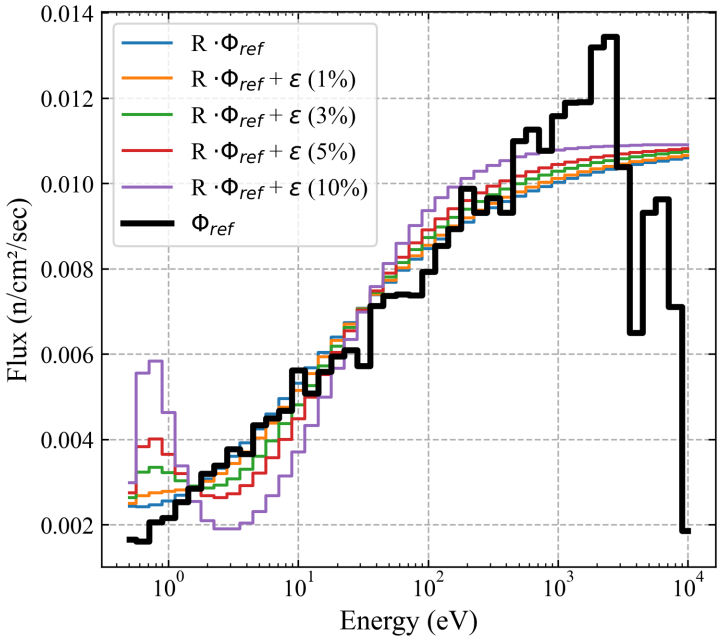


Figure 3.18: Comparisons between $\boldsymbol{\Phi_{ref}}$ and $\boldsymbol{\Phi_{est}}$ as the error added by implementing the pencil-beam neutron source $\boldsymbol{\Phi_{est}}$ values were estimated from depth distribution that corresponded to the matrix of $\boldsymbol{R}$ and $\boldsymbol{\Phi_{ref}}$.

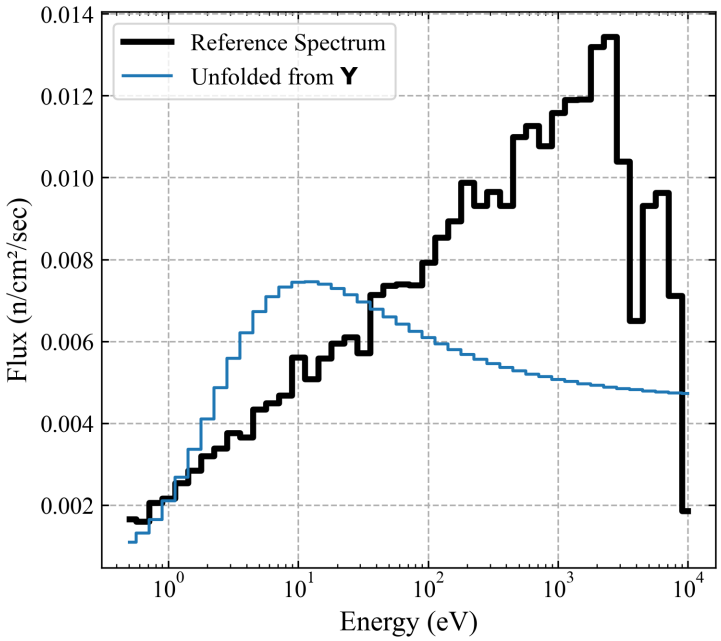


Figure 3.19: Comparisons between $\boldsymbol{\Phi_{ref}}$ and $\boldsymbol{\Phi_{est}}$ as the error added by implementing the pencil-beam neutron source $\boldsymbol{\Phi_{est}}$ values were estimated from depth distribution that corresponded to the matrix of the $\boldsymbol{Y}$ calculated in MCNP.

3.4.2 Limitation of This Approach and its Correction

As a result of Figure 3.19, $\boldsymbol{\Phi_{est}}$ showed a different peak of the spectrum from $\boldsymbol{\Phi_{ref}}$. hese discrepancies were attributed to the mismatch between the theoretically ideal response function and the practical response. Consequently, the response function in Equation (2.64) does not fully reproduce the actual neutron behavior when entering the ^{3}He PSPC under the designed beam conditions. We considered this due to the lack of beam characteristics. Figure 3.21 (a) illustrates the input values in the ideal case ($R \times \Phi_{ref}$) and calculated $\boldsymbol{Y}$. It revealed that the discrepancies were located at depths beyond 30 cm of the PSPC. As neutrons reach the deeper location of the PSPC, they spread out and pass through from the side surface of the detector without any reactions (parameter C in Figure 3.1). To prevent this effect, the emission angle from the entrance of the detector (cos θ) requires over 0.999 ($cos\theta = cos(tan^{-1}(\frac{1.25}{30})) = 0.9991$). However, in that case, it isn't easy to get sufficient counts in PSPC.

In order to reflect on the experimental situation, values of the response function were corrected by the Monte Carlo simulation. Assuming the response as the ^{3}He (n, p) ^{3}H reaction rate in each part, we calculated it using the F4 tally in MCNP and replaced it in the section beyond the latter half of the PSPC (defined as $R_{corrected}$). Note, that the simulation strategy was illustrated in Figure 3.20. The theoretical value was derived from the Equation (2.63), while MCNP values are the simulation result. Also, SDEF and tally settings were presented in **Appendix D**.

Figure 3.21 (b - d) presents the comparison between theoretical response (R) and $R_{corrected}$. Differences are also observed in response to monoenergetic neutrons.

Using this response function, we obtained the $\boldsymbol{\Phi_{est}}$ in the case iii, as shown in Figure 3.22. It indicates the improvements of the estimation performance, a shift of the peak was observed. RMSE and NRMSE values were 2.43×10^{-3} and 37.8 %, respectively, so that the correction of the response function has a good impact on improvements of estimation quality. Compared to the previous study (See Figure 1.8), discrepancies in lower-energy range were successfully improved. However, discrepancies were still larger than those in Figure 3.18. Furthermore, the isuue of the estimation performance beyond 1 keV also remained. This is because of the poor energy resolution for higher energy neutrons (over 1 keV), that is explained in the concept of mean free length (l) below;

$$l = \frac{1}{\Sigma} \tag{3.7}$$

$$l = \frac{1}{N\sigma_t} \tag{3.8}$$

where σ_t is total cross-section in ^{3}He in this study. Since we assumed the pressure of this PSPC as 5 atm, and using the absorption cross-section of ^{3}He in thermal neutrons (5330 barn) and 1/v rule, l in 1 keV is written in

$$\sigma_a\ (1\ \text{keV}) = 5330 \times \sqrt{\frac{0.025}{1000}} = 26.8\ \text{barn} \tag{3.9}$$

$$l \simeq \frac{1}{(1.25 \times 10^{20}) \times (26.8 \times 10^{-24})} = 3.0\ \text{m} \tag{3.10}$$

Where N = P/kT, T is the temperature (293 K in this case, 0 degree). This value clearly indicates that the contribution of high-energy neutrons to this PSPC is quite small, resulting in the poor estimation performance in this region. While the beam-type neutron source can enhance the estimation performance in low-energy region, it was implied that there was a huge gap to evaluate the entire region of epi-thermal neutron in ^{3}He PSPC.

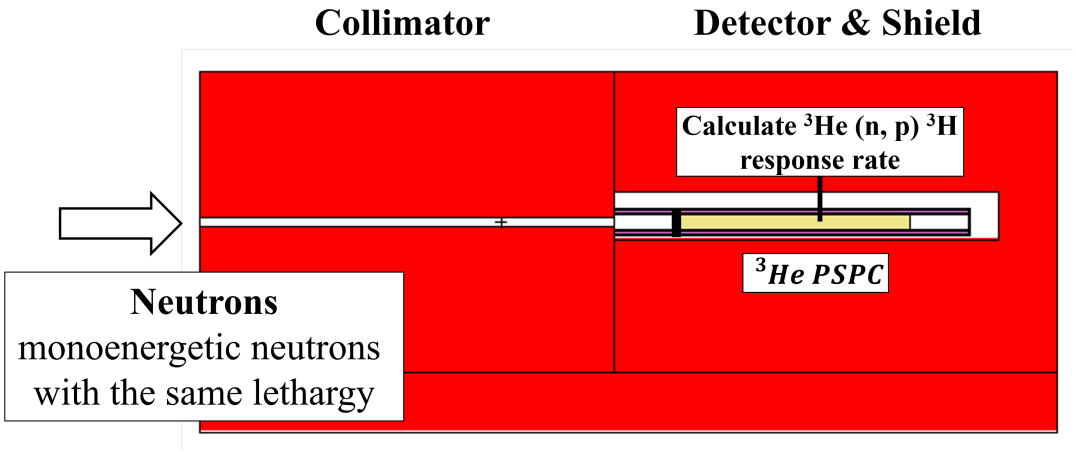
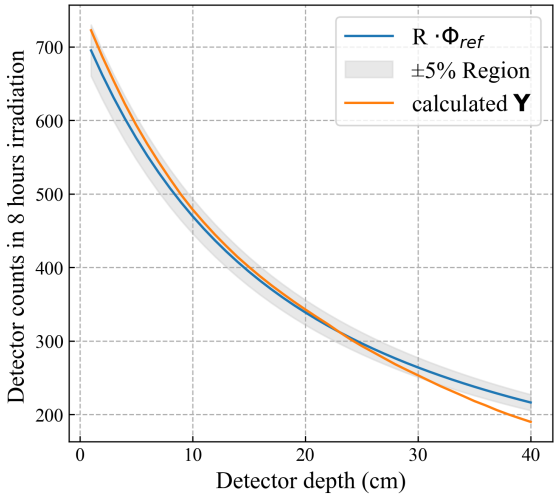


Figure 3.20: An Illustration of the response calculation method. As is the depth distribution, the ^{3}He (n,p)^{3}H response rate was calculated for the monoenergetic neutrons with the same lethargy.



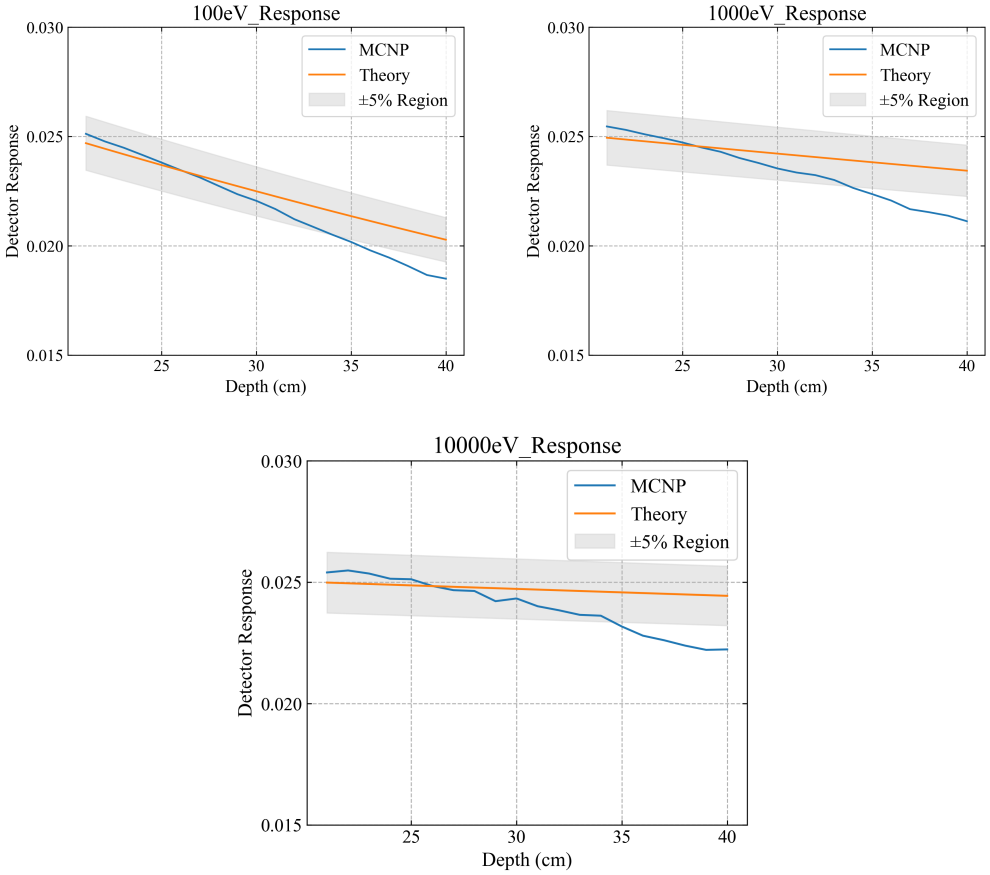


Figure 3.21: Comparison of the theoretical and the simulated detector responses, Depth distribution and detector responses for monoenergetic neutrons.

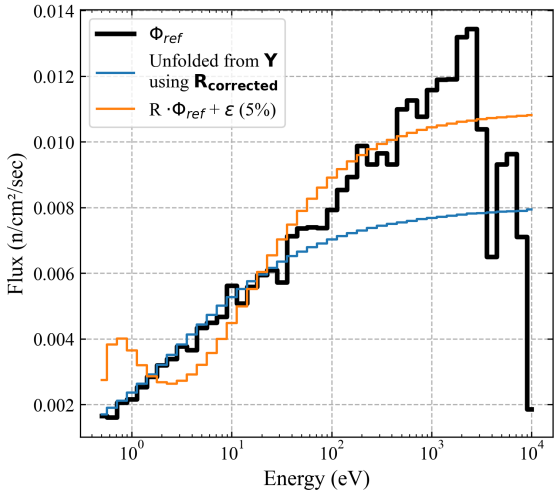


Figure 3.22: Comparisons between $\boldsymbol{\Phi_{ref}}$ and $\boldsymbol{\Phi_{est}}$ as the error added by implementing the pencil-beam neutron source $\boldsymbol{\Phi_{est}}$ values were estimated from depth distribution that corresponded to the matrix of the $\boldsymbol{Y}$ calculated in MCNP.

3.5 Summary

This chapter discussed the feasibility of a beam-type neutron source for the precise estimation of the epi-thermal neutron energy spectrum in a ^{3}He PSPC. The design of the beam-type neutron source was performed for the accelerator in my laboratory, OKTAVIAN, which is summarized in **Section 3.1**.

Section 3.2 described the structure of the experimental system, the epi-thermal column, the collimator, and the detector.

Before the validation experiment, numerical experiments were conducted to examine the robustness of this approach. Tentative depth distributions were generated with statistical errors, and the energy spectra were obtained in the unfolding process. They were compared to the reference spectrum, which is a calculated spectrum at the detector entrance. Results indicate that there are still discrepancies, especially in the higher energy region (1 keV to 10 keV), and it was found that the depth distribution also differed in deeper locations from the ideal one (completely convoluted the response function and energy spectrum, $\boldsymbol{Y}=\boldsymbol{R}\boldsymbol{\Phi}$).

To correct this effect, the response function was replaced by values calculated in MCNP 5. Using this response function, the unfolded energy spectrum reproduced the reference better than the unfolding result using theoretical response function. Results showed that the $\boldsymbol{\Phi_{est}}$ in lower-energy region was successfully reproduced with the $\boldsymbol{\Phi_{ref}}$; Thus, this approach has been demonstrated to be effective in neutron spectroscopy in the epi-thermal range.

In addition, an analysis of the beam characteristics for this neutron source revealed high beam quality 40 cm behind the exit of the collimator. This means that the designed beam neutron source can be applicable for other fundamental research, such as detector calibration in the epi-thermal range.

However, it still required corrections of the response function and the massive experimental system. Besides, the estimation accuracy in higher-energy region should be improved because the neutron energy in the recent BSA system might be higher than that of Reacter-based BNCT systems. To achieve this, the response modification process might be effective, as it did in this Chapter. The following chapter focuses on the improvements of the response function by the Monte Carlo simulation, performed in **Section 3.4.2**.

4 Design of Response Function in Monte Carlo Simulation

4.1 Introduction

Ideally, neutron incidents should be collimated well to achieve a situation assumed in the theoretical response function. However, there are a lot of obstacles, for example, neutron incidents reflected in the wall of the experimental room. Hence, it is extremely challenging to create a proper environment for the validation of this approach.

To deal with this issue, this Chapter presents an approach that applies a Monte Carlo (MC) simulation to create the response function. As discussed in **Section 3.4**, the detector's response function was corrected by evaluating the response in MCNP. his approach is commonly used in the context of radiation measurements, but it has not been investigated in PSPC yet. Since MC simulation can account for the neutron's behavior for each particle, it allows us to include neutron incidents entering the PSPC from the side surface as the "detector's response," not the illegal events. This advantage contributes to the mitigation of the beam characteristics as well as increasing the detector's count, reducing the statistical errors.

Section 4.2 introduces the way to create the response function for the PSPC in MCNP, and **Section 4.3** discusses the results of the numerical test, which aims to validate this approach is valid for the epi-thermal spectrometry. According to the results of the numerical tests, further discussions to enhance the estimation performance across the epi-thermal neutrons were also presented in **Section 4.4**.

4.2 Design of the Response Function

The response function of this spectrometer was evaluated by the ^{3}He (n, p) ^{3}H reaction rate for each monochromatic neutron in the epi-thermal range. As with the previous case, the neutron energy was divided into 44 equal-lethargy ($10^{0.1}$) groups in energies from 0.5 eV to 10 keV. To estimate the response function of the present PSPC, the spectrometer was separated axially into 40 groups for the length of the detector, 40cm, by 1 cm intervals.

In this Chapter, the heavy irradiation room was assumed as a neutron source to obtain high neutron intensity compared to the large experimental hall. Figure 4.1 shows the simulation geometry in this study. The PSPC is positioned at an opening in the wall, and the epi-thermal column based on Osawa's design is installed between the PSPC and the tritium target. A definitive difference from Osawa's model is that Carbon is installed surrounding the tritium target because the hole where PSPC is positioned is located vertically to the neutron's destination. Therefore, carbon plays a role in the reflector to concentrate neutrons in the right direction to the epi-thermal column. In addition, the concrete wall plays a role in the collimator, instead of the polyethylene in the previous Chapter.

Based on this simulation geometry, the response function of this spectrometer

and the reference spectrum ($\boldsymbol{\Phi_{ref}}$) were calculated, as shown in Figures 4.2 and 4.3, respectively. The detector response was calculated in the following Equation (4.1).

$$r_{i,j} = P_i(E = E_j) \times \pi d^2 \times x \tag{4.1}$$

Where P_i is the reaction rate of the (n, p) reaction at the i th interval of the PSPC, calculated using the F4 tally in MCNP, d is the radius of the PSPC, and x is the division interval of the PSPC (cm), with $i = 1$. The concept of the desing of response by Monte Carlo simulation was shown in Figure 3.20, that the SDEF and tally settings were presented in **Appendix D**.

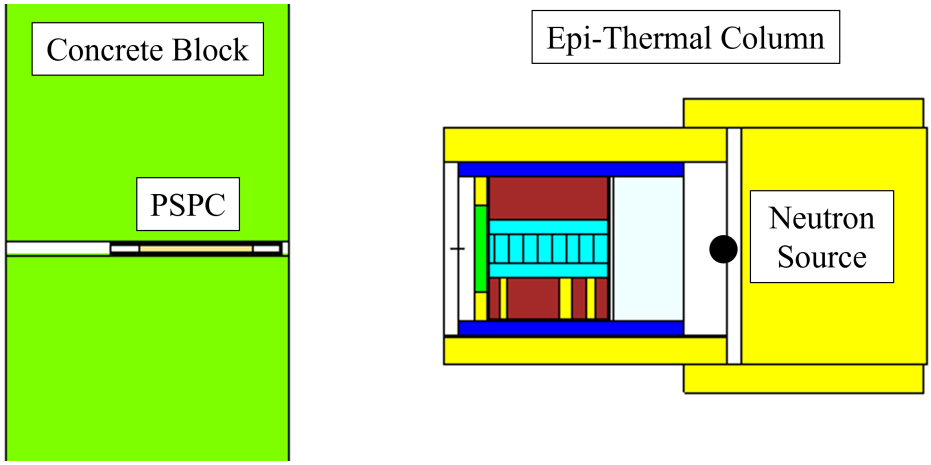


Figure 4.1: Simulation geometry to calculate the response function in the heavy irradiation room. Due to the spatial issue, the carbon blocks were installed to concentrate neutrons by the reflection.

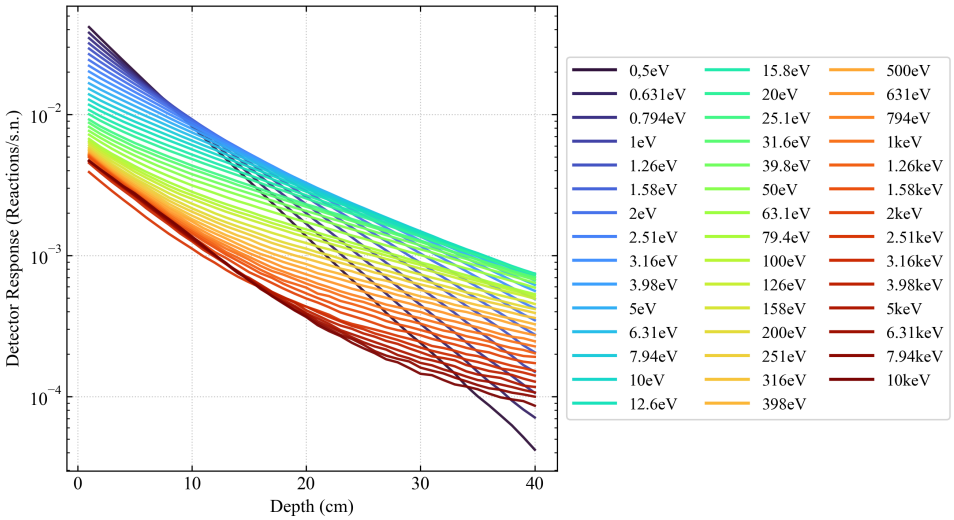


Figure 4.2: Response Function calculated in MCNP.

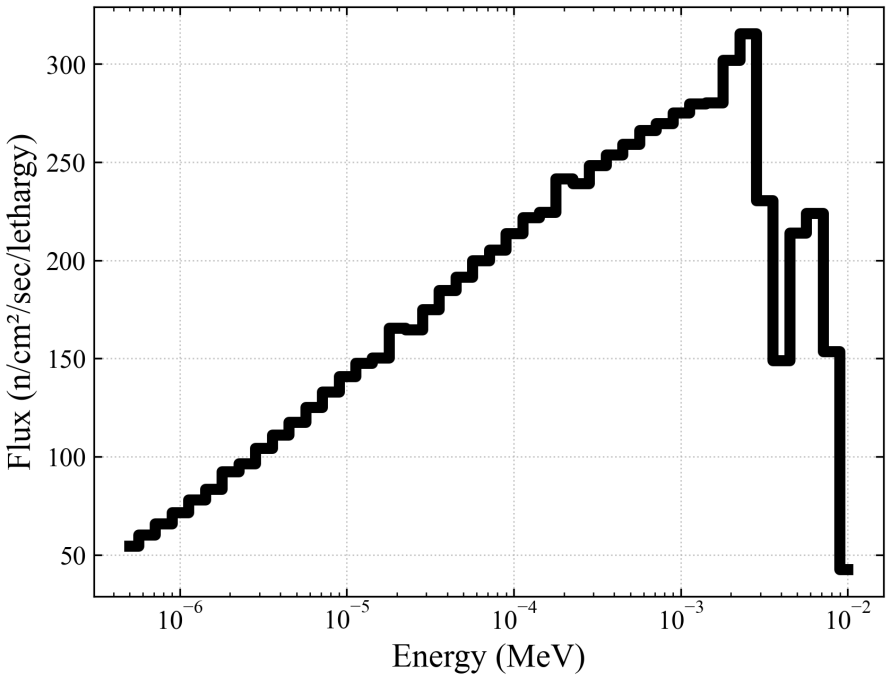


Figure 4.3: Reference Spectra ($\boldsymbol{\Phi_{ref}}$) in this Chapter.

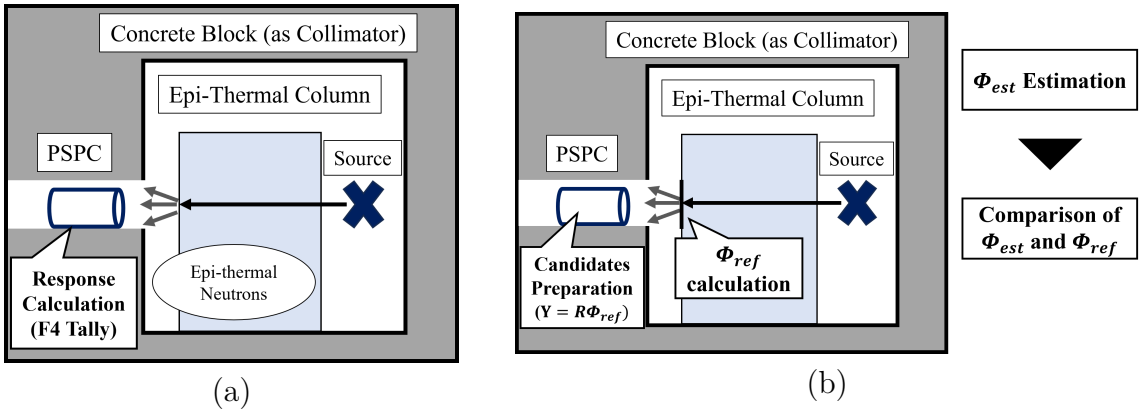


Figure 4.4: Procedures of the numerical analysis. Based on the response function calculated the process (a), several candidates of depth destribution ($\mathbf{Y}$) measured in PSPC, which adhere to Equation (2.63) were prepared. In addition, Φ_{ref} was calculated at the exit of the epi-thermal column. Φ_{est} were derived from for each candidate, using the Equation (2.51) (b).

4.3 Numerical Analysis

Several numerical experiments were conducted after evaluating the response function ($r_{i,j}$) to investigate the effectiveness of this method. These experiments converted several candidates for $\mathbf{Y}$ to the posterior distribution by Bayesian estimation to confirm the congruence of these distributions with the target value. Figure 4.4 shows the illustration on the numerical tests strategy in detail.

These values were compared with the calculated energy spectrum of the source. The following five values were the input for $\boldsymbol{Y}$:

(1) The matrix value of the response function and energy spectrum ($\boldsymbol{R\Phi_{ref}}$)

(2) $\boldsymbol{R\Phi_{ref}} + \boldsymbol{\epsilon}$ (1 % normal distribution)

(3) $\boldsymbol{R\Phi_{ref}} + \boldsymbol{\epsilon}$ (5 % normal distribution)

(4) $\boldsymbol{R\Phi_{ref}} + \boldsymbol{\epsilon}$ (10 % normal distribution)

(1) is the ideal case, if $\mathbf{Y}$ obeys the Equation (2.63). As for (2) – (4), uncertainty is added for the evaluation of counting uncertainty. In general, a counting error was observed in measured $\mathbf{Y}$ and evaluating the effect of uncertainty is important. Therefore, the error tolerance can be evaluated in this validation experiment by adding uncertainty to case (1) and conducting the estimation. (2) indicates that $\mathbf{Y}$ has a counting error of 1%. As for the iteration number, we applied "ideal iteration number" method for case (3) to determine it, as shown in **Section 2.3.3**.

Figure 4.5 shows the comparison between $\boldsymbol{\Phi_{ref}}$ and $\boldsymbol{\Phi_{est}}$ values, demostrating well agreements in the range from 0.5 eV to 4 keV, although the results do not agree in the higher energy region. Moreover, the discrepancies between the two became large as more errors. In this case, "error" means the counting error so that these results contribute to the determination of the counts required in the real experiment. Notably, the iteration number was 34 times, which was significantly smaller than other approaches. Statistical tests were also performed for these estimation results. RMSE & NRMSE values were summarized in Table 4.1. This table clearly exhibits very small increase/decrease of both statistical parameters, meaning that this estimation system has a great robustness for uncertainties.

Several things should be considered to improve the discrepancies. First, the effects of uncertainty need to be evaluated accurately. The calculated $r_{i,j}$ exhibited some uncertainty in MCNP. This $r_{i,j}$ is used repeatedly in this estimation; thus, each iteration increases the effect of the error. This could be the cause of the discrepancy between $\boldsymbol{\Phi_{ref}}$ and $\boldsymbol{\Phi_{est}}$ in case (1). Therefore, we should establish a more precise response function by increasing NPS, the number of particles simulated in MCNP.

The same applies to counting uncertainty: the larger the error, the greater the effect of repetition on the estimate. Hence, uncertainty in the counting rate should be as small as possible. In particular, irradiating neutrons for a long time to obtain many counting rates can be effective. Second, notably, the shapes of the response functions in the higher energy region are almost the same.

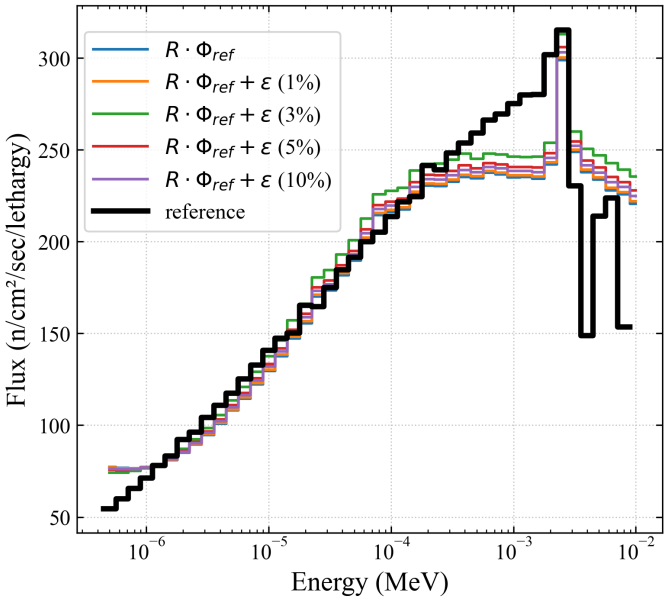


Figure 4.5: Results of the numerical analysis for each candidate, when concrete was applied to the collimator.

Table 4.1: RMSE & NRMSE values in candidate $\boldsymbol{Y}$ values.

$\boldsymbol{R\Phi_{ref} + \epsilon}$	RMSE value	NRMSE value
None error	37.09	0.233
$\boldsymbol{\epsilon} = 1\,\%$	37.13	0.234
$\boldsymbol{\epsilon} = 3\,\%$	38.76	0.244
$\boldsymbol{\epsilon} = 5\,\%$	37.60	0.237
$\boldsymbol{\epsilon} = 10\,\%$	37.31	0.235

The more the energy increases, the smaller the slope of the $\boldsymbol{r_{i,j}}$. These results reveal the poor energy resolution in a higher energy range of this spectrometer and that this spectrometer cannot discriminate higher energy neutrons. We should think of other approaches to improve the response function in the higher energy region (> 4 keV), particularly, using a longer detector, increasing the ^{3}He pressure, etc.

Furthermore, the characteristic of the response function at around 3 keV was considered to be involved in the high estimation performance. Figure 4.6 shows the response function around 3 keV, demostrating the unique behavior in the detector response at 2.51 keV. This characteristic might come from the resonance cross-section of sodium, that has a high cross-section at around this energy range, as shown in Figure 4.7 (a). Since there are no other nuclides exhibiting high-cross section around this energy range of all nuclide comsisting concrete wall (See Table 4.2), sodium is the main nuclide to affect this typical behavior. Figure 4.7 (b) illustrates the collision density of neutrons in concrete materials. This Figure shows the results from the top 5 nuclide of all components. According to the increase of the cross-section of

sodium, collision densities in other materials decreases, resulting in the decline of the performance as the moderator in Hydrogen. Therefore, more neutrons in about 2.85 keV enter the PSPC rather than neutrons having different energies, meaning such neutrons originally are moderated and become the lower energy that is enough to be detected in PSPC. Eventually, the response in this energy range became lower than other energy ranges.

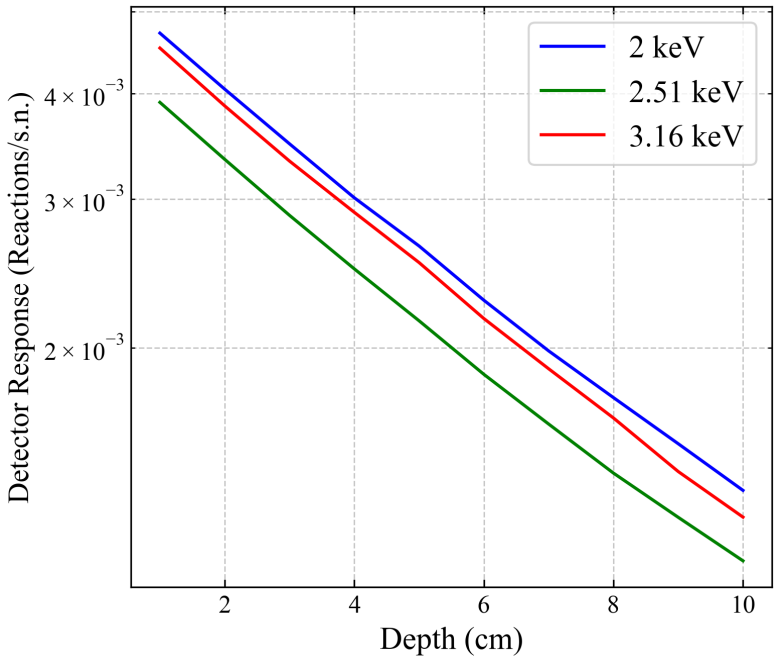


Figure 4.6: The response function in the first 10 cm depths calculated in MCNP. This result clearly shows the sharp reduction of the detector response in 2.51 keV.

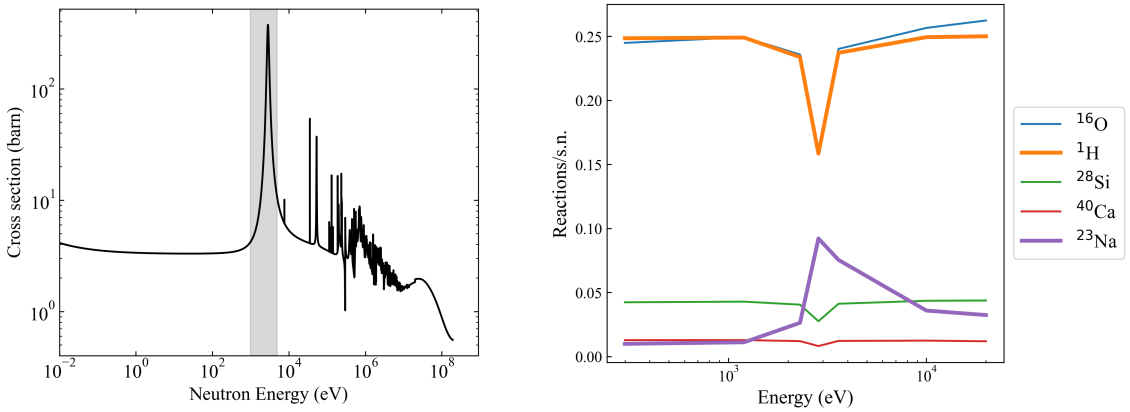


Figure 4.7: (a) The resonance cross-section of sodium. Data was extracted from [98]. (b) Collision densities of five nuclides which are top 5 of all concrete materials.

Table 4.2: Material components consisted of the concrete blocks in OKTAVIAN.

Elements	^{1}H	^{16}O	^{28}Si	^{29}Si	^{30}Si	^{27}Al	^{40}Ca	^{42}Ca
weight percentage (%)	0.55	48.96	28.67	1.46	0.96	4.49	7.89	0.05
Elements	^{43}Ca	^{44}Ca	^{48}Ca	^{32}S	^{34}S	^{54}Fe	^{56}Fe	^{57}Fe
weight percentage (%)	0.01	0.17	0.02	0.11	0.01	0.07	1.10	0.03
Elements	^{23}Na	^{24}Mg	^{25}Mg	^{26}Mg	^{39}K	^{41}K		
weight percentage (%)	3.42	0.19	0.02	0.03	1.76	0.13		

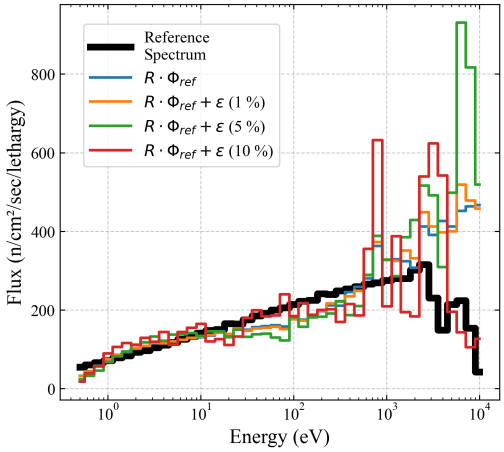


Figure 4.8: Comparisons between $\boldsymbol{\Phi_{ref}}$ and $\boldsymbol{\Phi_{est}}$ by implementing the polyethylene instead of the concrete blocks in this study.

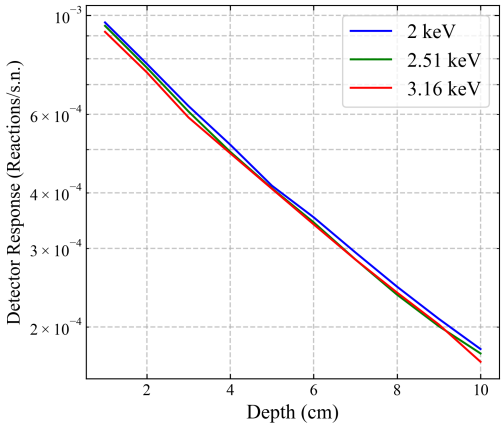


Figure 4.9: The response function of the first 10 cm depths of PSPC calculated in MCNP, when polyethylene was applied to the collimator. This result didn't show the typical response around this energy region.

In fact, the comparison between $\boldsymbol{\Phi_{ref}}$ and $\boldsymbol{\Phi_{est}}$ when applying polyethylene for the collimator indicates the large discrepancies at higher-energy range, as shown in Figure 4.8. Also, as compared the response functions around 2.85 keV between concrete and polyethylene (See Figure 4.9), a typical response was not observed. Therefore, the combination of materials which affect the neutron behavior with PSPC impries to be effective for improving the estimation performance.

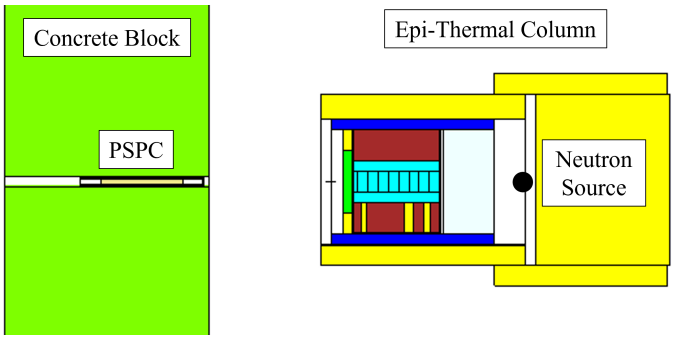
4.4 Further Improvements of This Spectrometer

Results in the previous section indicates the sodium plays an important role in enhancing the estimation performance at the typical energy region. This section discusses the potential application of this spectrometer for the spectroscopy in the higher energies Especially, we focus on the position of PSPC and the composition of sodium inside the concrete, that affect the shape of response function. The position of PSPC changes the amount of neutrons entering from the side surface. Also, it might be careful about the detector counts as its distance from the neutron source, which is relevant to the statistical error. On the other hand, sodium has a high cross-section at around 3 keV, as discussed in **Section 4.3**. In the previous section, the rate of atomic number density in sodium was 1.7 %, and the estimation performance might be changed by changing this rate. Furthermore, it can be effective by adding other materials that have high scattering cross-sections in epi-thermal range to cause a change in the detector response. The potential of this spectrometer was investigated by the same approach as previous section, preparing the response function using MCNP, and numerical analysis was performed for each situation.

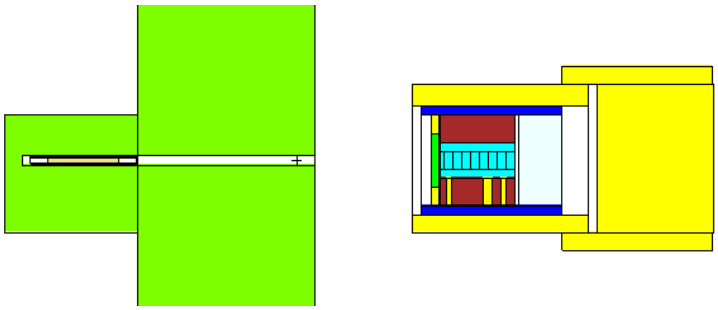
4.4.1 Influence of Spectrometer Position on Estimation Performance

This section features the position of PSPC spectrometer, as simulation systems were illustrated in Figure 4.10. Neutron counts and the number of neutrons entering from the side surface of PSPC are decreased as the distance of the neutron source. This study compared the results from the numerical analysis in these three cases; first of all, the response functions were calculated in MCNP, then energy spectrum was obtained in the same process of the previous section. Note that the true measured data ($\boldsymbol{R\Phi_{ref}} + \boldsymbol{\epsilon}(5\%)$, $\boldsymbol{R}$ is indivisual for each position of the spectrometer) was applied to $\boldsymbol{Y}$ in Equation (2.51), and the iteration number was determined by "ideal-number" method (See **Section 2.3.3**). The performance was evaluated in the iteration numbers and their RMSE values.

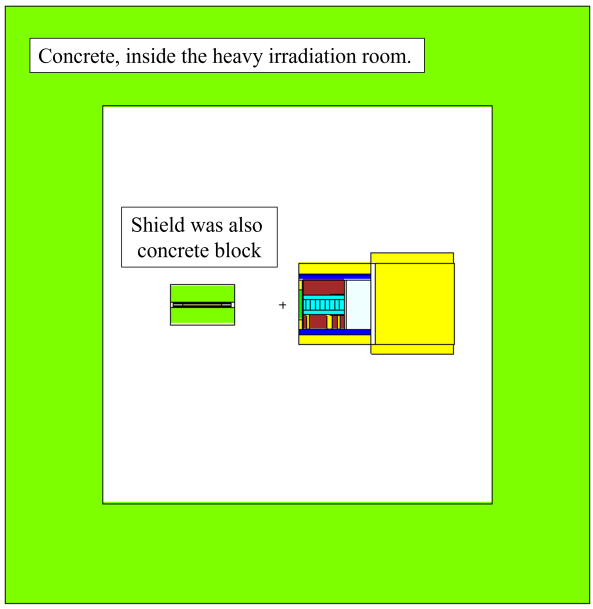
Figure 4.11 illustrates the unfolded spectra when the spectrometer was located in different distances from the neutron source, and Table 4.3 shows the results of statistical tests. In the previous Chapter, we considered that the ratio of neutrons entering from the side surface of PSPC was the crucial parameter which had effects on the unfolding performance. However, these findings showed the contrary. Even if the distance between the spectrometer and the epi-thermal column is close, unfolding spectra can reproduce the reference well.



(1): Inside the hole (same as **Section 4.3**)



(2): Outside the room



(3): Inside the room

Figure 4.10: Simulation systems to investigate the estimation performance in the detector position. (1): simulation geometry in the previous section, (2): PSPC was assigned to the outside of the experimental room, and (3): PSPC was assigned to inside the experimental room, assuming that the PSPC was covered by the concrete.

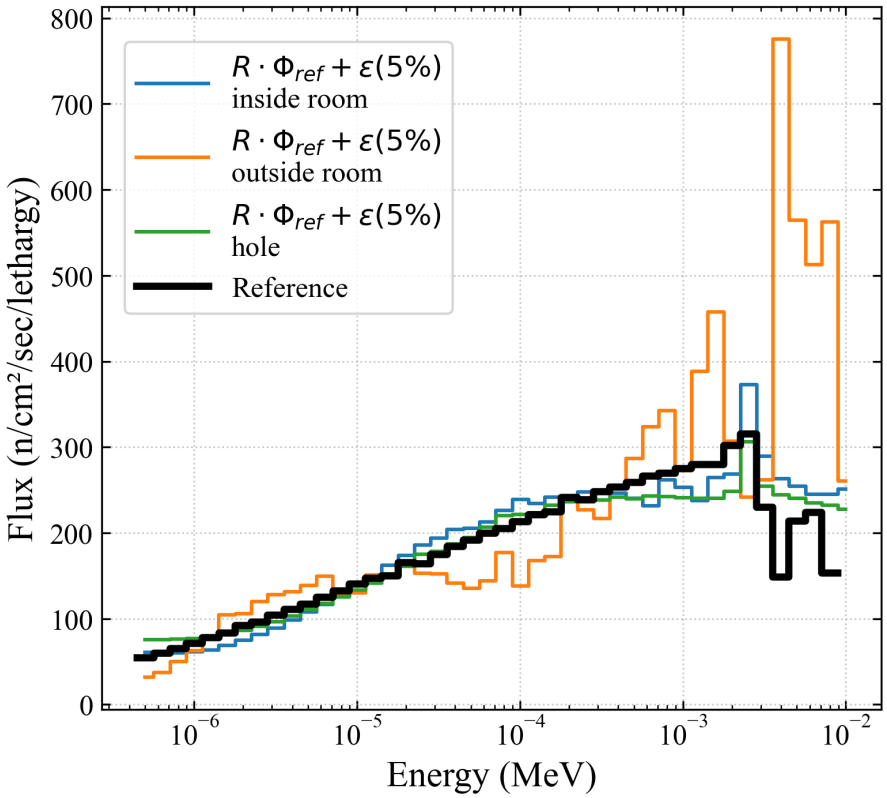


Figure 4.11: Estimated neutron energy spectra when the spectrometer was located in different positions.

Table 4.3: Iteration numbers and RMSE values in the sodium ratio

Spectrometer position	Iteration Number (times)	RMSE value
Inside the hole (1)	34	38.8
Outside the room (2)	678	43.78
Inside the room (3)	1459	1.43×10^2

4.4.2 Influence of Material Composition on Estimation Performance

This section features the material configurations surrounding PSPC spectrometer. The main approach is that we compare the estimation performance of the energy spectra with different sodium rates of atomic number density inside concrete; 1.7% (original), 3.4%, 10%, and 1%. Response functions in each sodium rate were calculated in MCNP, and then numerical analyses were performed. Figure 4.12 shows the energy spectra from the numerical analysis. As for the input data for unfolding process, it is almost the same as the previous section, ($\boldsymbol{R\Phi_{ref}} + \boldsymbol{\epsilon}(5\%)$, $\boldsymbol{R}$ is indivisual for each sodium ratio) was applied to $\boldsymbol{Y}$, and these criteria above were compared.

Results of statistical tests were also displayed in Table 4.4, indicating that the more the sodium contained in concrete, the more iteration numbers required, larger the discrepancies between the reference spectra. It was considered that the concrete block lost the function as moderator, as sodium rate was increased to concrete block. That's because of the fact that the ratio of hydrogen in concrete was decreased, which is the material used to moderate neutrons. Thus, these findings implied that the estimation performace can be enhanced by incorporating materials that have elastic scattering peak at the epi-thermal range into the concrete blocks. Moreover, this collimator should maintain the function as the moderator which is enough not to cause the decline of the estimation performance around 100 eV.

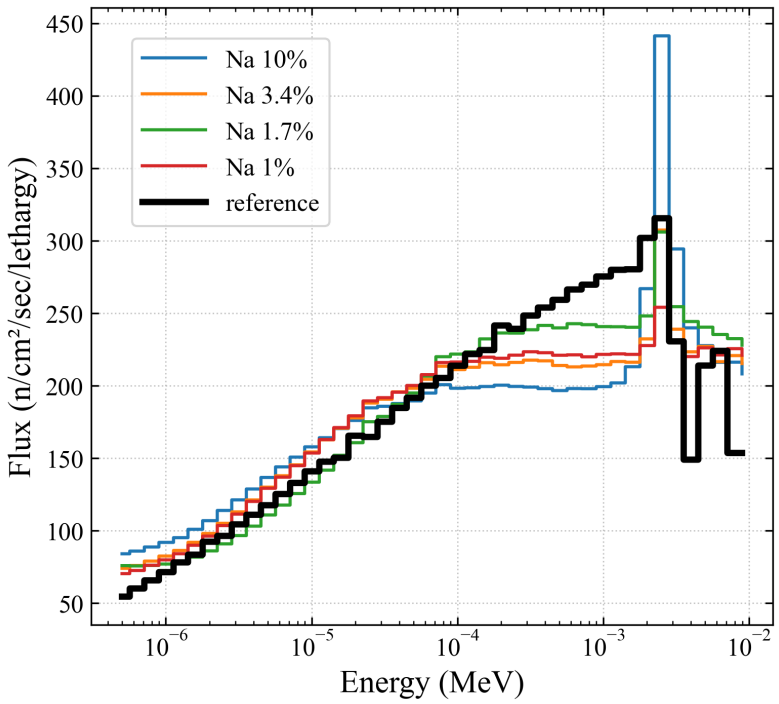


Figure 4.12: Estimated neutron energy spectra in different sodium ratio of the atomic number density inside concrete block.

Table 4.4: Iteration numbers and RMSE values in the sodium ratio

Sodium rate (atomic number ratio, %)	Iteration number (times)	RMSE value
1.7% (Original)	34	38.8
1%	78	40.8
3.4%	62	40.6
10%	1700	1.44×10^2

4.4.3 Potential for the Expansion of the Measurable Range

Previous sections discusses the slight changes in the configuration of the spectrometer and its materials' composition affect the estimation performance. As a result, the sodium rate and the detector composition have a crucial effect in enhancing it. These findings might be contributing to the wide-range spectrometer, not only for the PSPC, but also other conventional detectors.

First of all, by adding materials whose cross-section is effective in higher range than sodium, spectrometers can obtain the sensitivity at the region where its cross-section is effective. For instance, titanium is a potential candidate for this purpose, which has a high resonance cross-section at around 10 keV (See Figure 4.13). Furthermore, this system might be effective in other spectrometers, such as BSS, because it covered Au foils or ^{3}He counter by the polyethylene to reduce the neutron energy [46, 47]. Responses of these detectors depend on the moderator thicknesses and material compositions; thus, it is difficult to evaluate the response for accurate neutron spectrometry, only in polyethylene.

On the other hand, the application of the resonance reaction can enhance the sensitivity in the typical energy region. While just polyethylene is not insufficient to assess the wide-range energy, especially beyond 1 keV, the mix structure of the moderator with these materials can improve the estimation accuracy. These approaches has been carried out in the activation foils [106]; however, this approach utilized the moderator to cut off the contribution from the thermal neutrons and to adjust the effective cross-section of selected activation foils.

This approach can be compatible with our proposed method, so further research includes the optimization of the materials to allow the spectrometer acquire the sensitivity across the epi-thermal region, and then to evaluate the energy spectrum in higher energy region.

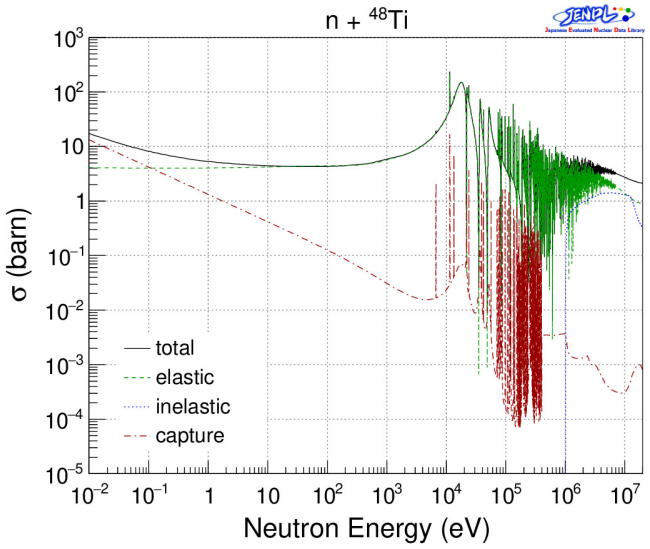


Figure 4.13: Illustration of the cross-section of ^{48}Ti [64].

4.5 Summary

In this Chapter, we have investigated the response function of the low-energy neutron spectrometer for epi-thermal energy region by the Monte Carlo simulation.

Initially, the response function was assessed even considering the spectrometer shield. Numerical experiments were then performed, considering the measuring uncertainty to confirm the availability of this response function in practical use. The energy spectrum was estimated by the Bayesian estimation. These results indicated that the feasibility of this approach was confirmed in the energy range from 0.5 eV to 4 keV. This information is useful to figure out the need for the number of counts in the experiment and the duration of the experiment. The causes of the discrepancies include poor response functions and low-energy resolution in the high-energy region in addition to counting and response function calculation uncertainty. Therefore, other approaches are crucial to represent well, particularly, using a longer detector or increasing the pressure of the detector.

Furthermore, the presence of sodium in concrete, which was placed as the collimator, was revealed the crucial factor to enhance the estimation performance by analyzing the collision density. This is because the sodium has a high resonance cross-section at around 3 keV, where the detector response was made a difference. According to the further analysis in **Section 4.4**, the percentage of the sodium contained in the concrete material, namely the surrounding material of the PSPC, clearly affects the estimation performance in the energy spectrum.

Therefore, we concluded that this approach was valid in the case of optimized material configuration. In addition, it was considered that it might be effective to enhance the estimation performance by adding contributions of unique nuclear reactions from other materials, for instance, activation reactions.

In the following Chapter, we proposed a new spectrometer by combining two different detectors which detect the signals by completely different mechanism, and analyzed the potential use of this hypothesis.

5 Simultaneous Utilization of PSPC and Activation Foils

5.1 Introduction

Considering the low-energy resolution to the higher (10 keV -) energy neutrons of this PSPC, there is a limit to the evaluation of the energy spectrum across the whole range of the epi-thermal neutrons. This Chapter proposes the combination of the multiple activation foil method with the PSPC spectrometer. Since the activation rates of materials can be represented in the MCNP simulations, the response function can also be prepared in the same approach as discussed in **Chapter 4**. The concept introduced in this chapter is formulated in terms of theoretical equations.

The activation rate ($\boldsymbol{A}$) is described in Equation (2.1), rewritten in

$$A = N \int \sigma(E) \cdot \Phi(E) \tag{5.1}$$

Where σ is the microscopic activation cross-section. If there are k pieces of information about activation rates, namely k materials used in the spectrometer, Equation (5.1) can be written as follows:

$$A_i = \sum_{i=1}^{k} \Sigma_{ij} \cdot \phi_j \tag{5.2}$$

where the $\Sigma = N \cdot \sigma$ in Equation (2.65), and energy spectrum was subdivided into m energy groups (j = 1 - m). Additionally, Equation (5.2) can be written as a matrix Equation,

$$\begin{pmatrix} a_1 \\ \vdots \\ a_k \end{pmatrix} = \begin{pmatrix} \Sigma_{11} & \cdots & \Sigma_{1m} \\ \vdots & \ddots & \vdots \\ \Sigma_{k1} & \cdots & \Sigma_{km} \end{pmatrix} \begin{pmatrix} \phi_1 \\ \vdots \\ \phi_m \end{pmatrix}, \tag{5.3}$$

The main concept is to merge this Equation with the one in PSPC as follows:

$$\begin{pmatrix} y_1 \\ \vdots \\ y_{40} \\ a_1 \\ \vdots \\ a_n \end{pmatrix} = \begin{pmatrix} r_{11} & \cdots & r_{1m} \\ \vdots & \ddots & \vdots \\ r_{n1} & \cdots & r_{nm} \\ \Sigma_{11} & \cdots & \Sigma_{1m} \\ \vdots & \ddots & \vdots \\ \Sigma_{k1} & \cdots & \Sigma_{km} \end{pmatrix} \begin{pmatrix} \phi_1 \\ \vdots \\ \phi_m \end{pmatrix} \tag{5.4}$$

Replacing the left-hand side by $\mathbf{Z}$ and the merged response function by $\mathbf{R}^*$, Equation 5.4 becomes

$$\mathbf{Z} = \mathbf{R}^* \, \mathbf{\Phi}$$
$$\begin{pmatrix} z_1 \\ \vdots \\ z_{n+k} \end{pmatrix} = \begin{pmatrix} r^*_{11} & \cdots & r^*_{1m} \\ \vdots & \ddots & \vdots \\ r^*_{n+k,1} & \cdots & r^*_{n+k,m} \end{pmatrix} \begin{pmatrix} \phi_1 \\ \vdots \\ \phi_m \end{pmatrix} \tag{5.5}$$

Activation foil data is crucial for enhancing the accuracy of spectrum unfolding by providing additional energy-specific information. The inherent limitation of the PSPC's length restricts the axial division to a maximum of 40 groups, resulting in challenges when reproducing the neutron energy spectrum up to 10 keV [49, 52, 54]. However, considering the spatial resolution of PSPC [93], the division of PSPC cannot be managed finer. Therefore, additional information from activation foils, especially at the higher energy range, helps to improve the estimation accuracy. First of all, 10 materials were selected in order to validate this approach as examples (See **Section 5.3**), and **Section 5.4** discusses the optimization of this approach, materials and their sizes.

5.2 Material Selection

As for the activation foils selection, materials were selected considering the activation cross-section to make their cross-sections have an unique value across the epi-thermal range. These materials have been widely used for neutron spectrometry, according to [42, 43, 107, 108]. In the first step to validate this apprach, 10 materials were selected ($A = [\mathbf{a_1}, \mathbf{a_2}, \cdots, \mathbf{a_{10}}]^{\mathbf{T}}$). Figure 5.1 shows the response ranges of selected activation foils in epi-thermal neutrons. ^{164}Dy, ^{115}In, ^{197}Au, and ^{186}W are used to evaluate neutrons in the 0.5 eV - 10^1 eV range, ^{107}Ag, ^{55}Mn, and ^{127}I below 1 keV neutrons, and ^{64}Ni, ^{98}Mo, and ^{75}As are beyond the 1 keV neutrons. Notably, the width is equal to the *length*, as exhibited in Table 5.1.

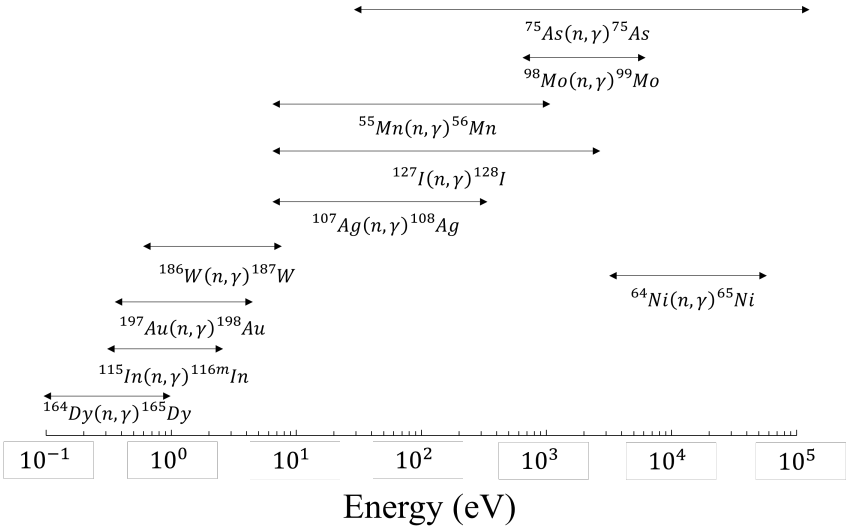


Figure 5.1: Response of the selected activation foils set-up in epi-thermal range.

Table 5.1: Material selection for activation foils.

Materials	Length	Thickness	Reaction interest
In	1	0.5	^{115}In (n, γ) ^{116m}In
Au	1	0.5	^{197}Au (n, γ) ^{198}Au
I	3	1	^{127}I (n, γ) ^{128}I
As	3	1	^{75}I (n, γ) ^{76}As
Ag	3	1	^{107}Ag (n, γ) ^{107}Ag
W	0.5	1	^{186}W (n, γ) ^{187}W
Ni	3	1	^{64}Ni (n, γ) ^{65}Ni
Mn	3	1	^{55}Mn (n, γ) ^{56}Mn
Mo	3	1	^{98}Mo (n, γ) ^{99}Mo
Dy	1	0.5	^{164}Dy (n, γ) ^{165}Dy

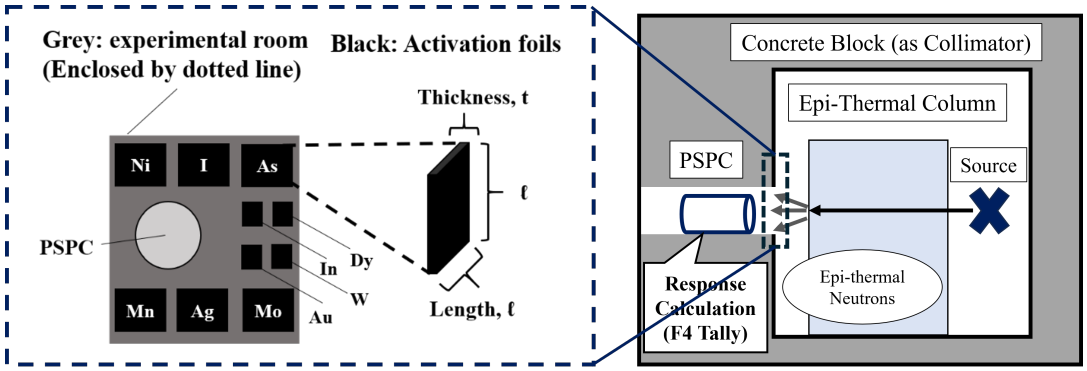


Figure 5.2: Simulation system in this Chapter. $\boldsymbol{R_{PSPC}}$ was prepared in the same approach as the one in the previous Chapter, and $\boldsymbol{R_{Foils}}$ was calculated in this material configuration.

5.3 Feasibility Analysis for the Simultaneous Use

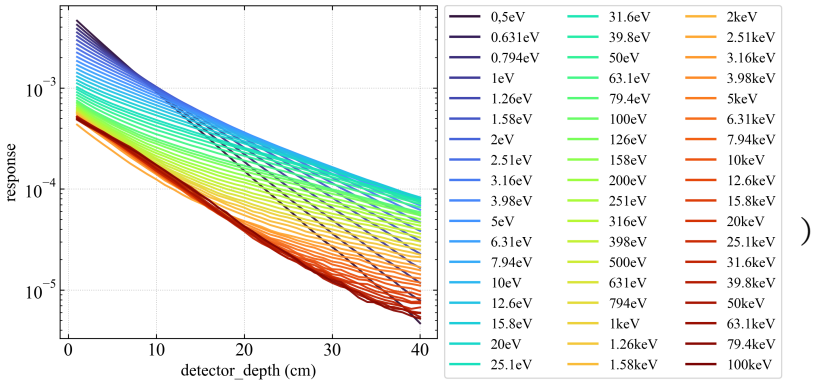
5.3.1 Evaluations of Response Function

Assuming the same experimental system as it was in Chapter 4, the response functions for PSPC and activation foils (named as $\boldsymbol{R_{PSPC}}$ and $\boldsymbol{R_{Foils}}$, respectively) was calculated in MCNP 5. Activation foils were placed in front of the hole where PSPC was deployed. A illustration of the simulation system was shown in Figure 5.2.

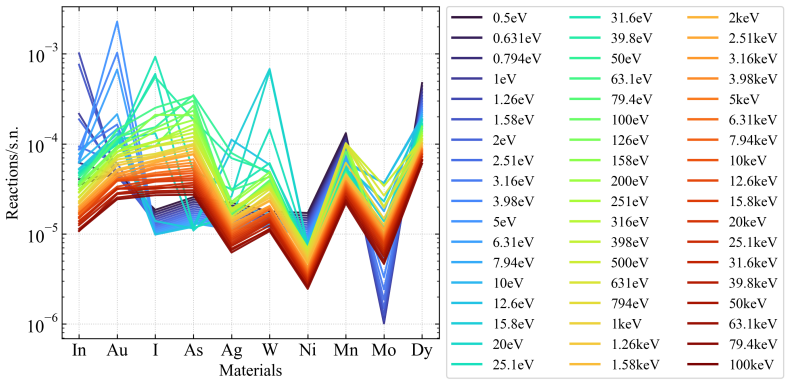
As we discussed in the previous Chapter, the response of PSPC was defined by the ^{3}He (n, p) reaction rate ($r_{i,j}$, See Equation 4.1), while the response of each foil through the (n, γ) reaction with the corresponding cross-section ($\sigma_{k,m}$), given in

$$\Sigma_{k,j} = A_i(E = E_j) \times L_w^2 \times L_t \tag{5.6}$$

Where "k" represents the material number ($1 \leq i \leq 10$), $\boldsymbol{A}$ is the (n, γ) activation rate calculated using the F4 tally in MCNP, L_w is the length, L_t is the thickness of the foils.



Response of PSPC ($\boldsymbol{R_{PSPC}}$)



Responses of Activation Foils ($\boldsymbol{R_{Foils}}$)

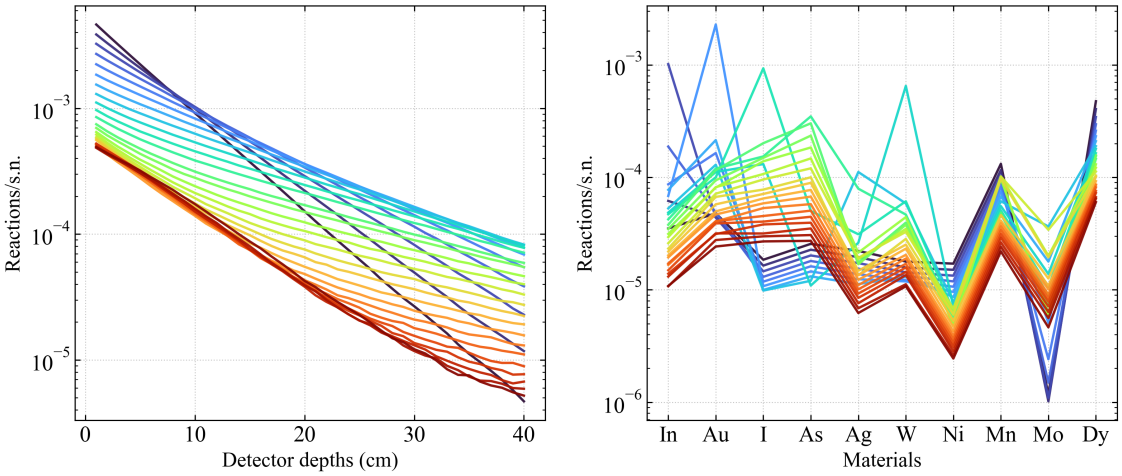


Figure 5.3: Response Function of this spectrometer ($\boldsymbol{R_{PSPC}}$ and $\boldsymbol{R_{Foils}}$), as the result of the response rate of ^{3}He (n, p) ^{3}H for PSPC and (n, γ) activation rates in each foil through MCNP simulations. Lower two figures show these responses with large energy intervals for better visuallization.

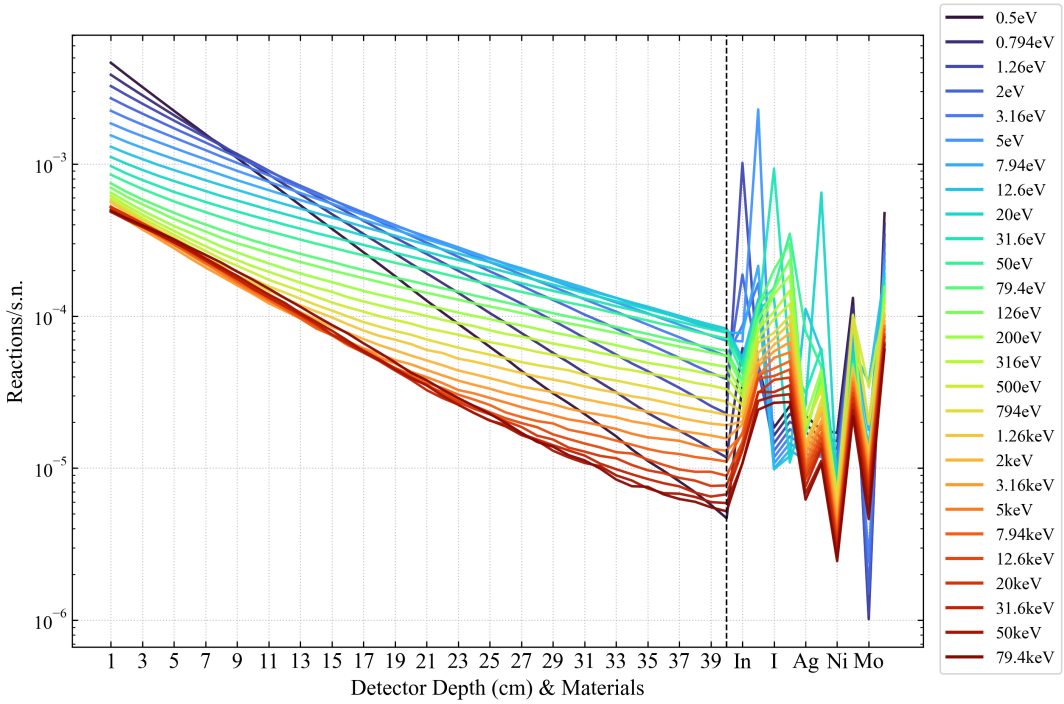


Figure 5.4: Response function of this spectrometer combined these two response ($\boldsymbol{R}^*$) shown in Figure 5.3.

By setting the atomic number and the MT number in the FM card of MCNP, MCNP can extract the activation cross-section from the nuclear data, and multiplied its atomic number to the track length, thereby activation rate is obtained.

Figures 5.3, 5.4 show the response function calculated in MCNP. The shape of R_{PSPC} indicates that the response decreases with the detector's depth, while R_{foils} exhibits a peak at specific energies corresponding to each material's activation cross-sections. Note, that the tally settings for the calculation of activation rates were introduced in **Appendix D**.

5.3.2 Numerical Analysis

As is in Section 4.3, numerical experiments were conducted by several candidates of $\boldsymbol{Z}$ (i) to estimate the energy spectrum in Equation (2.51) and compare with the reference spectrum listed below.

Z (1) : $\mathbf{Z} = \mathbf{R}^* \, \boldsymbol{\Phi}_{\boldsymbol{ref}}$

Z (2) : $\mathbf{Z} = \mathbf{R}^* \, \boldsymbol{\Phi}_{\boldsymbol{ref}} + \epsilon_1$ (1 %)

Z (3) : $\mathbf{Z} = \mathbf{R}^* \, \boldsymbol{\Phi}_{\boldsymbol{ref}} + \epsilon_2$ (3 %)

Z (4) : $\mathbf{Z} = \mathbf{R}^* \, \boldsymbol{\Phi}_{\boldsymbol{ref}} + \epsilon_3$ (5 %)

Z (5) : $\mathbf{Z} = \mathbf{R}^* \, \boldsymbol{\Phi}_{\boldsymbol{ref}} + \epsilon_4$ (10 %)

where ϵ represents the counting error, varying from 1 % to 10 %. $\mathbf{R}^*$ values calculated in **Section 5.3.1** were applied to this analysis. Note, that the iteration number was determined by "ideal-number" method for the $\boldsymbol{R^* \cdot \Phi_{ref} + \epsilon}(5\%)$, and the estimation performance was evaluated in its RMSE values.

The energy spectrum was deduced numerically using Equation (2.51), as shown in Figure 5.5. The "Simulation" label refers to the reference ($\boldsymbol{\Phi_{ref}}$), and the colored spectra represent the estimation values ($\boldsymbol{\Phi_{est}}$) from Z (1) – (4). The estimated spectrum generally agrees with the reference solution and reproduces the characteristic shape in Z (1) – (3). In case (4), larger discrepancies were observed between $\boldsymbol{\Phi_{ref}}$ and $\boldsymbol{\Phi_{est}}$ compared to other cases. However, $\boldsymbol{\Phi_{est}}$ values were significantly higher than $\boldsymbol{\Phi_{ref}}$ values for higher-energy neutrons.

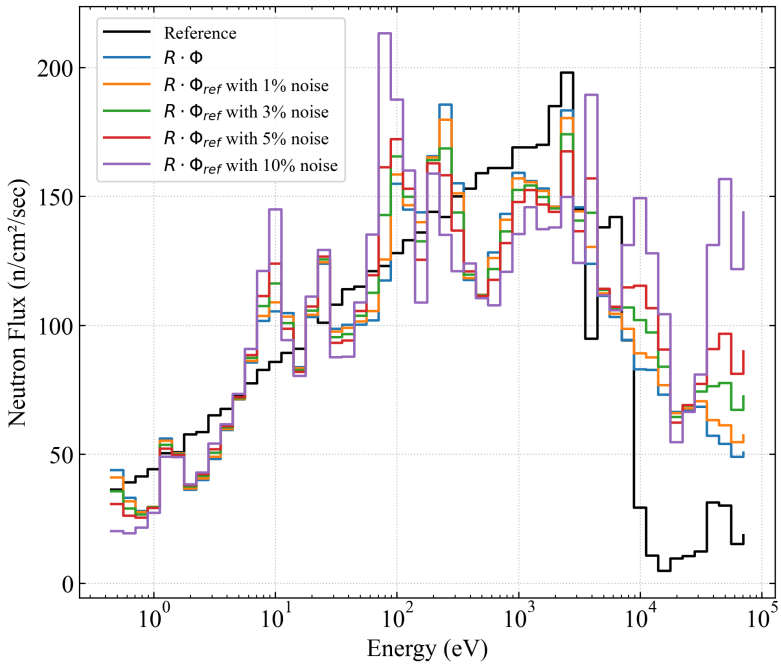


Figure 5.5: Comparison of $\boldsymbol{\Phi_{ref}}$ vs $\boldsymbol{\Phi_{est}}$ for each input value $\boldsymbol{Z}$.

Table 5.2: Iteration numbers and RMSE values in the sodium ratio

Input data ($\boldsymbol{Z} + \epsilon$)	RMSE value	NRMSE value (- 100 keV)	NRMSE value (- 10 keV)
None Error	28.6	0.41	0.22
$\epsilon = 1$ %	30.0	0.43	0.22
$\epsilon = 3$ %	33.7	0.48	0.25
$\epsilon = 5$ %	38.4	0.55	0.28
$\epsilon = 10$ %	53.6	0.76	0.39

Additionally, common peak-like features appear around 10 eV and 20 eV depicts the unfolded spectra, with the reference spectrum. In this energy region, contributions of activation foils were considered to be emerged. For instance, sharp fluctuations appear in the spectrum at the energies where Au, W, and I exhibit pronounced peaks in their activation cross-sections. Consequently, during the unfolding process, the estimated spectrum becomes increasingly influenced by these features as the iteration proceeds. Such effects must be appropriately addressed to obtain a more accurate and stable estimation.

In this case, the iteration number was determined to 7913 times, and RMSE & NRMSE values were shown in Table 5.2. While the iteration number was higher than that of tha case of only the PSPC instrumentation (See **Chapter 4**), the RMSE value was comparable despite the wider energy range for the evaluation. Although the RMSE was suppressed until measurement noise was 5 %, the RMSE of the unfolded spectrum increased almost twice when 10 % normal distribution was added as an uncertainty. This is because of the sharp reduction beyond 10 keV, and the NRMSE values by 10 keV indicates the equivalent estimation qualities compared to the results in previous Chapter.

The extent of the improvement can be demonstrated by first comparing the proposed method with the estimation obtained using only the PSPC system. Figure 5.6 presents the comparison between $\boldsymbol{\Phi_{ref}}$ and $\boldsymbol{\Phi_{est}}$, clearly showing a better agreement in the higher-energy region. The RMSE and NRMSE values were significantly reduced—from 58.2 to 28.6 and from 0.83 to 0.41, respectively. These results indicate that incorporating activation foils into the PSPC enhances the estimation quality owing to their energy-dependent cross-sectional sensitivities.

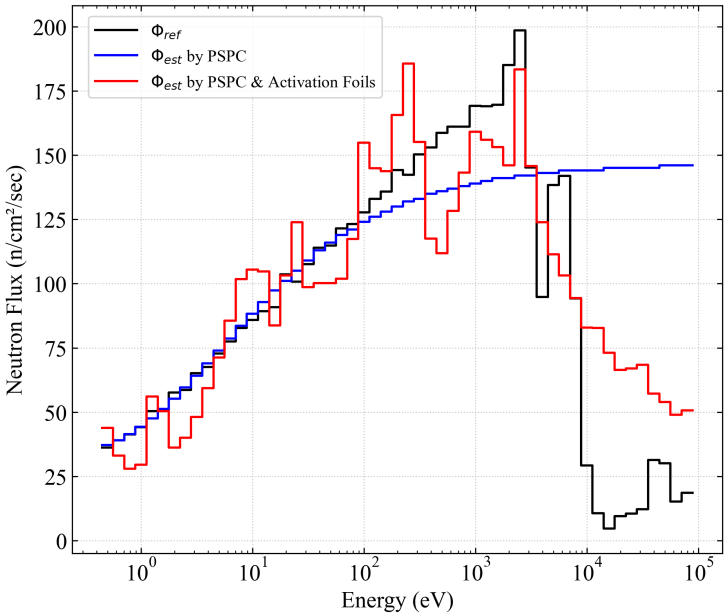


Figure 5.6: Comparison of $\boldsymbol{\Phi_{ref}}$ vs $\boldsymbol{\Phi_{est}}$ by only PSPC and mixture of PSPC and Activation foils.

5.4 Potential Application of This Approach

According to Figure 5.5, Numerical experiments indicated that the merged and calculated response function could unfold the energy spectrum from the input values that correspond to the experimental results. Notably, the estimated spectra showed good agreement with the reference spectrum, despite Equations (2.63, 5.3) being based on different physical laws, the former is based on protons by ^{3}He (n, p) ^{3}H reaction in PSPC, while equation (5.3) is based on activation reactions in various materials. Generally speaking, signals governed by different physical laws are not used for spectrum unfolding due to the drastic changes in the response function's shape (See Figure 5.4).

Nonetheless, the estimated spectra reproduced the reference spectrum well, likely because the number of measured data (length of $\boldsymbol{Z}$, 50 in this study) increased, and the absolute values in both detectors did not change significantly. This is because of the magnitude of the activation cross-section of each material. This result demonstrates that the experimental data can be converted simultaneously into the energy spectrum, even if it consists of signals produced by different physical phenomena.

Still, the estimated spectra might be affected by the activation foils, such as in around 10 eV and 20 eV. Therefore, the optimizations of materials selection, configuration and their dimension are necessary for more precise estimation. For example, cobalt, copper or gallium were often used as the activation foils in the epi-thermal energy ranges [42, 109], also, simultaneous use of the moderator such as boron or lithium was demonstrated to get the sensitivity in typical energy region [106]. In terms of the optimization process, several optimization algorithms have been utilized in this field, for instance, Yulin applied the Genetic algorithm for the moderator design of the neutron source in BNCT, called Beam Shaping Assembly [110]. This approach also is available for the design work of the activation foils. These approaches will be able to supplement the estimation performance with PSPC (this study), BSS, or others by using activation foils, as the same mechanism of resonance reactions.

5.5 Summary

In this Chapter, we proposed a novel spectrometer to measure the neutron energy spectrum in the range of 0.5 eV to 100 keV. Over the 10 keV neutrons are especially critical for patient dose during BNCT treatment. The proposed method combines a position-sensitive proportional counter with activation foils. While each technique has limitations in its measurable range, its integration allows coverage over a broader spectrum. By modeling the response of each detector and simulating signal distribution by the MC simulation, the energy spectrum was estimated and compared to a reference spectrum through the spectrum unfolding technique. Bayesian estimation was employed to solve the inverse problem, enabling spectrum derivation from any initial value. To account for experimental conditions, several normal distributions with errors were added to the counting values. The results

demonstrated good agreement between the estimated and reference values up to 10 keV. This indicates that incorporating activation foils improves spectrum unfolding performance, leading to a more accurate reproduction of the energy spectrum. Notably, the findings suggest that spectrum unfolding may be applicable when merging different physical measurements. However, the estimated values did not replicate the sharp decrease in the spectrum above 10 keV. RMSE analysis confirmed that this approach effectively measures the neutron energy spectrum in the epi-thermal range with high robustness. **Section 5.4** introduces the possibility of this approach to improve the estimation performance more, and suggested that the precise estimation of the energy spectrum will be achieved by optimizing the material selection and these configuration.

Through these discussion, we concluded that the proposed approach combining different detectors is valid, even if each of them detects neutrons in different mechanisms. However, since multiple foils need to be implemented for the precise estimation, it requires several experiments to obtain the signals from activation reactions in reality. Also, though PSPC can estimate the energy spectrum in one time irradiation, it is desirable for PSPC to obtain to get more precise results, as discussed in **Chapters 3, 4**. To cope with this issue, we proposed another novel spectrometer which is able to measure this parameter not only in the small size, but also with a high accuracy. In the following Section, I introduce the methodology and the validity of this spectrometer.

6 Instrumentation of Imaging Plate for Neutron Spectrometry

6.1 Introduction

This chapter presents the methodology and estimation results of another novel spectrometer, which utilizes the Imaging Plate Neutron Detector (IP-ND), as discussed in **Section 2.2.4**. The basic concept is that the energy spectrum is derived from the neutron spatial distribution measured in an IP-ND. For the high-neutron spectroscopy, Nohtomi et al. developed a unique approach which the acryl cone was installed in front of the BAS-TR to moderate neutrons and also to measure a spatial distribution corresponding to the neutron energy there [73].

This study also suggests a novel type of spectrometer for epi-thermal neutrons using IP-ND. Details were introduced in **Section 6.2** Since the measured data in IP is generated as a relative value (PSL scale), the neutron intensity should be monitored. During these processes, we aim to extract the neutron's intensity distribution from the spatial distribution in IP, and the energy spectrum is derived from that distribution.

Since **Section 2.2.4** focused on the detection system of the imaging plate (IP), including versions designed for photon detection, this chapter begins by describing the fundamental physics of IP-ND, as presented in **Section 6.2**. Building on this foundation, we then develop the discussion toward the spectrometer system, followed by a summary of the experimental and simulation methodologies and their corresponding results.

6.2 Detector Configuration

Figure 6.1 shows the spectrometer design; the moderator (boron was listed as an example) was installed on the imaging plate, and the signals are extracted by ^{157}Gd (n, γ) ^{158}Gd reactions. Theoretically, the effective absorption cross-section is changed by incorporating boron absorber with different thicknesses, and thanks to its 1:1 correspondence of boron in epi-thermal range (See Figure 6.2), neutron's energy is reduced in a constant ratio. Therefore, PSL value in each pixel includes the contribution of neutrons in a certain range of energy. By preparing several thicknesses of the moderator, we can reproduce the energy distribution of the epi-thermal neutron field with the IP's spatial distribution. Besides, this system allows us to evaluate the energy spectrum only in one-time irradiation experiment, unlike the BSS or multiple activation foils method.

We applied the spatial distribution ($\boldsymbol{N}$) for the unfolding Equation (2.23), as follows

$$\frac{dN}{d\Phi} = \int R(\Phi, E)\Phi(E)dE \tag{6.1}$$

$$N_i = \Sigma_j R_{i,j} \times \Phi_j \tag{6.2}$$

Where N_i is the neutron intensity derived from the recorded PSL intensity in the ith position interval, R_{ij} is the response matrix coupling the ith position interval with the j th energy interval and Φ_j is the neutron flux in the j th neutron energy interval. Since neutrons' contributions are measured from ^{157}Gd (n, γ) ^{158}Gd reactions, N_i should be proportional to their energy deposition [111], and this incident can be evaluated through Monte Carlo simulations (details are written in **Section 6.3.2**).

Here are other motivations for developing this spectrometer.

- **Downsizing the spectrometer**: Conventional spectrometers, BSS or PSPC, need to be covered by moderators such as polyethylene, and the size is relatively large (BSS requires at least 15 cm Φ sphere type of moderators, PSPC does $50 \times 50 \times 50$ cm^2 according to Ref [52].) On the other hand, boron used in this spectrometer has a large absorption cross-section in the thermal neutrons (3880 barn); thus, it doesn't require any large moderator systems. This study cuts an IP-ND into 10×12.5 cm to measure the spatial distribution (See Figure 6.3) When it comes to the utilization of the spectrometer in the hospital, this compactness reduces the human's effort.

- **Possibility of high energy sensitivity over the epi-thermal range**: Owing to its high spatial resolution, the IP enables the detector plane to be subdivided into a large number of meshes. This feature allows the IP-ND system to recover neutron-energy information over a wide dynamic range by placing multiple thin moderators within a compact geometry and analyzing the resulting spatial distribution. In contrast, the sensitivity of conventional BSS or activation-foil methods is constrained by the limited number of moderators or available materials. This lack of sensitivity is a major challenge in evaluating epi-thermal neutron spectra, and the IP-ND equipped with numerous moderators has the potential to overcome this limitation.

- **Flexibility to customize the moderator composition**: The spatial distribution measured with the IP depends on the types and thicknesses of the inserted materials, which can be easily investigated by designing and placing them directly on the IP surface. In contrast, moderators used in other spectrometers are generally large and structurally complex, making such flexibility difficult to achieve. This design freedom is therefore a significant advantage of the IP-ND system.

- **Availability of the passive measurements**: Nowadays, the neutron spectrometer using the liquid-based moderator to change its sensitivity has been developed [45, 90]. This approach enables us to evaluate the energy spectrum in only one-time irradiation; however, it also takes time and effort to change the volume of the liquid by hand. Our proposed spectrometer can evaluate the energy spectrum just by placing it onto the epi-thermal neutron field.

In order to confirm the feasibility of this system, we performed the irradiation experiment, as described in the following Section.

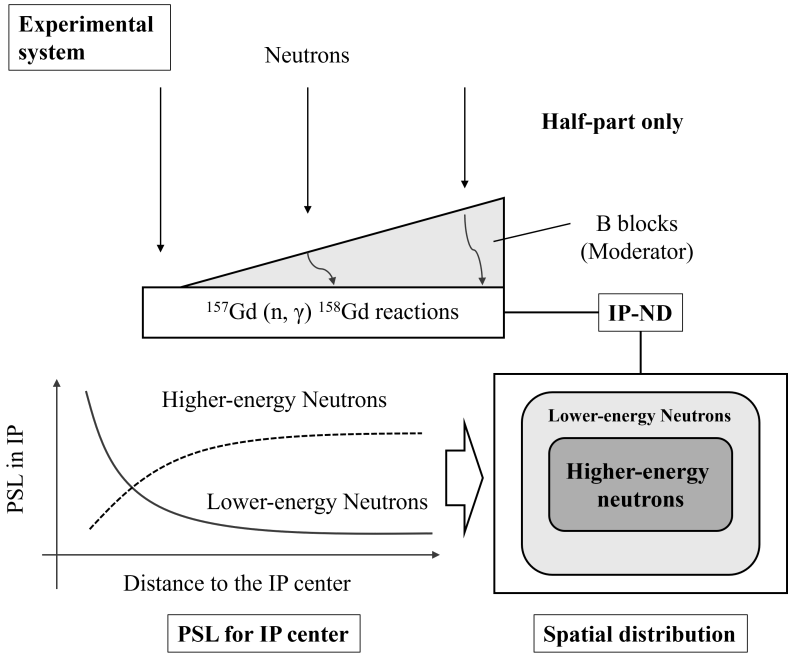


Figure 6.1: Schematic representation of the evaluation principle for neutron energy using an imaging plate with 10B blocks (half are shown here). By installing several thicknesses of the moderator (Ex. Pyramid style in this figure), the spatial distribution was represented with the neutron's energy information ($\boldsymbol{N}$). It is converted to the energy spectrum in the spectrum unfolding method (See **Section 2.3**)

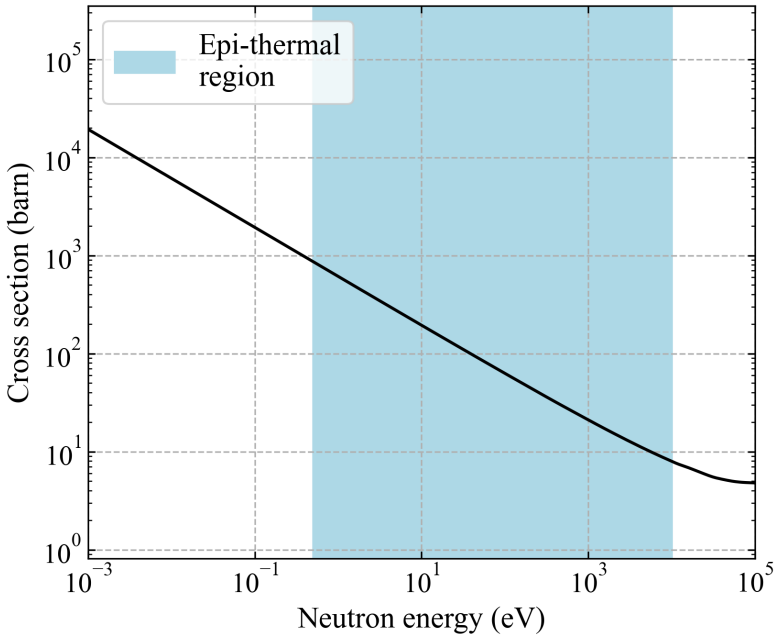


Figure 6.2: Neutron absorption cross-section in boron [64]. It adheres to 1/v law and 1:1 correspondence is valid in epi-thermal region.

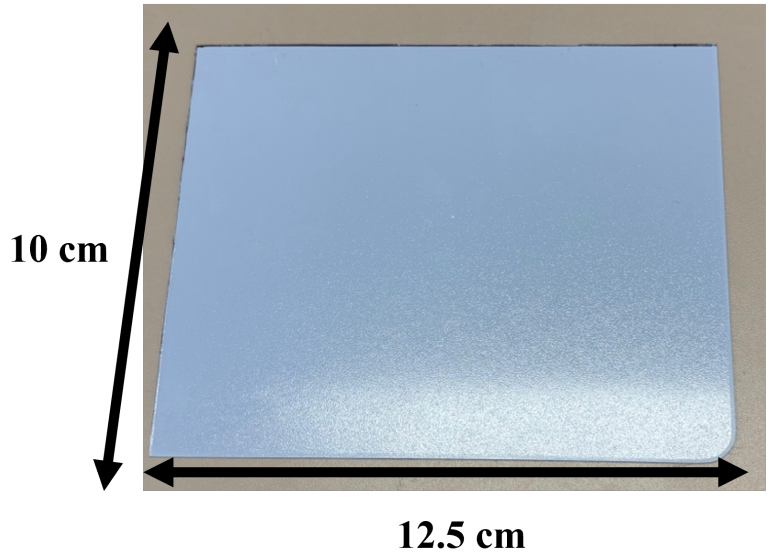


Figure 6.3: The picture of the IP-ND used in this study.

6.3 Data Acquisition Approach

6.3.1 Experimental Data Processing

In order to verify that the IP response corresponds to the neutron energy, we carried out validation experiments in an epi-thermal neutron field, KUR Heavy Water Neutron Irradiation Facility [112]. This system has a peak at lower part of the epi-thermal range (between 1 eV and 10 eV), as shown in Figure 6.4.

After irradiation, the PSL intensities were extracted and analyzed using an image scanner (BAS-1800, Fuji Film Co., Ltd.). The wavelength of the laser was 625 nm, and the pixel size was set as 200 µm. A PSL value in each pixel has a 16-bit gradation of grayscale. Also, the gray values were saved as "tiff" file, then were processed by "tifffile" module in Python. By selecting Region of Interest (ROI), we extracted the average PSL, Gray value in that region. As for the error propagation, we also extracted the standard deviation from the "tiff" file, thereby the standard error in the Pixel value (ϵ_{ROI}) was obtained from the following Equation:

$$\epsilon_{ROI} = \epsilon_{PSL} = \frac{Std_{ROI}}{\sqrt{ROI}} \tag{6.3}$$

Where $\sqrt{ROI}$ is the pixel numbers of the ROI. As introduced in this Equation, we assume that the standard error of PSL value also contributes to the PSL value (defined as ϵ_{PSL}).

However, we should consider other uncertainties in readout process. For instance, the experimental result in IP depends on the conditions of each experiment. According to the BAS-1800 manual, the shading correction in the readout process can introduce uncertainties of at least 5%. In addition, the fading effect must be

considered as another reason for variation in the PSL values, even when the same measurement conditions are repeated across different experiments [48].

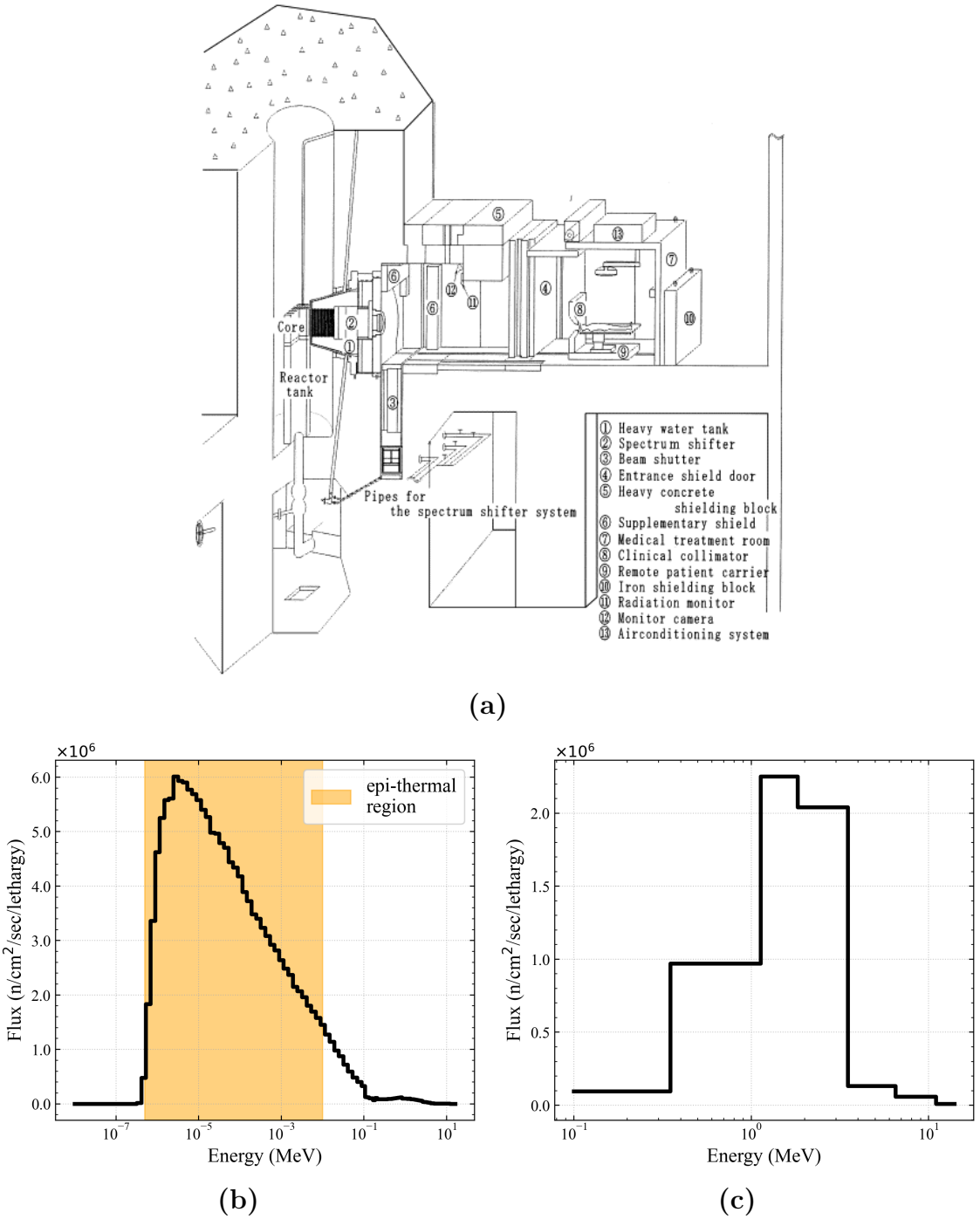


Figure 6.4: (a) A picture of the experimental room, picture was extracted from [112], (b) Reference spectrum of neutrons and (c) γ-rays in KUR-KWHIF.

It is important to mention that the experimental results from IP are relative, not corresponding to neutron intensity directly. To correct this, a gold foil was implemented to obtain the neutron intensity using Equation (6.4), which is the same as Equation (2.17), N_a was replaced by I, and C was also replaced by $\frac{A}{\lambda}$.

$$I = \frac{A}{\lambda} \cdot \frac{1}{f_s \cdot f_g \cdot \varepsilon_{ff} \cdot I_\gamma \cdot [\exp(-\lambda t_c)][1 - \exp(-\lambda t_m)]} \tag{6.4}$$

Where A means the radioactivity, I_γ is the emission ratio of γ rays from ^{197}Au (n, γ) ^{198}Au reaction (95.6 % in this study), f_s, f_g are the coefficient of the self-shielding effect and absorption probability of γ-rays inside the foil, ε_{ff} is detection efficiency (6.46 % in this study), t_c is time required to bring the Au foil to the HPGe detector from the experimental room, and t_m is the measurement time in HPGe detector. 411 keV γ-rays emitted through neutron irradiation are measured in the HP-Ge detector. In principle, the measured I includes the error from C, t_c, t_m, f_g, and ε_{ff}. however, since the decay constant of Au is extremely small (2.98×10^{-6} (1/sec)), the error in the count rate is dominant. We also performed the error propagation by processing the error in the count rate.

PSL values are measured relatively based on the maximum value, which differs in each experiment. Considering the secondary particles generation through the activation process in ^{197}Au, the PSL value in this region is the maximum. Therefore, the PSL values can be normalized uniformly, given in the following Equation (6.5)

$$PSL^{(i)}Corr(x) = PSL^{(i)}(x) \times \frac{PSL^{(1)}(\mathrm{Au})/I^{(1)}}{PSL^{(i)}(\mathrm{Au})/I^{(i)}} \tag{6.5}$$

Where $PSL^{(i)}Corr(x)$ is the corrected PSL values at position x from the initial PSL values $PSL^{(i)}(x)$ in this process, $PSL^{(i)}$ (Au) is the PSL values, $I^{(i)}$ (Au) is the neutron intensity from the Au foil in i th experiment (i = 1-4). In this study, PSL values were corrected based on the Experiment 1. During this procedure, the behavior of neutrons emitted from KUR is assumed to be influenced solely by the surrounding system. Consequently, neutron intensity is constant through the experiment, and the differences in the neutron frequency detected by the Au foils, that is, the differences in radioactivity, are attributed only to their positions.

We assumed that the radioactivity obtained by the experiment was to be accurate, and then the neutron flux was obtained from the PHITS simulation results of the activation rate, See the following Section. Notably, we employed two types of Au foils, with/without Cd sheet surrounding them. This is because we can understand whether the irradiation field is dominant to the epi-thermal or not by calculating the ratio of their radioactivity, written in

$$Cd\ ratio = (A_{\mathrm{Au}}/M_{\mathrm{Au}})\ /\ (A_{\mathrm{Au+Cd}}/M_{\mathrm{Au+Cd}}) \tag{6.6}$$

Where A_{Au}, A_{Au+Cd} are the radioactivity in each foil measured in HP-Ge detector, M_{Au}, M_{Au+Cd} are their masses. Originally, due to the extremely high absorption cross-section of Cd for thermal neutrons, the Au with Cd foil measures the contribution to neutrons over the epi-thermal range, while the Au without Cd foil measures

them including thermal neutrons. If Cd ratio is close to 1, this means the contribution from thermal neutrons is almost shielded by moderators in KUR-HWNIF, and then this neutron field can be defined as "epi-thermal."

6.3.2 Simulation strategy

In order to reproduce the IP-ND's response, PHITS Ver 3.35 was employed to reproduce the behavior happening in IP-ND [95]. This version uses EGS5 for the transport of electrons, positrons, and photons [113].

Figure 6.5 shows the brief illustration about the mechanism of the IP's neutron detection and the simulation strategy in this study. Based on the fundamental processes occurring in IP-ND discussed in **Section 2.2.4**, Hidding et al., proposed that the PSL value corresponds to the energy deposition in the phosphor region of IP [111]. Thus, the following Equation is valid:

$$PSL \propto a \cdot E_{dep} \tag{6.7}$$

Where "a" is the coefficient, and E_{dep} is the energy deposition to the IP. In this study, several additional contributions must be considered aside from the photons generated by ^{157}Gd (n, γ)^{158}Gd reactions:

- Background photons originating from KUR inherently accompanying the neutron field
- γ-rays generated by Cd (n, γ) reactions
- ^{10}B (n, α)^{7}Li reaction in Boron blocks used as moderators

They are non-negligible to evaluate the energy deposition to the IP. In PHITS, the total energy deposition is evaluated using the [T-deposit] tally. By defining an event counter that records only the occurrences of the ^{157}Gd(n, γ)^{158}Gd in the [counter] section, it becomes possible to isolate and quantify the energy-deposition component originating solely from Gadolinium (defined as E_{dep} (Gd)) [114]. Moreover, we need to assess the performance of the gold foils, which were utilized to obtain the neutron intensity. The response rate of ^{197}Au (n,γ) ^{198}Au ($1/cm^3/sec/s.n.$) can be obtained by calculating the track length of neutrons and then multiplying its activation cross-section and atomic number in [multiplier] section within the PHITS input. The neutron intensity (I) was also derived from this calculated response (R)

$$I = R \cdot \Phi_{ref} \cdot S \cdot t \tag{6.8}$$

Where Φ_{ref} is the reference spectrum in KUR [112], S is the source area, and t is the irradiation time (2 mins in this study). A cross-check of the experimental neutron intensity can be assessed by comparing Φ values from Equations (6.4) and Equation (6.8).

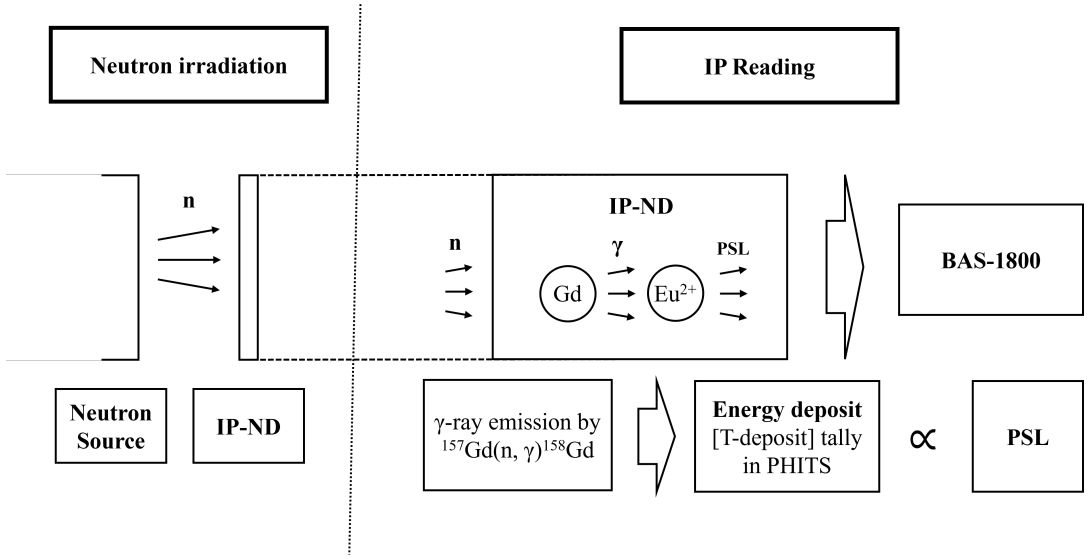


Figure 6.5: Illustrations of the PHITS simulation strategy. We considered that the energy deposited to the phosphor region of IP-ND relates to the PSL value, and both relative values were compared for benchmarking.

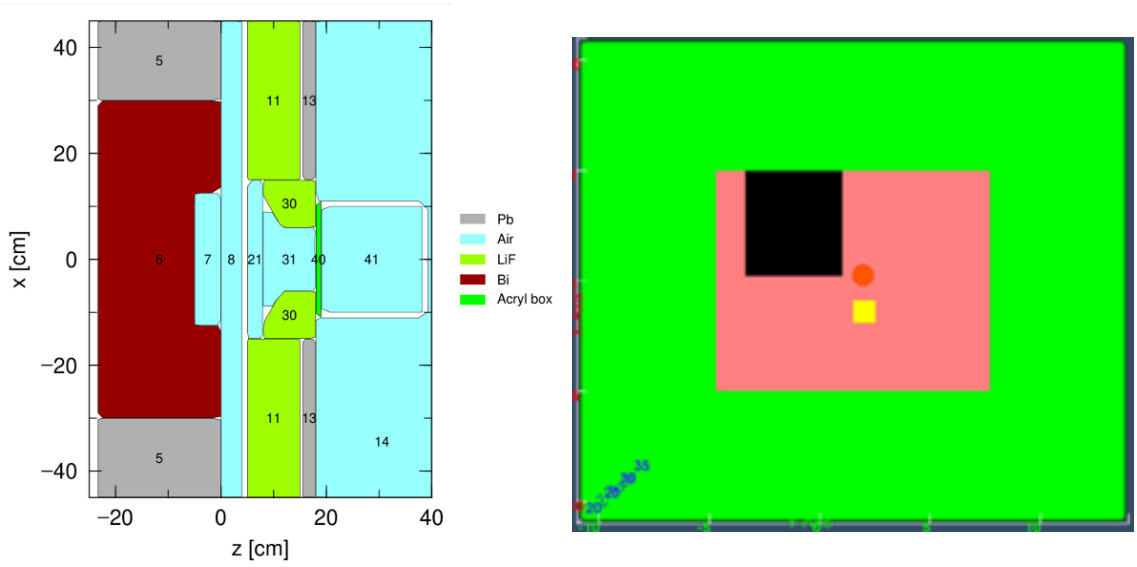
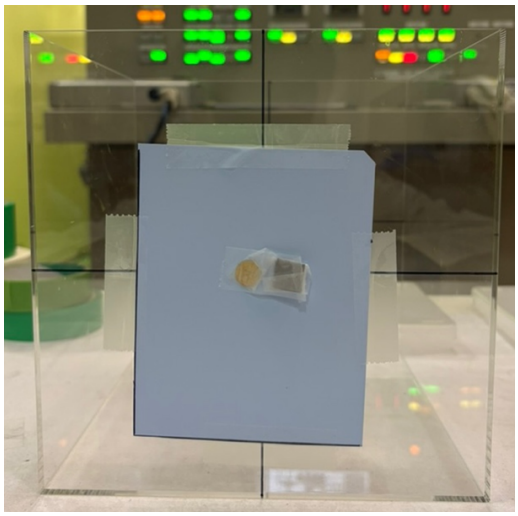


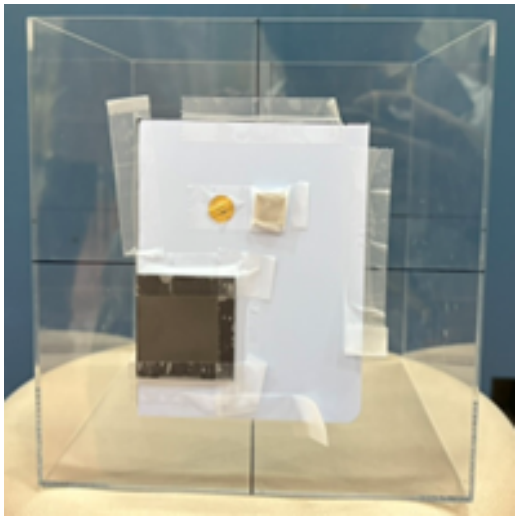
Figure 6.6: PHITS geometry modeling the experimental system (left: KUR source system, right: IP with a boron block, Au foils) Black region is for boron, orange is an Au foil, and yellow is cadmium. The left illustration was the result from T-track tally in PHITS with icntl = 8 version. The right one was from PHIG-3D.

The simulation geometry was depicted in Figure 6.6. IP-ND's structure was also modelled accurately (10 - 12.5 cm), namely a phosphor region and others were designed according to the Figure 2.5. The ferrite region consisted of the Fe_2O_3, which is often used as the ferrite material [115]. As for the source settings, the

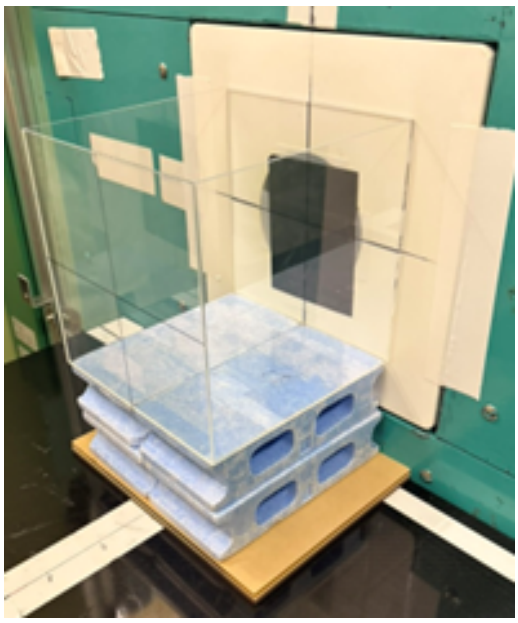
position was referred in [116], and the mixed-field of neutrons and γ-rays with the spectrum illustrated in Figure 6.4 were utilized in PHITS. In tally settings, we separated 5×5 mm in each mesh because the scattering effect can be suppressed within 5 mm, as a result of the preliminary experiments.



(a): IP Without any boron filters



(b) IP With ^{10}B, B_4C filters



(c): Acryl box and Styrofoam



(d) Light-shelding curtain

Figure 6.7: Experimental systems, (a), (b): IP with/without boron filters. Au foils were placed to measure the absolute intensity of this neutron field. A Cadmium sheet was covered with to confirm the epi-thermal neutrons' contribution. (c): These materials were stuck onto an acrylic box, and Styrofoam was used to adjust its position. (d): A light-shielding curtain was employed not to prevent PSL measurement.

Table 6.1: Radioactivity of Au foils and Au + Cd foils to determine the Cd ratio.

Experiment number	Au only		Au + Cd		CF ratio
	Mass(g)	A	Mass (g)	A	
#1	0.100	703.17 ± 5.56	0.099	600.39 ± 4.38	1.15
#2	0.100	692.65 ± 6.72	0.100	655.70 ± 6.75	1.05
#3	0.099	625.81 ± 5.88	0.100	599.18 ± 5.75	1.06
#4	0.100	639.43 ± 6.72	0.191	612.43 ± 4.77	1.13

Table 6.2: Comparison to neutron fluxes with the reference value [112]. The unit is $10^8\,\mathrm{cm}^{-2}\,\mathrm{s}^{-1}$.

Reference [112]	Experiment 1	Experiment 2	Experiment 3	Experiment 4
1.61	1.93 ± 0.02	1.99 ± 0.02	1.96 ± 0.02	2.05 ± 0.02

6.4 Benchmark Experiment

6.4.1 Experimental Set Up and Its Result

Benchmarking experiment was performed in two experimental systems (See Figure 6.7). Gold foils (with/without cd foil, to cut off the contribution of thermal neutrons) were placed on the IP-ND to obtain absolute intensity. IP-ND with these foils were stuck onto an acrylic box, adjusting position by Styrofoam, and light-shielding curtain was covered in the surrounding region. We prepared the boron blocks (B_4C and ^{10}B (100%), thickness varies from 2 mm, 3 mm, and 5 mm), as shown in case 2 to moderate neutrons. Exposure to the mixed-field of neutrons and γ-rays was taken in 2 minutes, and then the PSL value and the neutron intensity were measured.

Results of the neutron intensity and the mean values at several regions are presented in Tables 6.1 and 6.2, and Figure 6.8. Firstly, the radioactivity values of Au foils and Au with Cd foils were exhibited in Table 6.1, which indicates that the Cd ratio varies around 1.1 so that we regarded that this experiment has been carried out under the epi-thermal neutron field. The neutron flux analysis is summarized in Table 6.2, showing values approximately 25% higher than the reference. However, according to the reevaluation project reported in Ref. [116], the epi-thermal neutron flux under the 5 MW operation was found to be higher than the previously

published Ref. [112]. Therefore, the present values are considered reasonable, and this result can be used to monitor the neutron flux reaching the IP.

Figure 6.8 shows the spatial distribution of pixel value, read by BAS-1800. Herein, results of the experiment 1 and 4 were depicted and compared for instance. There were variations in the pixel values, due to the neutron distribution and the moderator placements. First, the highest pixel values were found at the bare Au foils locations, which is considered the contributions of the β^- decay from the ^{198}Au nuclei. Details were discussed in the Following Section with the simulation results of PHITS. Also, the pixel values at the Au foils covered by cadmium were smaller than other regions, which came from the high-absorption cross-section of cadmium, as well as the β^- decay from the ^{198}Au nuclei. The influence from boron filter can be clearly observed in the right figure, the low pixel values where boron was placed. Other blue-colored region was attributed not to neutrons, seemed background photons produced in the source at the same time. In addition, the pixel values in the region where the IP-ND was secured with tape were markedly higher due to its interaction with neutrons.

To investigate the spread of the epi-thermal neutron beam from KUR in more detail, PSL profile analyses were performed for the rectangular regions shown in the right-hand figure. This analysis is also essential for evaluating the scattering effects on the IP-ND introduced by the moderators.

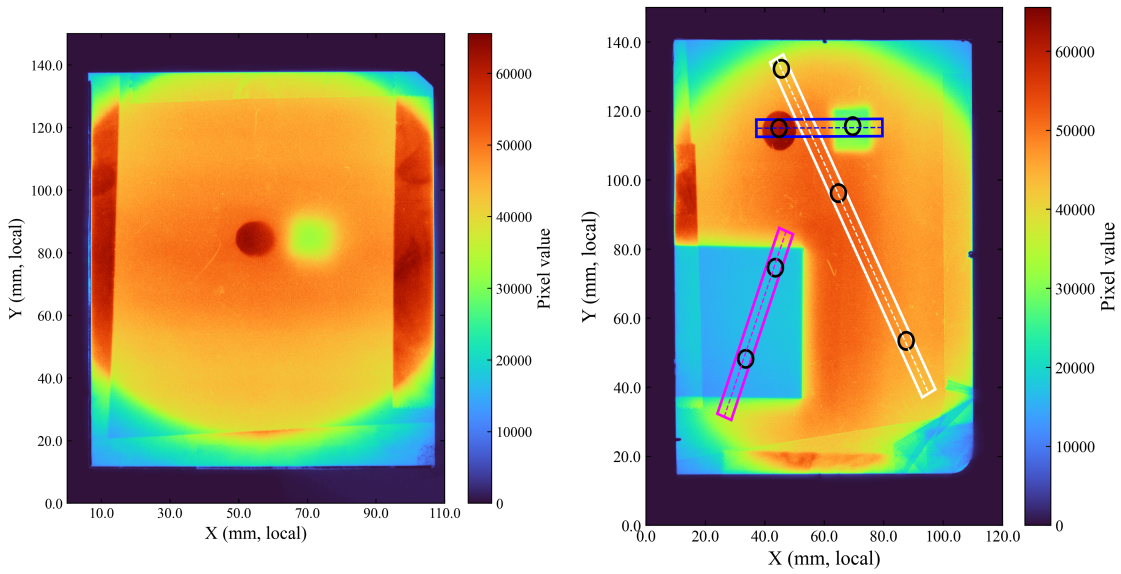


Figure 6.8: Illustration of the pixel values in experimental systems (left: Without any boron blocks, right: With a boron block). PSL profiles were analyzed in the rectangle regions, and also the mean pixel values and PSL values were investigated in the black circle regions (each circle has 5 mm ϕ, and selected to investigate both parameters in the positonal conditions).

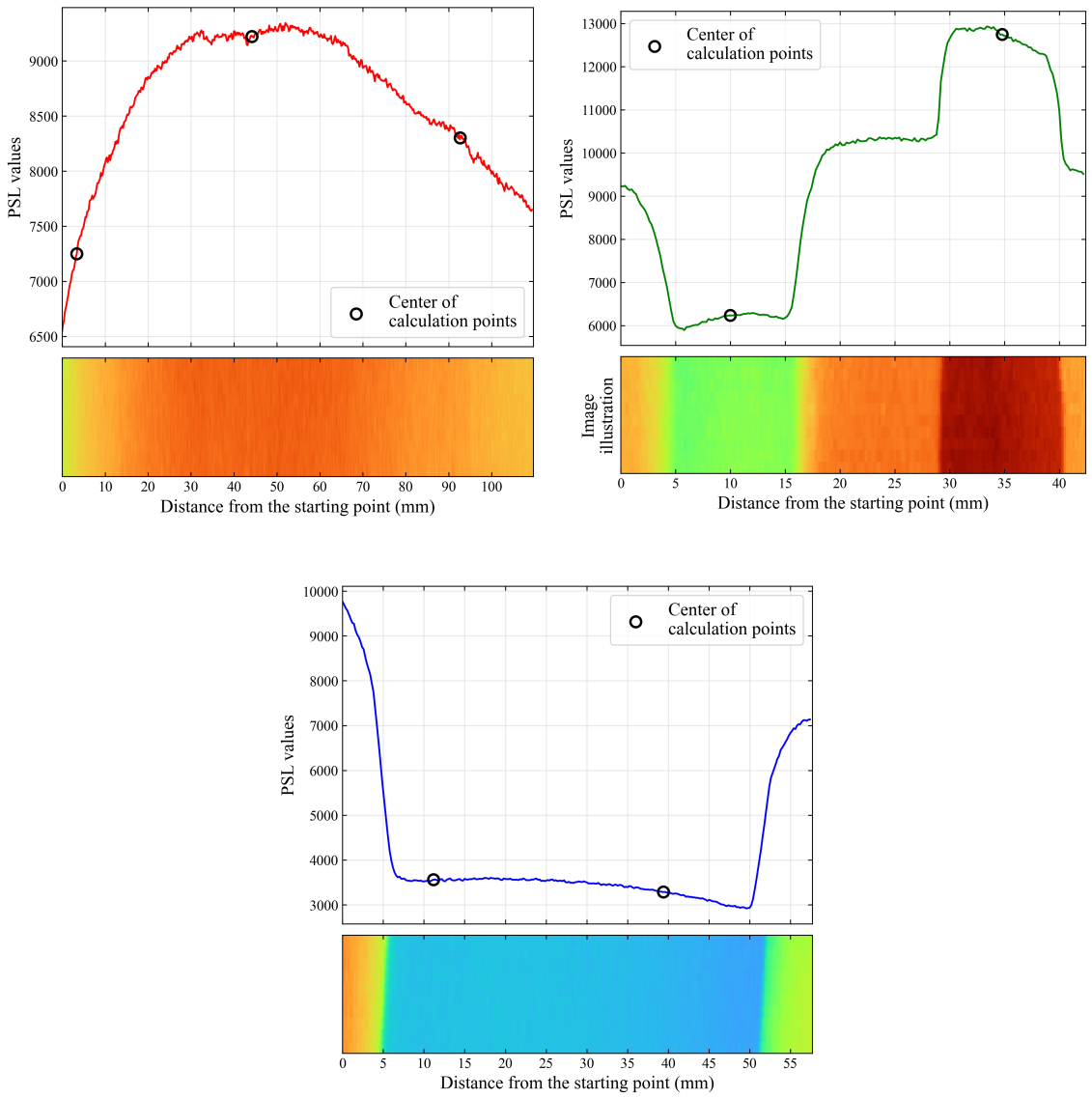


Figure 6.9: Illustration of the IP profile in each rectangle region (top: white, middle: blue, bottom: pink). graphical figures followed by the profile data are color maps of the PSL value in these regions.

As shown in Figure 6.9, we evaluated the "bare region" (white), "foil region" (blue), and "boron region" (pink). The results indicate that the PSL values vary with position in accordance with the local neutron fluence. Sharp increases and decreases in PSL values were observed at the boundaries of the moderator materials; however, the affected width was small—no more than approximately 5 mm. Therefore, these experimental results confirm that the PSL distribution maintains high spatial resolution even when multiple moderators are placed on the IP.

As several points were illustrated in Figure 6.8, we selected several points in each result and mean PSL values ($1/mm^2$) and corresponding mean pixel values

$(1/mm^2)$ were compared after the correction process by Equation (6.5). Figure 6.10 shows the result of this process, indicating that a clear linearity was observed. As for the moderating effect of boron, the PSL values were found to be nearly identical. This preliminary experiment indicates that a 1-mm boron layer is sufficient to stop most neutrons under the KUR irradiation conditions. Also, it revealed that thinner boron blocks are required to distinguish epi-thermal neutrons and reproduce their energy information with the IP.

6.4.2 Calibration from PSL Value to Neutron Intensity

For the benchmarking, we investigated the relationship between the PSL value of the irradiation result and the energy deposition calculated in PHITS. The mean PSL values and the mean value of E_{dep} at the selected regions in the previous Section were compared. The comparison between the experimental result modified data in mm scale and the spatial distribution of the E_{dep} is illustrated in Figure 6.11, which indicates the linearity is valid. Furthermore, a spatial distribution of E_{dep} (Gd) values was also calculated and the relationship for the PSL values was depicted in Figure 6.12. This result suggests linearity, and the y-intercept means the contributions γ-rays from the neutron source to PSL, and it should be almost constant. Therefore, PSL values over the y-intercept can directly reproduce the neutron' s contribution.

Furthermore, the highest PSL at the location the Au foil was positioned was revealed to come from the radioactivity of the daughter nuclide, ^{198}Au. Using the source function in PHITS which can set RI source, the energy deposition was calculated in [T-deposit] tally (See Figure 6.13). Results clearly indicate their high contributions to IP' s response, even if it was covered by 6 μm PET layer.

Therefore, simulation works above were found to be able to reproduce the IP-ND' s response, and we propose the spatial distribution about the number of neutrons counted in the IP can be estimated from PHITS simulations, as the process was shown below.

Firstly, PSL values are converted to neutron' s count rate from the Au foils experiment. Since the position where the Au foil is located is influenced by its radioactivity,

$$c = \frac{\phi_n St}{\text{PSL at Au foils}} \tag{6.9}$$

$$N = c \cdot PSL(neutrons) \tag{6.10}$$

Where PSL(neutrons) is the PSL in the neutron' s contribution. Let "a" , "b" be the constant of proportionality and y-intercept (4.8×10^8, 1028.1, respectively in this study), PSL(neutrons) and N are derived from the following Equations.

$$PSL(neutrons) = a \cdot E_{dep}(Gd) - b \tag{6.11}$$

$$N = c \cdot PSL(neutrons) = c \cdot (a \cdot E_{dep}(Gd) - b) \tag{6.12}$$

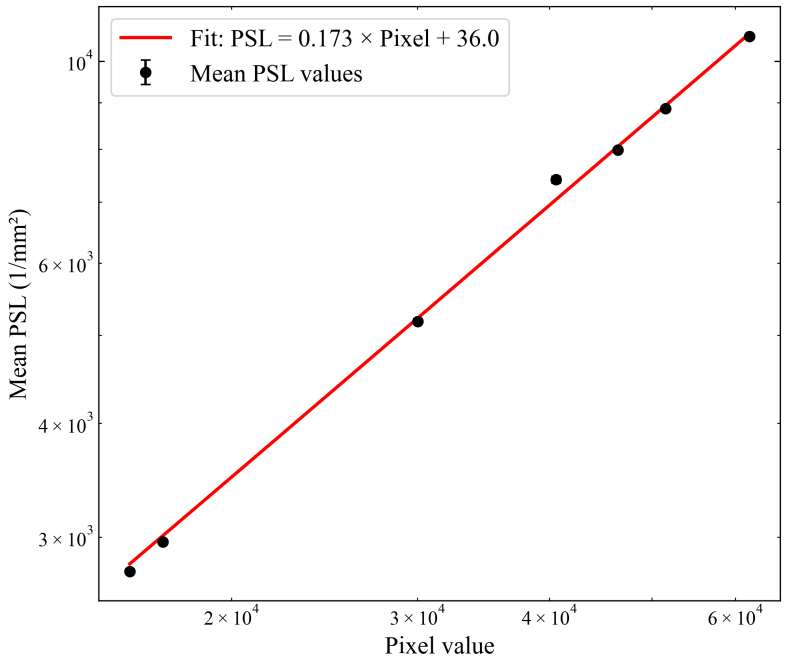


Figure 6.10: Correlation between pixel value and PSL value extracted in BAS-1800.

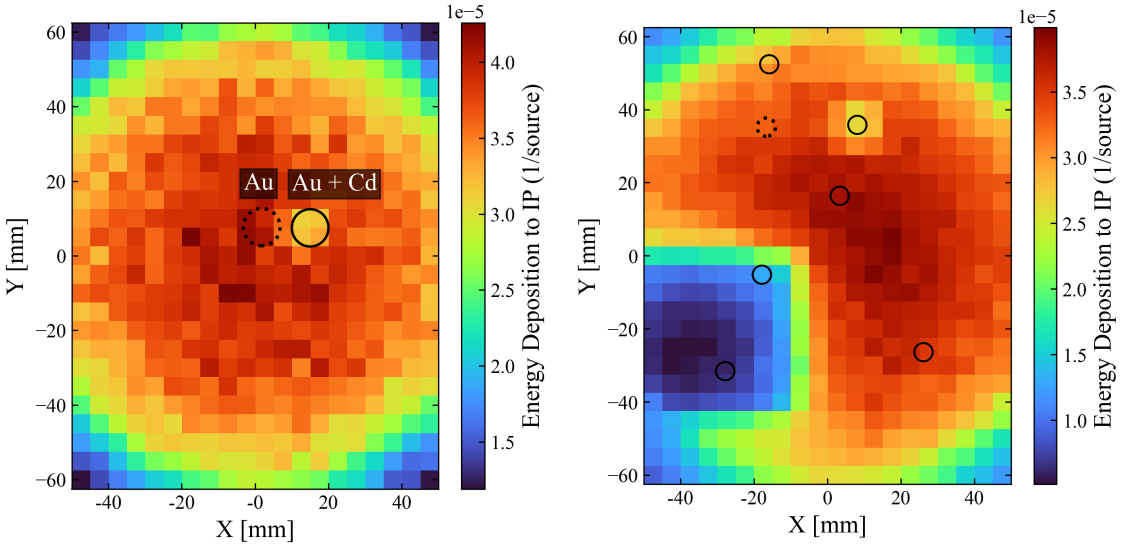


Figure 6.11: Results of the energy deposition calculated in [T-deposit] tally of PHITS. The left shows the result of Experiment #1, while the right shows #4.

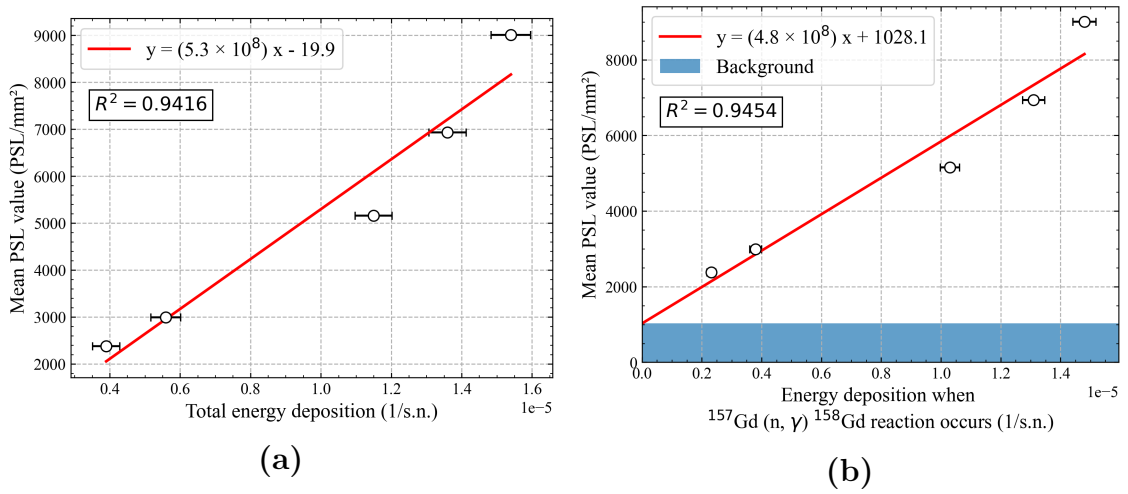


Figure 6.12: Correlation between the mean PSL values extracted in BAS-1800 and the (a) total energy deposition (b) when ^{157}Gd (n, γ)^{158}Gd reaction occurs to the IP-ND.

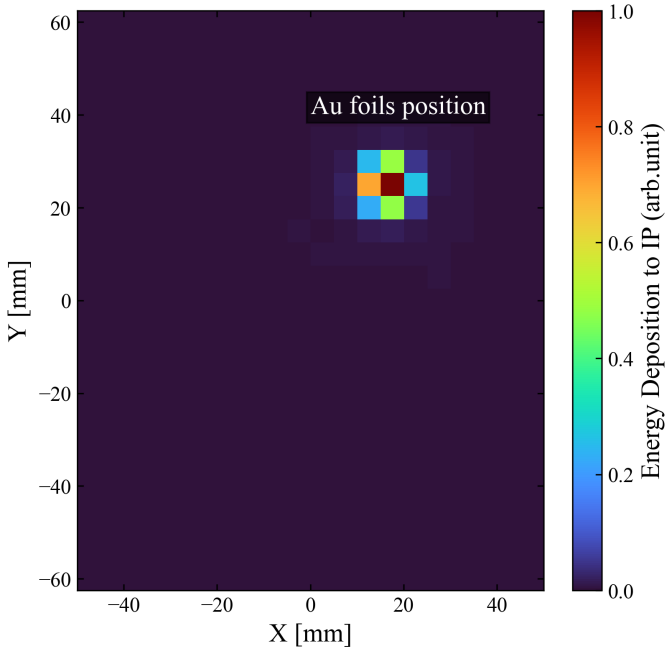


Figure 6.13: Energy deposition to the IP-ND from radioactivity source of ^{198}Au Radioisotopes. The colored region shows where the Au foil was located.

6.5 Feasibility of IP-Based Neutron Spectrometer

According to the PSL profiles analysis, the experimental results demonstrated that clear contrasts appeared in the PSL distribution depending on the positional condition and whether the moderator was assigned. The variations observed within a single imaging plate demonstrate that the IP-ND is sufficiently sensitive to the epi-thermal neutron field in the BNCT irradiation environment. In BNCT treatments, neutron fluxes are generally high to ensure adequate treatment quality [40]. Such high intensities may lead to several issues in radiation detection, for instance, it might cause pulse pile-up in gaseous detectors. On the other hand, it might be difficult to distinguish spatial variations in the neutron contribution on the IP because excessive neutron fluence enhances the ^{157}Gd (n, γ)^{158}Gd reactions uniformly across the plate, thereby reducing the contrast in the PSL distribution. The fact that measurable spatial variations were still obtained indicates that the field was within the dynamic range of the IP-ND and that the detector is capable of resolving spatial characteristics of the epi-thermal neutron field.

Experimental results demonstrated that the PSL distribution retains high spatial resolution, no more than 5 mm, even when several moderators are installed. This represents a major advantage of the IP-ND – based spectrometer: the imaging plate provides extremely fine pixel segmentation, enabling compact detector designs while preserving spatial information.

Furthermore, the relationship between the PSL values and the energy deposited by the ^{157}Gd(n, γ)^{158}Gd reactions was investigated. A linear trend was confirmed, showing a positive y-intercept in the fitting curve. Slight discrepacies were obserbed in the several reasons; different employments of the Au foils and boron blocks in the one IP-ND, the distribution of the gadolinium inside the IP. Since the neutron intensity is decreased in the distance of the neutron source, it is necessary to measure the epi-thermal neutron field in the same material compositions and the relationship between the distribution and the distance the source.

It is also important to measure the IP's response subtracting the γ-rays contributiion to investigate this tendency. Tanaka applied this discrimination technique, described in the following Equation (6.13),

$$N_{Gd} = N_{ND} \times \frac{N_{MS}}{R_{MS/ND}} \tag{6.13}$$

Where N_{Gd} is the spatial distribution from the ^{157}Gd(n, γ)^{158}Gd reactions, N_{ND} is the spatial distribution of IP-ND, N_{MS} is the one of BAS-MS, only sensitive for photons, and $R_{MS/ND}$ is the ratio of the detection rate in both IPs. The correction by $R_{MS/ND}$ is necessary because the composition and contents of the phosphor region are different from each other [65, 26].

As described in **Section 6.4**, this intercept likely represents the background contribution. Therefore, this analysis revealed that the background component can be appropriately handled by examining this relationship. These findings are very important for the calibration of the IP's response in PHITS. Based on the Equation (6.12), we can estimate the IP's response of the number of neutrons detected

in the specific ROI from the [T-deposit] tally in PHITS, without any preliminary experiments to distinguish neutrons and γ-rays.

Notably, we didn't correct the systematic variation because of the readout machine or positional uncertainty. According to the BAS-1800 manual, the shading correction in the readout process can introduce uncertainties of at least 5%. In addition, the fading effect must be considered as another reason for variation in the PSL values, even when the same measurement conditions are repeated across different experiments. It requires the experiment several times to investigate the linearity, and it is also important to take into account for the fading effect. According to Ref. [62], the fading effect is crucial in a few minutes, generally getting constant. Therefore, this influence can become equivalent by setting the time of readout process unite after the irradiation. Also, it can be approximated as an exponential function as performed by measuring the mean PSL values of the same IP-ND in several times [68].

As for the application of the neutron spectrometer, several things should be in consideration: First of all, it is essential to clarify the upper and lower limits of the measurable energy range, particularly when the system is intended to function as a broad-range spectrometer. The upper limit is defined by the saturation of PSL values, which occurs when an excessive number of neutrons are detected in the IP. In this study, however, the upper limit could not be identified because the 2-minute irradiation did not reach the saturation level.

In addition, obtaining distinct responses in each segmented region by placing moderators at different positions on the IP is crucial. The present experiment revealed that boron blocks with millimeter-scale thickness are sufficiently effective at stopping nearly all incident neutrons, which in turn makes it difficult to evaluate the contribution of epi-thermal neutrons. To cope with this issue, thinner boron blocks are desirable for the evaluation of epi-thermal neutrons. Moreover, the utilization of compounds seems to be effective such as boron nitride or boron carbide, and the other materials. For example, lithium based moderator might be a promising candidate because its cross-section also corresponds to 1/v rule, and the absolute value is smaller than that of boron. Furthermore, the neutron capture reaction of Lithium, ^{6}Li(n, α)^{3}H reaction doesn't produce any γ-rays. Other approahes include that the shielding material for ionization radiation, like Aluminum. it can trap the secondary particles generated from the moderator, taking results from backgrounds, such as β^{-} decay by Au foils.

Nevertheless, unlike the multiple-activation-foil method or Bonner Sphere Spectrometer, this IP-ND approach was demonstrated to have a potential in reproducing energy information over a wide and dynamic epi-thermal range using only a single plate in the contexts of high contrast reproduction and spatial resolution even in the epi-thermal field. The energy spectrum can be derived from the spatial distribution in a single irradiation experiment, if moderator design is optimized. Furthermore, even though compared with the PSPC, which can also estimate the spectrum from one irradiation, the IP-ND – based spectrometer is more compact and offers greater flexibility, as various moderators can be easily arranged on the plate surface to tailor

the detector response.

The moderator design work will be performed through the PHITS simulations. This process is the same as introduced in previous **Chapters 3 - 5**. The detector responses can be calculated using [T-deposit] tally in PHITS, and assigned multiple thicknesses of moderators onto the IP within the PHITS geometry. The response function can be made of the detector responses for the monoenergetic neutrons, and numerical analysis performed in the previous Chapters provides us with the design requirements for the IP-ND based spectrometer. In this way, a prototype of the spectrometer will be constructured, and the validation will be demonstrated in the experiment under the epi-thermal neutron field.

It might be also important to reduce the background noise and the measurement uncertainty by scattering effect in future. Such effects might be increased by placing a lot of moderators installed thotough one IP-ND. For this purpose, Artificial Neural Network has been applied to increasing the data quality and representativeness [117]. Besides, Topological Data Analysis (TDA) provides tools to extract the underlying structure even from highly noisy datasets. Its main method, persistent homology, has found successful applications to various machine learning problems, including radiation detection [118]. These approaches can capture wide-scale structural shape information in IP's data.

6.6 Summary

This study explores the use of a Gd-based imaging plate (IP) for epi-thermal neutron spectrometry. Gadolinium (Gd) was employed as a converter to detect γ-rays generated from the ^{157}Gd (n, γ) ^{158}Gd reactions. Additionally, introducing several thicknesses of boron blocks on the IP as moderators enabled the spatial distribution of neutron capture events to be used for deriving information on epi-thermal neutrons.

In order to confirm that the energy deposition was assumed to correspond to the PSL value, validation experiments have been performed in simple experimental systems (See **Sections 6.3 - 6.4**). Several thicknesses of boron (B_4C, ^{10}B) blocks were implemented and the epi-thermal neutrons irradiated to this system in KUR. The PSL was measured in BAS-1800, with the neutron flux monitored by the Au activation foil. The energy deposition was calculated in [T-deposit] tally of PHITS, and compared to the PSL value. This result clearly demonstrates the linearity was obserbed in this relationship. That means we can estimate the PSL value from [T-deposit], accordingly the spatial distribution of neutron numbers can also be obtained using the results of the Au foil. Since the energy deposited and the PSL values are both thought to be increased by reducing the deceleration ability of the moderator, we can evaluate the epi-thermal neutrons in wide dynamic range, within only-one IP-ND.

However, we also found that the boron blocks in mm scale are sufficiently effective at stopping nearly all incident neutrons, which in turn makes it difficult to evaluate the contribution of epi-thermal neutrons. Also, the identification of the upper/lower

limit of the PSL saturation due to the numerous neutrons irradiation beyond the IP-ND's detection capacity is essential to understand the measurable range of this spectrometer. This study served as an important initial step to evaluate the neutron energy spectrum in the epi-thermal range more accurately and simply. In future work, we will develop a detailed spectrometer systems; demonstrating a linearity more accurately, moderator optimization for spectrometer, and making the response function. Then, the validation experiments to fully reproduce epi-thermal neutron spectra under the epi-thermal field will be performed.

7 Conclusion

In conclusion, this thesis presents the neutron spectrometers which is capable of evaluating the energy spectrum in the epi-thermal range. Epi-thermal neutrons are utilized in a promising radiotherapy, boron neutron capture therapy. The energy spectrum should be assessed precisely to estimate the patient's dose and treatment time; however, conventional approaches have limitations in measurement accuracy, arising from their dependence on the number of materials as detectors. Furthermore, since multiple experiments are required to derive the spectrum, additional uncertainty is added due to varying experimental conditions.

Two devices were suggested in this thesis, a ^{3}He position-sensitive proportional counter and a neutron detection imaging plate (IP-ND), with the aim of the accurate evaluation of this parameter, only in one-time experiment. In **Chapter 2**, the principle, process to estimate the energy spectrum, and effectiveness of these spectrometers were outlined. The high and 1:1 correspondence of cross-sections for epi-thermal neutrons of ^{3}He in PSPC, and boron blocks placed on the IP-ND allows us to evaluate it in one-time experiment. Signal distributions including the information of the neutron's energy are measured, and then converted to the energy spectrum by spectrum unfolding technique. This study applied the bayes' theorem for this process, which was also compared to other conventional approaches and was proposed the effectiveness in high estimation performance.

We first focused on the PSPC, and a validation experiment was performed in our research accelerator, which demonstrated that the well estimation performance up to 1 keV. However, further improvements introduced across this thesis were also found for the application of the wide dynamic range of epi-thermal neutron spectrometry.

From **Chapter 3**, concrete approaches to expand the measurable range of the neutron energy spectra in the epi-thermal range have been described. Approaches in PSPC were introduced from **Chapter 3** to **Chapter 5**, and the feasibility investigation of the IP-ND was shown in **Chapter 6**.

First of all, in **Chapter 3**, a beam-type neutron source has been developed to reduce the neutron incident entering from the side surface of the PSPC, which was regarded as the trigger of the low-estimation performance.

For this purpose, we installed a collimator between the neutron source and detector. The material, width, hole diameter, and the distance between the source were investigated through the simulation work. As a result, an effective beam neutron source was successfully designed and developed; the material is polyethylene, 70 cm of width, 1.4 cm of hole diameter, and 3 m of the distance, reapectively. The beam characteristics were also examined in simulations, resulting in the highly collimated beam was designed in the range of 10 cm to 40 cm lengths from the exit of the collimator hole.

The effectiveness of this neutron source in the neutron spectrometery was also investigated numerically, and it could improve the estimation accuracy in lower-energy region; however, there still are sufficient discrepancies between the reference spectra. Besides, considering the reduction of the neutron incident reaching out to

the PSPC due to the collimator, more practical systems that allows the neutrons entering from the side surface were turned out to be necessary.

In **Chapter 4**, the effectiveness of the development of the response function in MC simulations was investigated. Simulations are necessary because the contributions of such neutrons can be evaluated only in the simulation, not theoretically. Modeling the experimental systems in my laboratory, the response function was calculated numerically, and its effectiveness was demonstrated through the numerical experiments as it has been done in **Chapter 3**. Estimated energy spectra reproduced the reference spectrum up to 5 keV, in contrast to the previous approaches. This result suggests that the scattering and reflection from other components in the experimental system might have a cucial impact on the estimation performance.

Furthermore, the estimation performance was proposed to be enhanced more by incorporating typical materials that have high-resonance cross-sections across the epi-thermal range. In this study, the presence of the sodium, which has a high-resonance cross-section at 2.5 keV, was found to cause the improvents of the estimation performance. Also, as the sodium rate was increased, the less the estimation performance, meaning highly dependent on that material. This mechanism offers the way of the approaches of the development of more robust neutron spectrometer, as well as covering more wide energy range.

In **Chapter 5**, the combination of the PSPC and Activation foils was investigated as another approach to expand the measurable range of this spectrometer. While the phisics in PSPC (using neutron capture reaction to detect neutrons) and activation foils are different, these methods can coexist and supplement with each other. We first prepared for 10 materials that can be sensitive in epi-thermal range, and the responses in each detector were obtained in simulations. Merged these responses with that of PSPC, we performed the numerical experiment to confirm its feasibility in beyond the epi-thermal range (by 100 keV). As a result, the estimation performance was improved compared to the previous approach, despite of the wide-energy region (0.5 eV to 100 keV). These findings suggest that the availability of several detectors simultaneously for the evaluation of the energy spectrum. Thus, the epi-thermal spectrometry can be performed by using advantages of each measurement technique, as introduced in this Chapter.

In **Chapter 6**, the feasibility of an IP-ND for the epi-thermal neutron spectroscopy was discussed. Thanks to high-spatial resolution and easy data processing, IP with Gadolinium converter can detect thermal neutrons, and it has a potential for the spectrometer with a simple comfiguration rather than other spectrometers. By implementing boron blocks that also have a high and 1:1 corresponding cross-section as ^{3}He has, we can reproduce the neutron's energy with the signal distribution.

To validate this, an irradiation experiment of epi-thermal neutrons was performed in Kyoto University Research reactor (KUR), that a boron block was stuck on a part of IP, and the Pixel value was obtained after the experiment. For benchmarking, ^{157}Gd (n, γ) ^{158}Gd response rate was calculated and compared to the PSL value. As a result, correlation was observed between the two, meaning that the PSL values can be derived from the simulation results. This fact is very important that

we can perform the design work of the spectrometer, and its response numerically.

In summary, the effectiveness of these approaches has been validated both in analytical examinations. We concluded that our proposed methodologies are effective wide dynamic range of the neutron spectrometry, over the epi-thermal region. This study proposed several Methodologies to measure the epi-thermal neutrons' spectrum in a wide dynamic energy range. A precise understanding of this parameter can be led to the safe treatments in BNCT. In BNCT, epi-thermal neutrons (0.5 eV to 10 keV, generally) are irradiated onto patients who have been administered boron-containing drugs. These neutrons are slowed down to thermal energies as they penetrate the body, enabling the ^{10}B (n, α) ^{7}Li reaction to occur. The resulting α particles and ^{7}Li nuclei then exert cytotoxic effects specifically on tumor cells.

Therefore, the neutron's energy spectrum is a crucial parameters to estimate the dose, and the irradiation time is also determined from this parameter.

Future work includes the experimental validation of these proposed approaches, and the application of this spectrometer in the actual accelerators used for BNCT treatments. As for the PSPC, the mixture of several materials which are sensitive resonance or activation cross-section across the epi-thermal range has a potential to enhancing the estimation performance. The optimization of material selections and these configurations is crucial to apply this for the neutron spectrometer. Not only that, this mechanism can be applied to other spectrometers, such as BSS. By incorporating some materials into the moderator (Polyethylene in general), the estimation performance can be improved as well. Since BSS is one of the most reliable methods and installed in some BNCT facilities, to investigate its effectiveness is important.

In terms of the IP-ND, the design work of the moderator is remained, and then validation experiment of this spectrometer can be performed in future. Using IP's characteristics, the detector size can get smaller than other spectrometers, and it is also easy to customize to combine with other methods, like putting some materials into the IP to obtain an unique response from themselves.

In this way, measurement systems suggested in this study can be scaled up for the real utilization, accelerating the safety evaluation of BNCT. This study lays the groundwork for evaluating the neutron field produced by the accelerator and the treatment effects in BNCT treatments.

Acknowledgements

First of all, this work was supported by the JSPS KAKENHI Grant-in-Aid (JSPS Fellows Number 24KJ1616). With this financial support, I could participate in a lot of international conferences and submit papers. I highly appreciate it.

I truly appreciate Prof. Isao Murata, who has bolstered me for 6 years. Your never-ending passion and deep knowledge of nuclear engineering granted me the basis of a researcher. Furthermore, I'm delighted that you are giving me opportunities to go around the world. I would also like to thank you, Prof. Shingo Tamaki, for helping me many times with your outstanding insights and precise feedback. I sincerely thank you, Dr. Sachie Kusaka, for supporting everything, not only with the administrative procedures but also with the life coaching.

I would like to express my sincere gratitude to Prof. Fuminobu Sato, Yoko Akiyama, and Sachiko Yoshihashi for their valuable time in reviewing my thesis.

I'm so grateful to Prof. John Ford for accepting me as a visiting scholar at Texas A&M University. Your strong and considerate messages helped me during my life in the US. You spread my horizon abroad. Thank you from the bottom of my heart, Ndum Zavier. Ndum, telling me about an amazing research topic, Microdosimetry. I learned from you that "Everything falls into place." I also want to appreciate Prof. Toru Obara and Tatsuya Katabuchi, who organize Studying Abroad Nuclear Innovation (SANI) program and giving me this impressive opportunity.

I'm very much obliged to Dr. Michael Walsh and Coriton Bruno for accepting me as an intern at the diagnostics team, ITER organization. You always cared for me, and I could have magnificent and precious experiences there. I also wish to thank the team members at Neutronics for giving me a lot of support, including Dr. Mariano Giovanni. I received thousands of supports from the admission to the private activities during my stay. I am truly grateful to Japanese staff, including Dr. Yutaka Kamada san. I will pour my effort into what can only be achieved in this moment, with the aim of becoming the kind of person you are.

I'm indebted to those who allowed me to join a team at brilliant research institutions, Brookhaven National Laboratory, Michigan University, Neutron therapeutics. Inc., Birmingham University, and Politecnico di Milano. I could have valuable experiences seeing the research staff and discussing our research.

Thanks a million to my supervisor, Mr. Takahiro Hirayama (Panasonic Corporation), young colleague, Masahiro Hori (Daikin industries. Ltd.), for inviting me on the path of a researcher. Also, let me take this occasion to say thank you to my laboratory colleagues for having had a lovely time. Additionally, I had the pleasure of spending wonderful time with members of my sub-major program and the AESJ Student Network. I truly appreciate all the memorable moments we shared.

I can't thank you enough, my parents. You are always on my side, giving me strict and thoughtful advice. Finally, I am grateful for the many meaningful relationships I have formed throughout my life across the world. These connections, which often transcend language and borders, have been an invaluable source of support and inspiration.

This doctoral journey has been both challenging and deeply rewarding, and I am grateful for every moment made possible by the support of those around me.
Thank you for being my friends, now and always.

References

[1] World Health Organization, *Cancer Control* **199** (2020).

[2] W. S. Halsted, *Ann. Surg.* **46**, 1–19 (1907).

[3] F. Torino et al., *Thyroid* **23** (2013).

[4] V. T. DeVita, C. Edward, *Cancer Research* **68** (2008).

[5] R. Baskar et al., *Int. J. Med. Sci.* **9**, 193–199 (2012).

[6] T. Watabe et al., *J. Nucl. Med.* **60**, 1301–1307 (2019).

[7] D. A. Jaffray et al., *Nature Cancer* **4**, 1228–1238 (2023).

[8] ICRP, *Ann. ICRP.* **37**, 1–332 (2007).

[9] T. Terasawa et al. *Particle Beam Radiation Therapies for Cancer*. Agency for Healthcare Research and Quality. (2009).

[10] W. A. G. Sauerwein et al. *Neutron capture therapy: Principles and applications*. Springer. (2012).

[11] J. Chadwick, *Nature* **129** (1932).

[12] G. L. Locher, *Am. J. Roentgenol. Radium Ther.* **36** (1936).

[13] L. E. Farr et al., *Trans. Am. Neurol. Assoc.* **13** (1954).

[14] L. E. Farr et al., *Am. J. Roentgenol. Radium Ther.* **71** (1954).

[15] A. K. Asbury et al., *J. neuropathol. exp. neurol.* **31** (1972).

[16] H. Hatanaka, *Basic life sciences* **54** (1990).

[17] A. H. Soloway, H. Hatanaka, M. A. Davis, *J. Med. Chem.* **10** (1967).

[18] K. Hideghéty et al., *J. Neuro-Oncol.* **62** (2003).

[19] W. F. Verbakel et al., *Int. J. Radiat. Oncol. Biol. Phys.* **55** (2003).

[20] Y. Mishima et al., *The Lancet.* **334** (1989).

[21] A. Wittig, W. A. Sauerwein, J. A. Coderre, *Radiat. Res.* **153** (2000).

[22] J. A. Coderre et al., *Cancer Research* **50** (1990).

[23] K. Yoshino et al., *Strahlenther Onkol.* **165** (1989).

[24] S.-H. Jiang et al., *Appl. Radiat. Isot.* **161**, 109143 (2020).

[25] L. Provenzano et al., *Appl. Radiat. Isot.* **88**, 171–176 (2014).

[26] H. Tanaka et al., *Appl. Radiat. Isot.* **69**, 1642–1645 (2011).

[27] H. Kumada et al., *Appl. Radiat. Isot.* **88**, 211–215 (2014).

[28] H. Horiike et al., *Appl. Radiat. Isot.* **106**, 92–94 (2015).

[29] K. Watanabe et al., *Appl. Radiat. Isot.* **168** (2021).

[30] S. Suzuki et al., *Appl. Radiat. Isot.* **199**, 110898 (2023).

[31] Neuboron Medical Group. *Neuboron Medtech starts animal pre-clinical study after successfully installed its BNCT system NeupexTM in China' s first BNCT Center*. URL: `https://en.neuboron.com/news/294.html` (2023). (Accessed 12/07/2025).

[32] L. Porra et al., *Acta Oncol.* **61**, 269–273 (2022).

[33] Neutron Therapeutics. *A Compact Neutron Source Designed for the Hospital Environment*. URL: `https://www.neutrontherapeutics.com/technology/` (2023). (Accessed 09/06/2025).

[34] K. Hirose et al., *Radiather. Oncol,* **155** (2021).

[35] S. Kawabata et al., *Neuro-Oncology Advances* **3** (2021).

[36] T. Kashihara et al., *Radiather. Oncol.* **202**, 110607 (2025).

[37] R. D. Rogus, O. K. Harling, J. C. Yanch, *Med. Phys.* **21**, 1611–1625 (1994).

[38] N. Hu et al., *J. radiat. Res.* **64** (2023).

[39] H. Tanaka et al., *Nucl. Instrum. Meth. Phys. Res. B* **267**, 1970–1977 (2009).

[40] International Atomic Energy Agency. *Advances in Boron Neutron Capture Therapy*. (2023).

[41] T. E. Blue, N. Gupta, J. E. Woollard, *Phys. Med. Biol.* **38** (1993).

[42] I. Auterinen et al., *Appl. Radiat. Isot.* **61** (2004).

[43] Y. H. Liu, W. L. Chen, S. H. Jiang, *IEEE Trans. Nucl. Sci.* **60** (2013).

[44] Y. Sakurai, T. Kobayashi, *Nucl. Instrum. Meth. Phys. Res. A* **531** (2004).

[45] S. Shiraishi et al., *Appl. Radiat. Isot.* **163** (2020).

[46] S. Tamaki et al., *Radiat. Prot. Dosim.* **180** (2018).

[47] H. Ueda, H. Tanaka, Y. Sakurai, *Appl. Radiat. Isot.* **106** (2015).

[48] G. F. Knoll. *Radiation Detection and Measurement*. (2010).

[49] I. Murata, H. Miyamaru, *Nucl. Instrum. Meth. Phys. Res. A* **589** (2008).

[50] M. McPheeters, K. McKinny, E. Yokie, *Nucl. Instrum. Methods Phys. Res. A* **1040** (2022).

[51] H. Toyokawa et al., *Nucl. Instrum. Meth. Phys. Res. A* **381** (1996).

[52] Y. Fujiwara et al., *J. Instrum.* **20**, P08018 (2025).

[53] Y. Osawa et al. *EPJ Web of Conferences*. (2017).

[54] Y. Fujiwara et al., *J. Radiat. Prot. Res.* (2025).

[55] Y. Fujiwara et al., *Appl. Radiat. Isot.*, 111719 (2025).

[56] H. Zhu et al., *IEEE Trans. Nucl. Sci,* **66** (2019).

[57] L. Zhao et al., *Jpn. J. Appl. Phys.* **64**, 066502 (2025).

[58] M. Kaburagi et al., *J. Instrum.* **19**, P11019 (2024).

[59] I. Murata et al., *Appl. Radiat. Isot.* **181** (2022).

[60] Y. Fujiwara et al., *Radiat. Meas.*, 107538 (2025).

[61] S. Shalev, Z. Fishelson, J. Cuttler, *Nucl. Instrum. Meth.* **71**, 292–296 (1969).

[62] N. Niimura et al., *Nucl. Instrum. Methods Phys. Res. A* **349**, 521–525 (1994).

[63] S. Tazaki et al., *Nucl. Instrum. Methods Phys. Res. A* **424**, 20–25 (1999).

[64] O. Iwamoto et al., *J. Nucl. Sci. Technol.* **60**, 1–60 (2023).

[65] T. Fujibuchi et al., *Radiat. Prot. Dosim.* **147**, 394–400 (2011).

[66] D. Schultz et al., *J. Phys. D: Appl. Phys.* **43**, 075502 (2010).

[67] Y. Sakurai, T. Kobayashi, *J. Nucl. Sci. Technol.* **39**, 1294–1297 (2002).

[68] Y. Ogino et al., *IEEE Trans. Plasma. Sci.* **51**, 2436–2442 (2023).

[69] K. Tanaka, S. Endo, M. Hoshi, *Appl. Radiat. Isot.* **68**, 207–210 (2010).

[70] K. Tanaka et al., *Appl. Radiat. Isot.* **88**, 143–146 (2014).

[71] K. Tanaka et al., *Appl. Radiat. Isot.* **106**, 125–128 (2015).

[72] K. Tanaka et al., *Appl. Radiat. Isot.* **115**, 212–220 (2016).

[73] A. Nohtomi et al., *Nucl. Instrum. Meth. Phys. Res. A* **633** (2011).

[74] Y. H. Chen et al., *Sci. China-Phys. Mech. Astron.* **57** (2014).

[75] X. Du et al., *Fusion Eng. Des.* **184** (2022).

[76] S. Iwasaki et al., *Appl. Radiat. Isot.* **48** (1997).

[77] M. Reginatto, P. Goldhagen, S. Neumann, *Nucl. Instrum. Meth. Phys. Res. A* **476** (2002).

[78] M. Matzke, *Report PTB-MN-19* (1994).

[79] J. Cvachovec, F. Cvachovec, *Mil. Technol.* **3** (2008).

[80] G. D'Agostini, *Nucl. Instrum. Methods Phys. Res. A* **362**, 487–498 (1995).

[81] F. Kamisaki et al., *Appl. Radiat. Isot.* **209**, 111299 (2024).

[82] H. Nishimura et al., *Appl. Radiat. Isot.* **185** (2022).

[83] Y. Nauchi, S. Iwasaki, *Nucl. Instrum. Meth. Phys. Res. A* **735** (2014).

[84] J. Bourbeau, Z. Hampel-Arias, *J. Open Source Softw.* **3**, 741 (2018).

[85] F. B. Bouallègue, J. F. Crouzet, D. Mariano-Goulart, *Ann. Nucl. Med.* **27**, 84–95 (2013).

[86] M. Febbraro et al., *Nucl. Instrum. Meth. Phys. Res. A* **989** (2021).

[87] S. Tamaki, F. Sato, I. Murata, *Nucl. Instrum. Meth. Phys. Res. A* **870** (2017).

[88] K. Kondo. PhD thesis. The University of Osaka, 2008.

[89] H. Kumada et al., *Radiat. Meas.* **177**, 107276 (2024).

[90] S. Tamaki et al., *Nucl. Instrum. Methods Phys. Res. A* **940**, 435–440 (2019).

[91] S. Tamaki et al., *Appl. Radiat. Isot.* **222**, 111836 (2025).

[92] B. E. Fischer, *Nucl. Instrum. Meth.* **141** (1977).

[93] C. J. Borkowski, M. K. Kopp, *IEEE Trans. Nucl. Sci.* **17**, 340–349 (1970).

[94] J. E. Sweezy et al. *MCNP - A General Monte Carlo N-Particle Transport Code, Version 5 - Volume 1: Overview and Theory.* (2003).

[95] T. Sato et al., *J. nucl. Sci. Technol.* **61** (2024).

[96] National Nuclear Data Center. ^{3}*He(n,p)*^{3}*H Cross Section from ENDF/B-VIII.0.* URL: `https://www.nndc.bnl.gov/sigma/getDataset.jsp?evalid=14963` (2025). (Accessed 12/07/2025).

[97] G. Schnabel et al., *Nuclear Data Sheets* **193**, 1–78 (2024).

[98] K. Shibata et al., *J. Nucl. Sci. Technol.* **48** (2011).

[99] J. Allison et al., *Nucl. Instrum. Methods Phys. Res. A* **835**, 186–225 (2016).

[100] P. K. Romano et al., *Ann. Nucl. Energy* **82**, 90–97 (2015).

[101] K. Sumita et al. *Commission of the European Communities.* (1983).

[102] S. Tamaki et al., *Plasma Fusion Res.* **17** (2022).

[103] Y. Tsuchikawa et al., *Scientific Reports* **15**, 7687 (2025).

[104] E. A. Klein et al., *Physical Review Applied* **15**, 054026 (2021).

[105] Y. Fujiwara et al. *Radiation Detectors And Their Uses.* 158–168 (2024).

[106] H. Lin et al., *Nucl. Instrum. Methods Phys. Res. A* **811**, 94–99 (2016).

[107] I. Murata, Y. Otani, F. Sato, *Appl. Radiat. Isot.* **106**, 75–77 (2015).

[108] Y. Bae et al., *AAPPS Bulletin* **32**, 34 (2022).

[109] Y. Kashiwagi et al., *Appl. Radiat. Isot.* **151**, 145–149 (2019).

[110] Y. Ge et al., *Med. Phys.* **51**, 6445–6457 (2024).

[111] B. Hidding et al., *Rev. Sci. Instrum.* **78** (2007).

[112] Y. Sakurai, T. Kobayashi, *Nucl. Instrum. Meth. Phys. Res. A* **453** (2000).

[113] H. Hideo et al. *THE EGS5 CODE SYSTEM.* (2005).

[114] Japan Atomic Energy Agency. *PHITS user' s manual.* (2024).

[115] Y. Miyoshi. *Soft Ferrite.* Springer Nature Singapore. (2025).

[116] J. Prateepkaew, Y. Sakurai, *Nucl. Instrum. Meth. Phys. Res. B* **557**, 165555 (2024).

[117] S. Bagherzadeh-Atashchi et al., *Eur. Phys. J. Plus.* **140**, 893 (2025).

[118] Z. A. Zaky et al., *Sci. Rep.* **15**, 16038 (2025).

List of Publications

Publications

Relevant to the Ph.D. Thesis

1. **Y. Fujiwara**, Y. Osawa, S. Tamaki, S. Kusaka, F. Sato, and I. Murata, "Experimental Investigation of A Neutron Energy Spectrometer in Low-Energy Range Using A Position-Sensitive Proportional Counter", *Journal of Instrumentation*, **20** P08018 (2025). doi: 10.1088/1748-0221/20/08/P08018.

2. **Y. Fujiwara**, S. Tamaki, F. Sato, and I. Murata, "Development of a measurement method for neutron energy spectrum in the low-energy range by combining activation foils and position-sensitive proportional counter-numerical study-," *Applied Radiation and Isotopes* **219**, 111719 (2025). doi: 10.1016/j.apradiso.2025.111719

3. **Y. Fujiwara**, S. Tamaki, S. Kusaka, F. Sato, and I. Murata, "Development of a new low-energy neutron spectrometer using a position-sensitive proportional counter: Examination of the response function considering the spectrometer shield," *Journal of Radiation Protection and Research* **50**, 43–48 (2025). doi: 10.14407/jrpr.2023.00325

4. **Y. Fujiwara**, S. Tamaki, S. Kusaka, F. Sato, and I. Murata, "Validation of Low-Energy Neutron Spectrometer Using A Position-Sensitive Proportional Counter. Design and Fabrication of Beam-Neutron Source", *Proceedings of the 37th Workshop on Radiation Detectors and Their Use*, 158–168 (2024).

Others.

1. **Y. Fujiwara**, S. Tamaki, S. Kusaka, F. Sato, and I. Murata, "AB011. Validation of a spectrometer to measure epi-thermal neutrons using a position sensitive proportional counter—development of pencil-beam epithermal neutron source with a deuteron-tritium (DT) neutron source ", *Therapeutic Radiology and Oncology*, 9**9** AB011-AB011 (2025).

2. **Y. Fujiwara**, M. Miyagawa, M. Yagura, J.Qiu, S. Tamaki, S. Kusaka, F. Sato, and I. Murata, "Simultaneous Use of Coincidence and Anti-Coincidence Counting Leveraging Crosstalk to Enhance Measurement Accuracy in BNCT-SPECT," *Radiation Measurements* **189**, 107538 (2025).

3. **Y. Fujiwara**, Z. N. Ndum, and J. Ford,
"Monte Carlo Microdosimetric Analysis of Medical Implant Effects on Radiation Quality and Biological Effects During Particle Radiotherapy," *Radiation Protection Dosimetry*, (Submission).

4. **Y. Fujiwara**, T. Sakabe, M. Okamura.
"IK-Frag: Frag data generator for the PHITS simulation with the inverse kinematic reaction producing a focused neutron beam," *Software Impacts*, (Submission).

Conference Presentations

Relevent to the Ph.D. Thesis | International Conferences.

1. **Y. Fujiwara**, "Low-Energy Neutron Spectroscopy Using A Position-Sensitive Proportional Counter," *12th Korea-Japan Joint Summer School, Aomori, Japan*, Aug 27 - 29, (Poster) (2025).
Awarded Encouragement award.

2. **Y. Fujiwara**, S. Tamaki, F. Sato, and I. Murata,
"Development of A Measurement Method for Neutron Energy Spectrum in the Low-energy Range by Combining Activation Foils and Position-sensitive Proportional Counter -Numerical Study-," 20th International Congress on Neutron Capture Therapy, Krakow, Poland, June, (Poster) (2024).

3. **Y. Fujiwara**, S. Tamaki, S. Kusaka, F. Sato, and I. Murata,
"Development of a New Low-Energy Neutron Spectrometer Using a Position-Sensitive Proportional Counter -Examination of Response Functions Including Shield-," ISORD-11 (Seoul, Korea, July 4-7) (2023) (Poster).

4. **Y. Fujiwara**, S. Tamaki, S. Kusaka, F. Sato, and I. Murata,
"Validation of A Spectrometer to Measure Epi-thermal Neutrons Using A Position Sensitive Proportional Counter. Development of pencil-beam epithermal neutron source with a DT neutron source," Young Researchers BNCT meeting (Online, November 14-17) (2022).

Domestic Conferences.

1. **Y. Fujiwara**, S. Tamaki, F. Sato, and I. Murata,
"Development of A Measurement Method for the Neutron Energy Spectrum in the Epi-thermal Range Using Imaging Plates," 61st Congress of Isotope and Radiation (Tokyo, Japan, July) (Oral) (2024).

2. **Y. Fujiwara**, S. Tamaki, S. Kusaka, F. Sato, and I. Murata,
"Development of a New Low-Energy Neutron Spectrometer Using a Position-Sensitive Proportional Counter -Simulation Study-," Spring 2024 annual meeting (Osaka, Japan, March) (Poster) (2024).
Awarded Encouragement award.

3. **Y. Fujiwara**, S. Tamaki, S. Kusaka, F. Sato, and I. Murata,
"Validation of Low-Energy Neutron Spectrometer Using A Position-Sensitive Proportional Counter. Design and Fabrication of Beam-Neutron Source," Workshop on Radiation Detectors and Their Uses (Tsukuba, Japan, January 26-27) (2023) (Poster).
Awarded Encouragement award.

Others | International Conference

1. **Y. Fujiwara**, J. Qiu, S. Tamaki, S. Kusaka, and I. Murata.,
"Directional Sensitivity Analysis of an Epi-thermal Neutron Flux Monitor for In-vivo Real-time Dosimetry in Boron Neutron Capture Therapy," *IEEE Nuclear Science Symposium Medical Imaging Conference and Room Temperature Semiconductor Conference (2025 NSS MIC RTSD)*, Yokohama, Japan, Nov 1-8 (Poster) (2025).

2. **Y. Fujiwara**, Z. N. Ndum, and J. Ford,
"Energy Dependency of Biological Effects from Radiation Scattering Around Medical Implants in Particle Therapy", *AAPM 67th Annual Meeting & Exhibition (AAPM 2025)*, Washington DC, United States, Jul 27 - 30, (Poster) (2025).

3. M. Giovanni, A. Kovarev, B. Coriton, D. Gin, S. Di Sarra, **Y. Fujiwara**, Q. Potiron, V. Krasilnikov,
"Simulations activities for the Calibration of ITER Neutron Diagnostics." *Fusion Neutronics Meeting 2025: ITER and beyond*, Spain, April (2025).

4. **Y. Fujiwara**, Z. N. Ndum, and J. Ford,
"Investigation of the Influence of Medical Implants on Radiation Quality and Biological Effectiveness Using Microdosimetry," The International Youth Nuclear Congress (IYNC2024), Abu Dhabi, United Arab Emirates, Sep 30 - Oct 5, (Poster) (2024).

Appendix

A Experimental Data Processing in PSPC

Due to the malfunction of the accelerator in my laboratory, I couldn't perform further experimental verifications for the use of the Beam-type neutron source, as well as the application of the calculated response function in MCNP 5. Therefore, this appendix summarizes the way to do the data processing of the pulse height spectrum in PSPC to obtain the depth distribution.

Figure A.1 illustrates the measurement system employed in the study to obtain the depth distribution. The ^{3}He PSPC was operated in the proportional mode, with the same voltage applied at both ends via a high-voltage power supply (714-1E, OKEN). Signals from the detector were amplified using a preamplifier (703-1C, OKEN) and main amplifier (590A; AMETEK ORTEC, Oak Ridge, TN, USA) before being fed into a multiparameter, multichannel analyzer (MCA, named in MCS-1600), which provided two-dimensional (2D) signal distribution images.

Figure A.2 depicts a representative signal distribution image obtained by irradiating the ^{3}He PSPC with an Am – Be neutron source for 10^5 s. The voltages at both ends of the ^{3}He PSPC are denoted as Vol_x and Vol_y: the sum of which ($Vol_x + Vol_y$) at a given detector depth reflects the energy imparted to both ends by the ^{3}He (n, p) ^{3}H reaction, which ideally remains constant. However, the energy imparted to each particle may decrease due to the wall effect [48]. Therefore, the experimental results became a two-dimensional distribution. Moreover, the Vol_x/Vol_y ratio corresponds to the detection position along the ^{3}He PSPC, which is also reflected by the slope in Figure A.2. Therefore, the depth distribution was obtained by counting signals corresponding to detection positions within the ^{3}He PSPC, determined by the angle of the slope in Figure A.2.

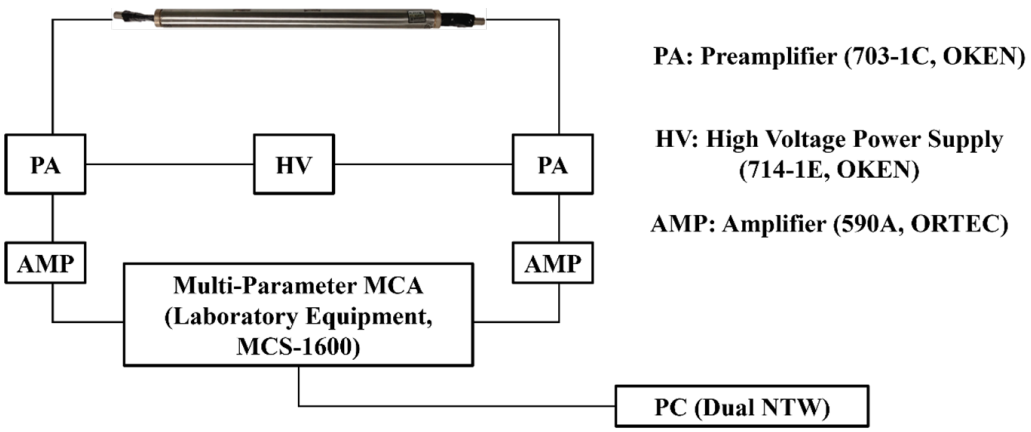


Figure A.1: Electrical circuit for the PSPC experiments.

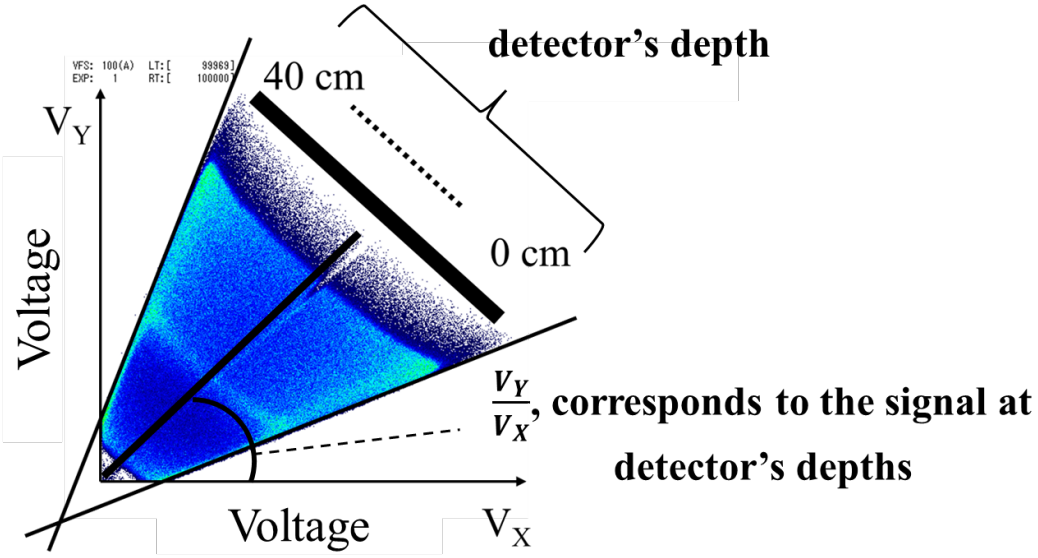


Figure A.2: An example of a two-dimensional distribution in PSPC experiments. "Voltage" means the voltage of electrical signals. Due to the wall effect, signals exhibit a fan-shaped distribution. A depth distribution can be obtained by counting the signals for the angle related to the ratio of the V_X and V_Y , $\frac{V_Y}{V_X}$.

Prior to the validation experiment, the detector's calibration is required, such as establishing the relationship between the angles in the 2D signal distribution and the detection positions, as well as methods for correcting background effects. To this end, this section presents the calibration results obtained using simpler experimental setups than those used in the validation experiment.

- **Detection position determination**

  In PSPC, the signals are then counted as a function of the angle corresponding to the ratio V_x/V_y, allowing us to derive the depth distribution. Therefore, to determine the count corresponding to each segment of the PSPC, it is essential to establish the relationship between the segment position and the angle in the two-dimensional distribution. For this purpose, we exposed each segment of the PSPC and obtained its two-dimensional distribution individually. The peak angle for each segment was then extracted to serve as a reference for identifying the segment-specific count in actual measurements. Figure A.3 illustrates the experimental system employed to examine the relationship between the angles in the 2D signal distribution and detection position. A thermal neutron field was generated by moderating neutrons in carbon and irradiating the bare region of the ^{3}He PSPC. PE (polyethylene) was utilized to produce the beam, and Cd was used to shield the thermal neutrons. The irradiation time was 1 h. This process was repeated for different positions in the ^{3}He PSPC (with 1 cm intervals). To obtain the angular distribution of signals from the 2D signal distribution, we calculated $\tan^{-1}$ for every point (θ) and

obtained signal counts for $\theta = 0°$ to 90°, with 0.1° bins. The peak degree for each detector depth was derived using Equation (A1):

$$\theta_i^{'} = \frac{\Sigma_i(\theta_i \cdot C_i(Pre))}{\Sigma_i C_i(Pre1)} \tag{A1}$$

where $\theta_i^{'}$ refers to the peak degree for each depth of the ^{3}He PSPC and C_i(Pre1) refers to the signal count for each bin in the preliminary experiment. Figure A.4 presents the angular distributions of signals in the ^{3}He PSPC at several depths. The peak degree could not be obtained at detector depths of 3, 4, and 38 cm, as it was buried under the peaks at other depths. Additionally, we could not obtain 2D signal distributions at detector depths of 1, 2, 39, and 40 cm owing to the end effect in the ^{3}He PSPC [48].

- **Background Calibration**

  Signal counts at different detection positions are ideally the same when neutrons are isotropically reaching the ^{3}He PSPC. However, as a result of the preliminary experiments, the sensitivity at each position of this PSPC was revealed to be different systematically. Therefore, we introduced a correction factor (eff_i) to obtain the precise data, as described in the following Equation (A2):

$$eff_i = \frac{\bar{C}}{C_i(Pre2)} \tag{A2}$$

  where $\bar{C}$ refers to the average ^{3}He PSPC counts and C_i(Pre2) refers to the signal count at each detector depth, in the 2nd preliminary experiment. The ^{3}He PSPC was exposed to the laboratory conditions, which contained background neutrons, for 10^5 s. Figure A.5 presents the eff_i values for each detector depth. Therefore, the signal count (eff_i) was expressed as follows:

$$C_i(True) = eff_i \cdot C_i(Ex) \tag{A3}$$

  where $C_i(Experiment)$ refers to the signal count in the validation experiment.

Through these calibration processes, the experimental data was obtained. Figure A.6 presents the 2D signal distribution obtained from the validation experiment, where neutrons were irradiated for 8 hours. The dark blue region in the lower left of the 2D signal distribution corresponds to electromagnetic noise generated during accelerator operation. Then, Figures 1.7 and 1.8 were derived from this result.

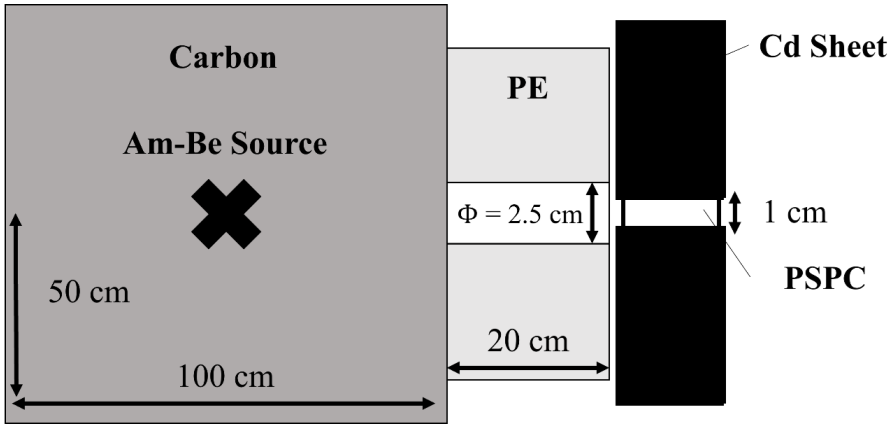


Figure A.3: Experimental system to determine the detection position (Pre 1).

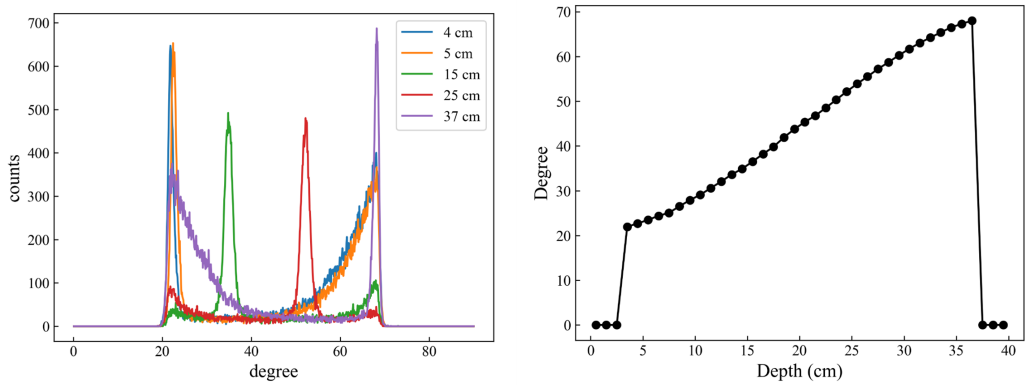


Figure A.4: Left: Angular distributions at several depths of PSPC. Right: Relationship between the peak degree and the detection position.

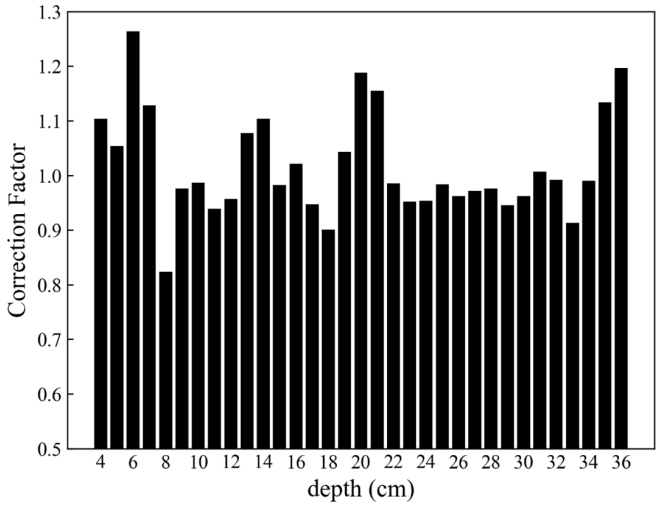


Figure A.5: correction factor (eff_i) at detector's depths (Pre 2).

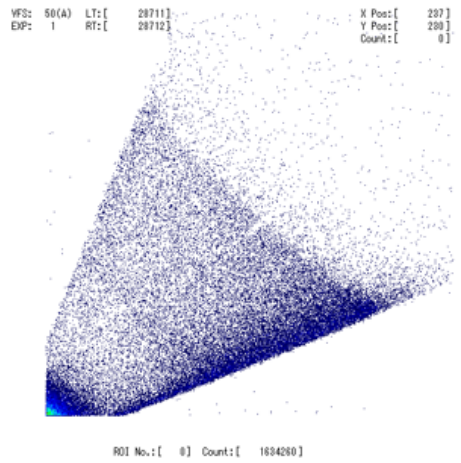


Figure A.6: Two-dimensional distribution in the validation experiment.

ALGORITHM 4: Bayesian unfolding algorithm based on the PyUnfold module [84].

Input: $\mathbf{y} = \mathbf{R} \times_{\mathbf{ref}}$, $R \in \mathbb{R}^{n \times m}_{\geq 0}$, $\mathbf{est}^{(0)} = \dfrac{1}{m}$, $N_{\text{iter}<=}$ 10000

Output: $\mathbf{\Phi}_{\text{est}}$

// Compute $f_j = \sum_{i=1}^{m} R_{ij}$ and normalized response $R'_{ij} = R_{ij}/f_j$

for $j = 1, \ldots, n$ **do**

  $f_j \leftarrow \sum_{i=1}^{m} R_{ij}$

  for $i = 1, \ldots, m$ **do**

    $R'_{ij} \leftarrow \dfrac{R_{ij}}{f_j}$

// Main loop, acquisition of $\mathbf{\Phi}_{\text{est}}^{(k+1)}$

$\text{RMSE}^{(1)} \leftarrow \infty$ // Initial RMSE value

for $k = 0, 1, \ldots, N_{\text{iter}} - 1$ **do**

  $\mathbf{q}^{(k)} \leftarrow R' \, \mathbf{\Phi}_{\text{est}}^{(k)}$ // n-dim predicted counts

  for $j = 1, \ldots, m$ **do**

    $\Phi_{\text{est},j}^{(k+1)} \leftarrow \Phi_{\text{est},j}^{(k)} \cdot \sum_{i=1}^{n} y_i \dfrac{R'_{ij}}{q_i^{(k)}}$

  $\text{RMSE}^{(k+1)} \leftarrow \sqrt{\dfrac{1}{m} \sum_{l=1}^{m} \left(\Phi_{\text{est},l}^{(k+1)} - \Phi_l^{\text{ref}} \right)^2}$

  if $\text{RMSE}^{(k+1)} > \text{RMSE}_{\text{k}}$ **then**

    break

  $\text{RMSE}^{(\text{k})} \leftarrow \text{RMSE}^{(k+1)}$

return $\mathbf{\Phi}_{\text{est}} \leftarrow \mathbf{\Phi}_{\text{est}}^{(k+1)}$

B Comparison to Unfolding Algortihms

The full implementation of the spectrum unfolding algorithms, including MLEM, conventional Bayesian, and PyMC-based Bayesian methods, is available on GitHub at the following repository: `https://github.com/furiwara19/Ph.D.-project/tree/main/spectrum_unfolding`.

The repository contains modular Python code with command-line interface support, designed for reproducibility and extensibility. As discussed in **Section 2.3**, there have been several unfolding algorithms developed so far, and it is debating that which algorithm is the best to solve the inverse problem. This section compared the performance of each algorithm by the convergence time and the robustness. Unfolding algorithm based on PuUnfold was exhibited in Algo 4.

The contribution of random noise for the unfolded spectrum depends on the choice of stopping criteria, as discussed in **Section 2.3.3**. In order to discuss the effectiveness of "Nauchi-Bayes" method, this section investigates the iteration times and RMSE values for "ideal iteration number" among algorithms. Note, that this investigation was performed for the spectrometer when it was placed inside the concrete hole, as discussed in **Section 4.3**. Estimation performance of "Nauchi-Bayes" method was evaluated for the robustness and the coincidence with reference spectra $\boldsymbol{\Phi_{ref}}$. The iteration numbers that were determined the previous paragraph was used for this comparison.

Firstly, the convergence speed was assessed with other unfolding algorithms. Figure B.1 shows the energy spectra in the algorithms (See **Section 2.3.2**), indicating that our method has the equivalent convergence speed compared to GRAVEL and MLEM; however, PyUnfold shows the different spectrum shape from others. This result also meant that the convergence speed of PyUnfold might be slower than others, even in the epi-thermal neutrons spectroscopy.

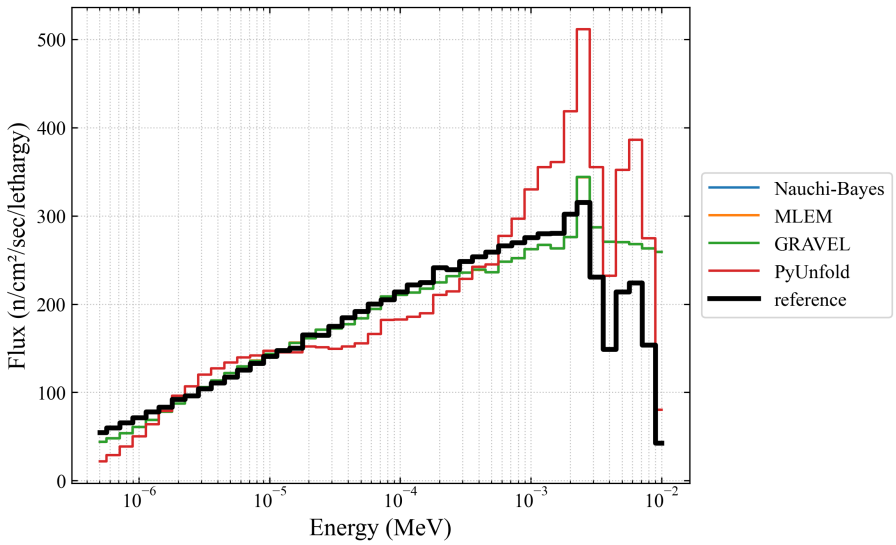


Figure B.1: Neutron energy spectra estimated by in different algorithms.

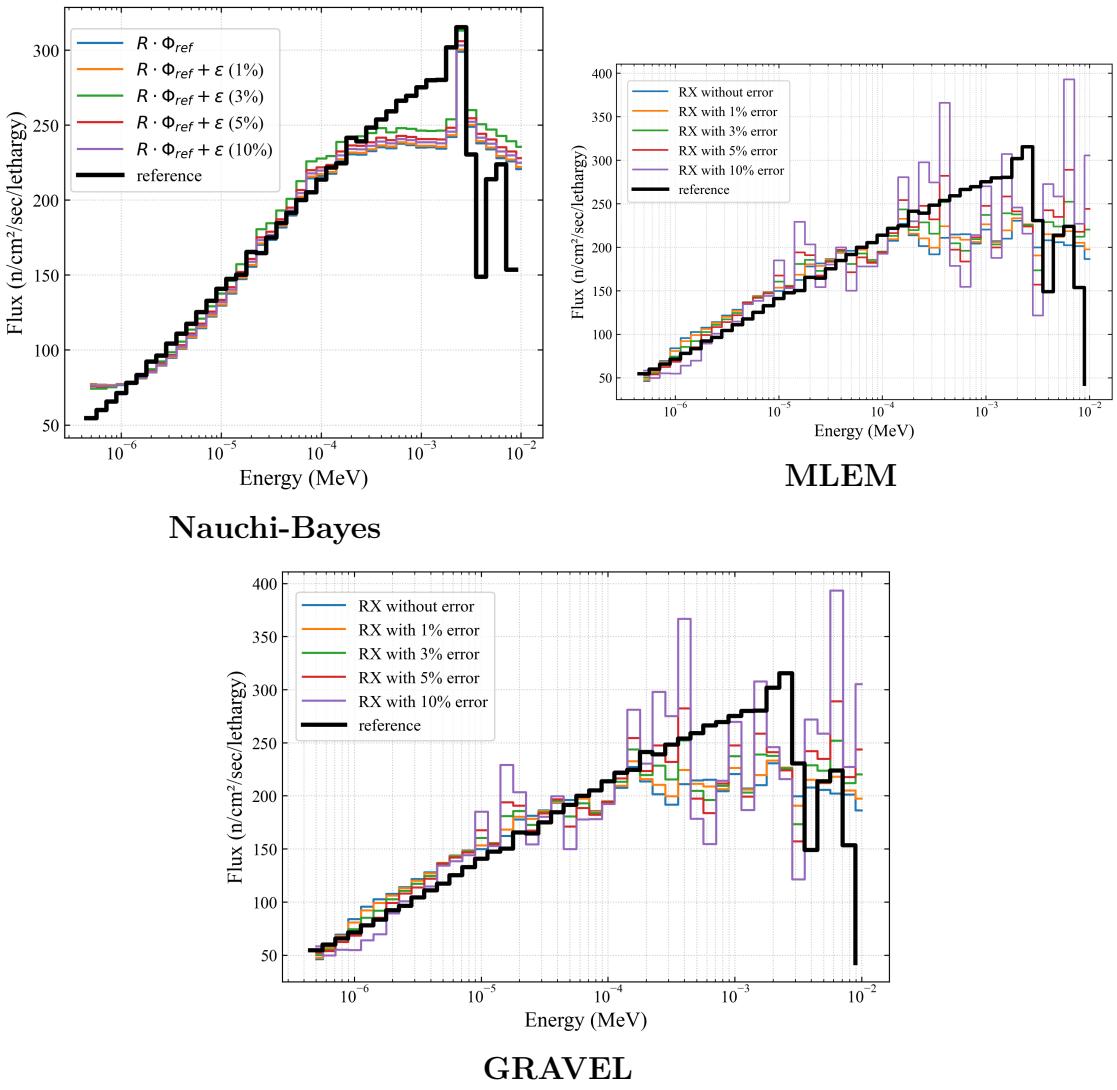


Figure B.2: RMSE values variation in unfolding algorithms.

Secondly, unfolded spectra for $\boldsymbol{R \cdot \Phi_{ref} + \epsilon}(5\%)$ was compared to investigate the iteration number and robustness of algorithms, as depicted in Figure B.2. Results of statistical test to judge the estimation performance was also exhibited in both Figure B.3 and Table B.1. These results indicate that the estimated spectra are reproduced more accurately with respect to $\mathbf{\Phi_{ref}}$ than with other algorithms. In particular, the statistical metrics clearly demonstrate that both the required iteration numbers and the RMSE values are smallest for the Nauchi-Bayes method. Interestingly, the estimation results obtained using the GRAVEL and MLEM algorithms are almost identical, whereas those from the Nauchi-Bayes method differ significantly. In this study, the Nauchi-Bayes method was adopted from a statistical performance perspective; however, there is still no consensus on the optimal algorithm for this ill-posed problem.

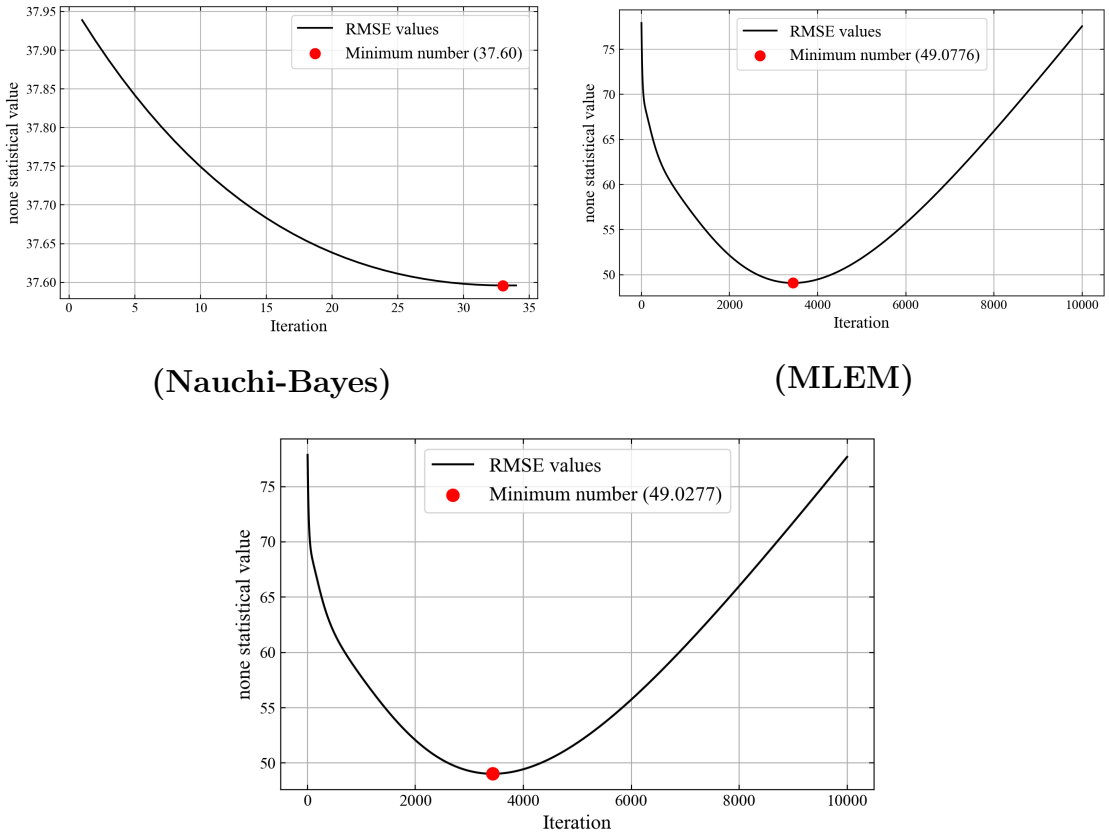


Figure B.3: RMSE values variation in unfolding algorithms.

Table B.1: Iteration numbers and RMSE values in Unfolding Algorithms

Algorithms	Iteration Number	RMSE value	nRMSE values
Nauchi-Bayes	34	37.6	0.237
MLEM	2500	49.08	0.31
GRAVEL	2500	49.02	0.31

C Unique Subsequent MCNP Calculation

This study requires the Subsequent calculation because the geometry is massive and detailed structure so that it spends huge computational time to obtain results without large uncertainties. In MCNP, a Surface Source Write Card (SSW) records the information of the particle incidents at the defined surfaces, and then Surface Source Read Card (SSR) enables us to use the information in SSW for the desired calculation [94]. As for PHITS, the same function can be performed by creating "dump file" at a certain surface, and then set information tallied in that surface (s-type = 17) [114]. However, this function was found not to be enough to get good

statistics in this study, for instance, the energy spectrum had a luck of data in very small angle, as shown in Figure C.1. This fact means that neutrons transported in this method cannot reach the detector region if the hole diameter of the collimator is extremely small, leading to be unable to design work, or response function calculation.

To cope with this issue, we applied the unique subsequent calculation method. First of all, the neutron currents and the angular distribution at the exit of the epi-thermal column, where titanium was assigned, were calculated. These parameters were then incorporated into the SDEF card for the next simulation. This process means to set the bias the area of the simulation, and the direction of the neutron incidents. Therefore, to correct this effect, we also multiplied the weight of these procedures to the results of the desired simulations.

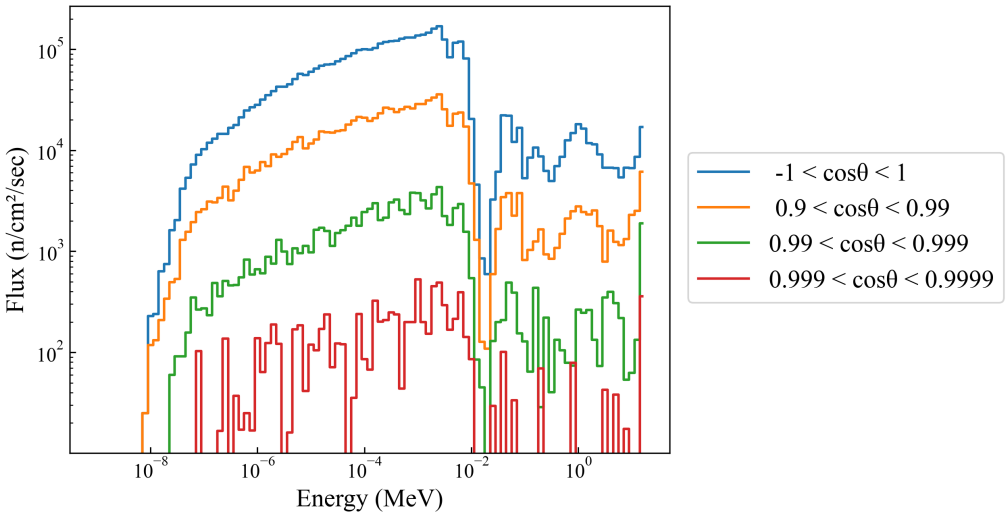


Figure C.1: Energy spectra at the epi-thermal column in the neutron emission angles. The luck of data was observed, because none neutrons were not tallied. Due to this, this figure illustrates the spectrum in the shape of lines, not histgrams.

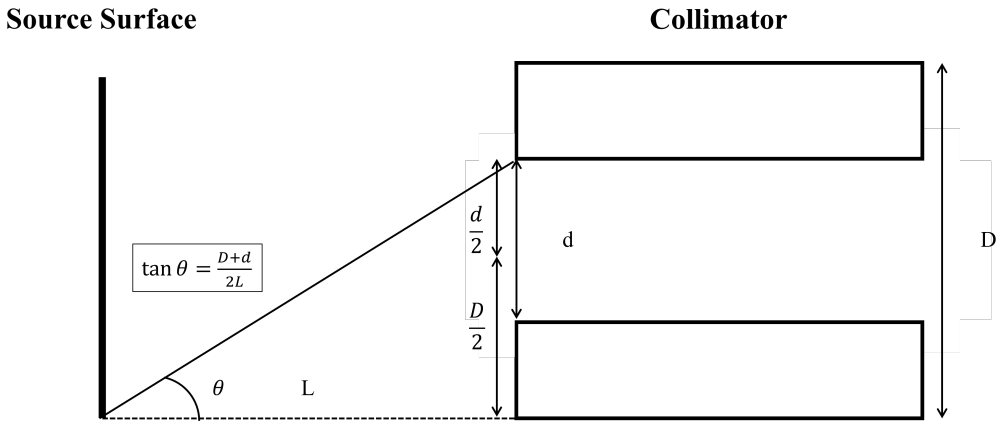


Figure C.2: A sketch of the determination of the θ in this study.

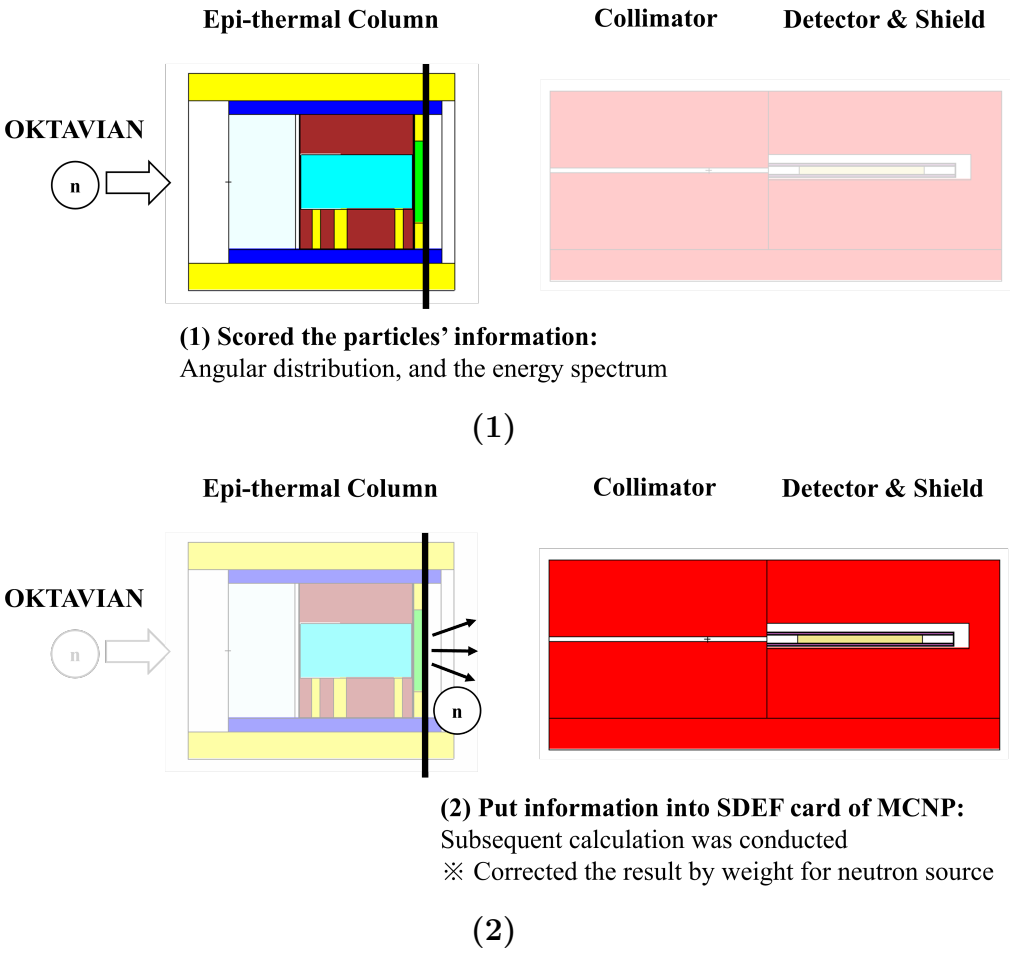


Figure C.3: illustrations of the procedures of the subsequent calculations performed in this study. We first performed the neutron flux and angular distribution calculations to obtain the incident information at the exit of the epi-thermal column (Titanium plane, green colored). Next, depth distribution or detector response were calculated with the particle information put into the SDEF card in MCNP. Note, the particle information (energy spectrum, angular distribution, i.e.) was interpolated by the bins of energy/emission angle.

It is one of the bias methods, that allows us to create an ideal situation for incidents to irradiate the Tally region, resulting in getting meaningful calculation by adjusting the weights at the source surface or its emission angle. For weight, we put into the angle in the emission angle, and this effect was corrected in the following Equation (C1).

$$W = \int_{cos\theta}^{1} f(x)dx \tag{C1}$$

Where θ is the emission angle, determined in the following Equation (C2),

$$tan\theta = \frac{D+d}{2L} \tag{C2}$$

Where D, d, and L was defined 10 cm, 5 cm, 1 m, respectively. Thus, θ means the maximum angle that neutrons can reach the hole diameter from the edge of the source surface, as shown in the Figure C.2.

Using this W, simulaton results using this source became:

$$\Phi \text{ (Real)} = \Phi \text{ (MCNP)} \times W \tag{C3}$$

In **Chapters 3, 4, and 5,** we set the subsequent surface at the center circle of the exit of the epi-thermal column with 2.5 cm ϕ, and the neutron current and angular distribution was calculated using F1 tally in MCNP. Simulation results of subsequent calculations were summarized in Figure C.3, and they were used in each Chapter.

D Source Code for the Simulation and Data Processing

Any other data analysis codes, making the graphs of response functions, nuclear cross-sections of materials, and simulation codes are presented in this Section. All code descriptions were opened to a public folder (`https://github.com/furiwara19/Ph.D.-project/tree/main/spectrum_unfolding`.)

In this paper, the simulation files for the preparation of response function and other settings to model the experimental system were exemplified. As for the data processing codes, Python-based source codes for the response function preparation, unfolding iteration algorithms, and stopping criteria determination were shown in this Section as examples.

Source Code 1: MCNP Example Input File

```
c Collimator design - Response Calculation
c $SDEF card writing
c sdef
c
sdef  erg =d1 vec=a b c  pos=X Y Z  dir=d2  rad=d3   axs=1 0 0
c
c Energy bin settings for response function.
c Set the whole energy range to calculate the detector response
c
si1   5e-07 6.29e-07
c set monoenergetic neutrons with the same lethargy
c
sp1    0 1
c
c
c probability
c particles directly settings
si2    0 0.1 0.2 0.3 0.4 0.5 0.6 0.7 0.8 0.9 1
sp2    0 7.97256E-05 2.78209E-04 5.30646E-04 8.33193E-04 1.19164E-03
       1.60132E-03 2.06897E-03 2.60745E-03 3.23054E-03 3.98396E-03
```

```
c
c surface settings
c
si3    0 15
sp3    -21 1
c
c $tally card (Use F4 tally)
c
F4:N 200 $cell number of the PSPC, 200
FM4 (0.000122 20 103)
c
c Set atomic density, material number of 3He, and MT number
c (103 = (n,p) reaction)
c
SF4 300
c
c surface settings to calculate.
c surface 300 is the top surface of PSPC.
c detector separation.
c
FS4 301 302 303 304 305 306 307 308 309
        310 311 312 313 314 315 316 317 318
        319 320 321 322 323 324 325 326 327
        328 329 330 331 332 333 334 335 336
        337 338 339 T
c
c
F114:N 200  $cell number of the PSPC, 200
FM114 (0.000122 20 103)
SF114 241
c surface 241 is side surface of PSPC.
FS114   301 302 303 304 305 306 307 308 309
        310 311 312 313 314 315 316 317 318
        319 320 321 322 323 324 325 326 327
        328 329 330 331 332 333 334 335 336
        337 338 339 T
c For response rate calculations of activation foils,
c add other F4 tallies.
F14:N 401 $Cell settings to calculate
FM14 (0.0222 39 102) $ MT=102 is (n,gamma)
```

Source Code 2: Response Function hundling

```
model_name='model1' #defined by users
# date='1127'
date = '1220'
names = ['0,5eV','0.631eV', '0.794eV','1eV', '1.26eV','1.58eV','2eV','2.51eV','3.16eV',
      '3.98eV','5eV','6.31eV','7.94eV', '10eV','12.6eV','15.8eV','20eV','25.1eV',
      '31.6eV','39.8eV','50eV','63.1eV','79.4eV', '100eV','126eV','158eV','200eV',
      '251eV','316eV','398eV','500eV','631eV','794eV','1keV','1.26keV','1.58keV',
      '2keV','2.51keV','3.16keV','3.98keV','5keV','6.31keV','7.94keV','10keV']
whole_cell_result = []
weight0 = 3.64e-3 #weight (See Appendix C)
cf = 0.586 #CF ratio
v = 4.91 #volume
s=707
intensity = 1e9 #intensity of OKTAVIAN
folder = USER defined

# data processing
cdata = np.zeros((44, 40))
response_around3keV = []
x = np.linspace(1, 40, 40).tolist()
for i in range(44):
    file_num = i + 1
    file = folder + 'r_' + str(file_num) + '.o'

    try:
        with open(file, errors='ignore') as f:
            data = f.readlines()
            results = []
            for index, line in enumerate(data):
                if line.find('multiplier bin:   1.22000E-04 ') >= 0:
                    try:
                        value = float(data[index + 1].split()[0]) *  s * cf * v #*intensity*weight0
                        results.append(value)
                    except (IndexError, ValueError) as e:

            if len(results) < 40:

            flux = results[:40] if len(results) >= 40 else [0] * 40
            if names[i] in ('2keV', '2.51keV', '3.16keV'):
                response_around3keV.append(flux[:10])
    except FileNotFoundError:
        continue

    # plt.plot(x, flux, label=names[i])
    cdata[i] = flux

```

```
Activation foils

for i in range(53):
    results = []
    file = folder + '\\activation_foils_all_papers_r_' + str(i+1) + '.o
        '
    try:
        with open(file, encoding='shift_jis', errors='ignore') as f:
            data = f.readlines()
    except FileNotFoundError:
        print(f"[WARN] {file} not found. skip.")
        continue

    for index, line in enumerate(data):
        if ' multiplier bin:' in line:
            results.append(float(data[index + 1].split()[0]))
            activation = [val*cf*s for val in results[:10]]
            response   = [val*v3*cf*s for val in results[10:50]]

    activation_In_Au     = [val*v2 for val in activation[:2]]
    activation_I_As_Ag   = [val*v1 for val in activation[2:5]]
    activation_W         = activation[5]*v2
    activation_Ni_Mn_Mo  = [val*v1 for val in activation[6:9]]
    activation_Dy        = activation[9]*v2
    activation_rate = activation_In_Au+activation_I_As_Ag+[activation_W
        ]+activation_Ni_Mn_Mo+[activation_Dy]

    response_pspc.append(response)
    response_foils.append(activation_rate)
```

Source Code 3: Iterative unfolding algorithms

```
# R, X should be prepared by users. This study obtained these
    parameters from the MC simulations.
# Bayes Algorithm based on Nauchi.
def Nauchi_Bayes(r, X, target, calc_num):
    x_initial = 1/len(X)
    arr_est = np.full((len(X),1),x_initial)

    rt = np.empty_like(r) # empty arrays
    for i in range(len(target)):
        rt[i] = r[i] * target[i]

    for _ in range(calc_num):
        denominator = r @ arr_est

        numerator = np.empty_like(r)
        for l in range(len(target)):
            row_index_2 = l
            multiplier_2 = denominator[l]
            numerator[row_index_2] = rt[row_index_2] / multiplier_2

        numerator = numerator.sum(axis = 0).reshape((len(X),1))
        arr_est = numerator * arr_est

    return arr_est

# This function is necessary to obtain estimated values from the
    itereted value.
def inverse_X(arr_est, F_inv):
    return F_inv @ arr_est

# GRAVEL Algorithm.
def gravel(R, Y, Phi0, iterations, eps=1e-12, sigma=None, use_sigma=
    False):
    """
      R: (m, n) response
      Y: (m,) measured counts (>=0)
      Phi0: (n,) initial spectrum (>=0). default = uniform
      iterations: number of iterations
      eps: small positive to avoid 0-div & log(0)
      sigma: (m,) measurement std (>=0) if used
      use_sigma: if True, weight by (Y/sigma)^2 (Poisson:sigma=sqrt(Y))
    """
    R   = np.asarray(R, dtype=float)
    Y   = np.asarray(Y, dtype=float).reshape(-1)
    m,n = R.shape

    x_initial = 1/len(Phi0)

    Phi = np.full((len(Phi0),1), x_initial).reshape(-1)
    Phi = np.clip(Phi, eps, None)

    if use_sigma:
```

```
50          if sigma is None:
51              sigma = np.sqrt(np.clip(Y, eps, None))
52          else:
53              sigma = np.asarray(sigma, dtype=float).reshape(-1)
54              sigma = np.clip(sigma, eps, None)
55          w_meas = (Y / sigma) ** 2   # (= Y^2 / $\sigma$^2)
56      else:
57          w_meas = np.ones_like(Y)
58
59      for _ in range(iterations):
60          # Q_i^{(k)} = sum_j R_{ij} X_j^{(k)}
61          Q = R @ Phi
62          Q = np.clip(Q, eps, None)
63
64          # W_{ij}^{(k)} = w_meas_i * ( Y_i * R_{ij} * X_j^{(k)} / Q_i^{(
                k)} )
65          W = w_meas[:, None] * (Y[:, None] * R * Phi[None, :] / Q[:,
                None])
66
67          # ln(Y_i / Q_i^{(k)})
68          log_ratio = np.log(np.clip(Y / Q, eps, None))
69
70          #  $\Phi_j^{(k+1)} = \Phi_j^{(k)} * exp((\Sigma_i W_{ij} \times
                ln(Y_i/Q_i))/ (\Sigma_i W_{ij}) )$
71          num = (W * log_ratio[:, None]).sum(axis=0)
72          den = np.clip(W.sum(axis=0), eps, None)
73          Phi = Phi * np.exp(num / den)
74
75          Phi = np.clip(Phi, eps, None)
76
77      return Phi
78
79  # MLEM Algorithm
80  def MLEM(R, target, ref, iters, eps=1e-12):
81      """
82      R: (I, J) response function
83      y: (I,) or (I,1) measured data
84      x0: (J,) or (J,1) initial spectrum
85      iters: iterations
86      """
87      R = np.asarray(R, dtype=float)
88      print(R.shape)
89      y = np.asarray(target, dtype=float).reshape(-1, 1)
90      x = np.asarray(ref, dtype=float).reshape(-1, 1)
91      # initial number
92      initial = 1/len(ref)
93      arr_est = np.full((len(ref),1),initial).reshape(-1,1)
94      print(arr_est.shape)
95
96      colsum = R.sum(axis=0).reshape(-1, 1)
97      colsum[colsum == 0] = np.inf
98
99      for _ in range(iters):
```

```
        Rx = R @ arr_est
        Rx = np.clip(Rx, eps, None)

        # bayesian updating
        arr_est = (arr_est / colsum) * (R.T @ (y / Rx))

    return arr_est

# PyUnfold Algorithm.
from pyunfold import iterative_unfold
from pyunfold.callbacks import Logger
def estimate_pyunfold(R, ref, target, error, prior=None,
                      rng=None, max_iter=10000, tol = 1e-4):

    r = np.asarray(R, float)           # (m, n)
    m, n = r.shape

    ref = np.asarray(ref, float).reshape(-1)   # (n,)
    assert ref.shape[0] == n

    y = target.reshape(-1)                  # (m,)
    assert y.shape[0] == m

    seed = 123
    if rng is None:
        rng = np.random.default_rng(seed)
    data_err = y * error * rng.random(len(y))               # (m,)
    response_err = np.full_like(r, 1e-12)      # (m, n)

    prior = ref.copy()
    s = prior.sum()
    prior = prior / s if s > 0 else np.full(n, 1.0/n)
    efficiencies = np.ones(n)                  # (n,)
    efficiencies_err = np.zeros(n)             # (n,)

    res = iterative_unfold(
        data=y, data_err=data_err,
        response=R, response_err=response_err,
        efficiencies=efficiencies, efficiencies_err=efficiencies_err,
        prior=prior, ts='ks', ts_stopping=0.0,
        max_iter=max_iter, return_iterations=True, callbacks=[Logger()]
    )

    return res
```

Source Code 4: Iterative unfolding algorithms with stopping criteria

```
1
2  def Nauchi_Bayes(
3      r, X_ref, calc_num, error,
4      stopping_method=None, seed=None, rng=None,
5      tol = 1e-5, patience=3, eps=1e-12, return_trace=True, record_every
           =1,
6      stat_when_no_stop="ideal"
7      ):
8      r = np.asarray(r, dtype=float)
9
10     # normalization
11     normalized_r, F_inv = r_normalization(r)
12
13     target = r @ X_ref
14
15     y = np.asarray(target, dtype=float).reshape(-1)
16     m, n = normalized_r.shape
17
18     arr_est = np.full((n, 1), 1.0/n, dtype=float)
19
20     if rng is None:
21         rng = np.random.default_rng(seed)
22     errors = y * error * rng.random(len(y))
23
24     target_values = []
25     for t, e in zip(y, errors):
26         target_values.append(t+e)
27
28     rt = normalized_r * np.asarray(target_values, dtype=float).reshape
           (-1, 1)
29     X_ref_vec = np.asarray(X_ref, dtype=float).reshape(-1)
30
31     meth = (stopping_method or "none").lower()
32     use_stop = meth in {"ideal", "mlem-stop", "tamaki"}
33
34     def _stat_value(mode, X_ref_vec, check_vec, y_vec, q_vec):
35         if mode == "ideal":
36             return float(root_mean_squared_error(X_ref_vec, check_vec))
37         elif mode == "mlem-stop":
38             return float(mean_squared_error(y_vec, q_vec) / np.mean(
                   q_vec))
39         else:
40             return float(root_mean_squared_error(X_ref_vec, check_vec))
41
42     best_est = arr_est.copy()
43     best_metric = None
44     metric_name = None
45     metric_trace = []
46     no_improve = 0
47     stop_iter = 0
48     stop_reason = "max_iter"
49     iters = []
```

```
50
51      q0 = (r @ arr_est).reshape(-1)
52
53      if use_stop:
54          if meth == "ideal":
55              metric_name = "rmse"
56              best_metric = 1000
57          elif meth == "mlem-stop":
58              metric_name = "mlem-stop"
59              best_metric = 1000
60          metric_trace.append(1000)
61          iters.append(0)
62      else:
63          metric_name = f"trace_only_{stat_when_no_stop}"
64          first_stat = _stat_value(stat_when_no_stop, X_ref_vec, arr_est,
                y, q0)
65          metric_trace.append(1000)
66          iters.append(0)
67
68
69      for it in range(1, calc_num + 1):
70          # --- 1 step update (Nauchi) ---
71          denominator = normalized_r @ arr_est
72          numerator   = (rt / (denominator + eps)).sum(axis=0).reshape(n,
                1)
73          arr_est     = numerator * arr_est
74
75          check = inverse_X(arr_est, F_inv)
76
77          q = (r @ check).reshape(-1)
78
79          if it % record_every == 0:
80              if use_stop:
81                  cur = _stat_value(meth, X_ref_vec, check, y, q)
82              else:
83                  cur = _stat_value(stat_when_no_stop, X_ref_vec, check,
                        target_values, q)
84              metric_trace.append(float(cur))
85              iters.append(it)
86
87              # print(metric_trace)
88
89          if use_stop:
90              if meth == "ideal":
91                  cur = _stat_value("ideal", X_ref_vec, check, y, q)
92                  print(best_metric)
93                  if cur < best_metric - tol:
94                      best_metric = cur
95                      best_est = arr_est.copy()
96                      no_improve = 0
97                  else:
98                      print('cannot be improved')
99                      no_improve += 1
```

```
                    if no_improve >= patience:
                        stop_iter = it
                        stop_reason = f"early_stop_{metric_name}
                            _no_improve"
                        break

            elif meth == "mlem-stop":
                cur = _stat_value("mlem-stop", X_ref_vec, check, y, q)
                if cur <= tol:
                    best_metric = cur
                    best_est = arr_est.copy()
                    stop_iter = it
                    stop_reason = f"hit_{metric_name}_<=_tol"
                    break
                if cur < best_metric - tol:
                    best_metric = cur
                    best_est = arr_est.copy()
                    no_improve = 0
                else:
                    no_improve += 1
                    if no_improve >= patience:
                        stop_iter = it
                        stop_reason = f"early_stop_{metric_name}
                            _no_improve"
                        break

    if not use_stop:
        stop_iter = calc_num
        stop_reason = "no_stopping_max_iter"
        best_est = arr_est.copy()
        best_metric = None

    if return_trace:
        info = {
            "stop_iter": stop_iter if stop_iter else calc_num,
            "stop_reason": stop_reason,
            "stopping_method": meth,
            "metric_name": metric_name,
            "metric_trace": metric_trace,
            "best_metric": None if best_metric is None else float(
                best_metric),
            "best_est": best_est.copy(),
            "tol": tol,
            "patience": patience,
            "iters": iters,
            "record_every": record_every,
        }
        return best_est, info
    else:
        return best_est
```